A MORPHOLOGICAL STUDY OF THE PRIMARY MOTOR CORTEX USING MRI

A MORPHOLOGICAL STUDY OF THE PRIMARY MOTOR CORTEX IN HUMANS USING HIGH RESOLUTION ANATOMICAL MAGNETIC RESONANCE IMAGING (MRI)

EYESHA HASHIM, M.SC.

A Thesis Submitted to the School of Graduate Studies

in Partial Fulfilment of the Requirements for the Degree of

Doctor of Philosophy

September 2014

Ph. D. (2014) McMaster University

(Medical Physics and Applied Radiation Sciences) Hamilton, Ontario, Canada

TITLE: A morphological study of the primary motor cortex in humans using high resolution anatomical magnetic resonance imaging (MRI)

AUTHOR: Eyesha Hashim

M.Sc. (Physics),

Quaid-e-Azam University,

Islamabad, Pakistan

SUPERVISOR: Dr. Nicholas A Bock (Medical Physics)

Supervisory Committee: Dr. Alex Bain (Chemistry)
Dr. Mike Noseworthy (Biomedical Engineering)

NUMBER OF PAGES: xix, 157

To
My mother, Jameela Khatoon
And father, Hafiz Muhammad Yunus (Late)
For their never ending love and affection
And my husband, Hashim Allaudin
For his loving and devoted companionship

بنام

والدہ محترمہ جمیلہ خاتون اور والد محترم حافظ محمد یونس مرحوم

جنکی بے پناہ محبتوں اور شفقتوں کے سائے

اور میرے شوہر ہاشم علاؤالدین

جنکا بے بدل ساتھ اور رفاقت ہمقدم رہے۔

Abstract

Myeloarchitecture is a prominent feature that can identify the primary motor and sensory areas in the cerebral cortex and is increasingly imaged in magnetic resonance imaging (MRI) studies of cortical parcellation in humans. However, MRI studies of cortical myeloarchitecture are technically difficult for two reasons: the cortex is only a few millimeters thick, and intracortical contrast due to myelin is much smaller than the overall anatomical contrast between cortical tissue and underlying white matter that is typically utilized in imaging. The research in this thesis thus presents specific MRI protocols to visualize intracortical myelin, image processing protocols to delineate the heavily myelinated cortex from the adjacent typical cortex and the application of these techniques in the precentral motor cortex to study morphology of the highly myelinated dorso-medial part, consisting of Brodmann area (BA) 4 and part of BA 6.

Optimization of the MRI protocols involved determining the sequence parameters for a T_1-weighted MRI sequence to obtain maximal intracortical contrast at 0.7 mm isotropic resolution in imaging time of 15 min, based on T_1 differences between cortex that is myelinated (GMm) or unmyelinated (GM). As part of the optimization, T_1 values were measured in the following brain tissues: GM, GMm and white matter (WM). The optimization was carried out by simulating the MRI signal for a 3D, magnetization prepared, gradient echo sequence, using the measured T_1 values in the analytical signal equations. It was found that

lengthening the time delay at the end of each inner phase encoding loop increased the intracortical contrast. The optimization of MRI protocols also included implementing techniques to reduce radio frequency field (B1) inhomogeneities. It was found that dividing the optimized, T_1-weighted MRI with a predominantly proton density weighted image resulted in a ratio image with significantly reduced B1 inhomogeneities.

The goal of the image processing protocols developed in this thesis was to visualize the variation of intracortical myelin across the precentral motor cortex and to delineate its well-myelinated dorso-medial part. The myeloarchitectonic feature that was selected to visualize the variation in intracortical myelination was the thickness of GMm in the deeper parts of the cortex relative to the cortical thickness, referred to as the proportional myelinated thickness (p). To measure p, the following processing steps were performed. The ratio image was segmented into four tissues: GM, GMm, WM and cerebrospinal fluid (CSF) using fuzzy C-means clustering technique. Using a level set approach, thickness of the cortex was determined as the distance between the outer boundaries of GM and WM and thickness of GMm or myelinated thickness (*m*) was determined as the distance between the outer boundaries of GMm and WM. The proportional myelinated thickness *p*, was calculated as follows: $p = m/t$. The well-myelinated dorso-medial part of the precentral cortex, referred to as M_m, was distinguishable from the adjacent cortex when the proportional myelinated thickness was projected on the outer cortical surface.

The optimized MRI and image processing techniques developed in this thesis were used to investigate cortical plasticity in amputees. Two morphological features of the myeloarchitecture over M_m, the mean proportional myelinated thickness and area, were measured in four lower limb amputees and four matched controls. A comparison of these morphological features showed no statistically significant difference ($p < 0.05$) between the two groups.

Acknowledgments

I offer my sincere thanks to my supervisor, Dr. Nicholas A Bock, for his continuous support and guidance throughout this journey. His vision and knowledge showed me the way. I am thankful to him for accepting me as a graduate student, encouraging me to transfer to PhD and always keeping the bar raised to make me work harder. A special thanks to him for patiently guiding me how to attempt scientific writing.

I am also very thankful to other members of my supervisory committee, Drs. Alex Bain and Mike Noseworthy for providing expert opinion on my project and for adding breadth to my knowledge by discussing my project with me. I am also grateful to Mike for providing MRI facilities and for providing very detailed feedback on my thesis. I am thankful to Alex for never forgetting to give positive and encouraging comments about my work.

I am thankful to my family for always loving me and believing in me. A special thanks to my uncle Juneid Akram and my elder brother Anas Noman for taking care of me like their daughter. My heart-felt thanks to my brother Salman Yunus for also being a heart-to-heart friend and for working hard to keep the love, for everything under the sun except science, alive in me. I am hugely in debt to my sisters Khaula Kausar, Sajda Kausar, Tooba Kausar, Abda Yunus, Majda Yunus, Amna Yunus and Maryam Yunus, and my sister-in-law Shahida Noman, for their profound love and emotional support. I am grateful that my brother Salman Yunus, aunt Rukhsana Ruhi, niece Barira Tahir and nephew Jawad Hafeez have been around here in North America as their presence made the process of settling down in a new country easier. My heart-felt thanks go to Hashim's family for accepting me as one of their own and for generously feeding me delicious home cooked meals. I am also in debt to Hashim's niece Rafia Allaudin for being an invaluable friend. My friends Emma Bahroos, Farah Akhtar, Mehnaz Ishrat, Saadia Tanveer, Shiraza Shakeel, Sumaira Ali and Uzma Nackvi

have always been a source of inspiration and support for me regardless of the rather infrequent contact.

I am grateful to my colleagues Aundrey Hanu, Chris Rowley, Lianne Lobo, Nataliya Moldovan, Nelson Miksys, Sagar Buch, Saifeng Lu and Sepideh Behinaein for helping me on the road to discovery. A special thanks to Lianne Lobo for finding me funny at times, and for her friendship. A sincere thank you goes to the staff at the Medical Physics office for providing excellent administrative support. I am also very thankful to the staff at the Imaging Research Centre, St. Joseph's Hospital, specially Norm Konyer, for the much needed technical support. I am also grateful to all the people who allowed me to scan their brains for the sake of my project.

Contents

List of Figures

List of Tables

List of abbreviations and symbols

A	Anterior
a.u.	Arbitrary units
A1	Primary auditory cortex
AC	Anterior commissure
ACQ	Acquisition
BA	Brodmann's area
BRAVO	General Electric's acronym for Fast Spoiled Gradient Echo
CC	Corpus callosum
CNR	Contrast to noise ratio
CSF	Cerebrospinal fluid
D	Dimension
DTI	Diffusion tensor imaging
EEG	Electroencephalography
EPI	Echo planar imaging
FA	Flip angle
FLASH	Fast low angle shot
FMC	Fast marching cubes
FOV	Field of view
GE	General Electric
GM	Gray matter

GMm	Myelinated gray matter in the cortex
Gpe	Phase encoding gradient
GRE	Gradient echo
Gss	Slice encoding gradient
IR	Inversion recovery
LSM	Level set method
M	Male
M1	Primary motor cortex
MEG	magneto encephalography
Mm	Well-myelinated dorso-medial part of the precentral gyrus
mm	Millimeter
MPRAGE	Magnetization prepared, rapidly acquired gradient echo
MR	Magnetic resonance
MRI	Magnetic resonance imaging
MS	Multiple sclerosis
ms	Millisecond
MTR	Magnetization transfer
MultS	Multiple slices
p	Proportional myelinated thickness
P	Posterior
PC	Posterior commissure
PE	Phase encoding

PFC	Prefrontal cortex
RF	Radio frequency
RL	Right-left
ROI	Region of interest
S1	Primary somatosensory cortex
SD	Standard deviation
SI	Superior-inferior
SNR	Signal to noise ratio
SPGR	Spoiled gradient echo
SS	Single slice
t	Cortical thickness
T	Tesla
TD	Time delay
TE	Echo time
TI	Inversion time
TOMROP	T-One by Multiple Readout Pulses
TR	Repetition time
V1	Primary visual cortex
WM	White matter
B_1	Radio frequency field
B_1^-	Receive field
B_1^+	Transmit field

T_1^*	Effective longitudinal relaxation time
T_1	Longitudinal relaxation time
T_2	Transverse relaxation time
T_2^*	Effective transverse relaxation time
ρ	Proton density
Φ	Level set function

1 Introduction

1.1 Cortical morphology and its significance

The cerebral cortex is a highly convoluted, layered structure that is a few millimeter (mm) thick and makes up the outer surface of the brain in primates and other mammals. The cortex consists mainly of neuronal cell bodies that give it a gray colour in formalin-fixed tissue and hence the name gray matter. The cortex is a highly organized structure, both functionally and anatomically. It coordinates a vast number of important functions including motor control, sensation, vision, and hearing. There are specific cortical fields or areas dedicated exclusively to these primary functions called primary functional fields that have distinguishable anatomical characteristics when compared with the adjacent cortex. Gross morphological differences are also known to be present between various cortical fields. For example, the primary motor field in the precentral gyrus is much thicker than the posteriorly adjacent somatosensory (S1) cortex (Brodmann, 1909; von Economo and Koskinas, 1925).

The high degree and specificity of cortical organization raises many questions such as whether function and anatomy are correlated and if cortical field sizes depend on factors such as age, sex and gender. Another important question that arises is whether the cortex reorganizes, functionally or anatomically, as a result of experience (learning) or disease. To answer these questions*, in vivo* human studies of cortical mapping are needed in healthy and diseased cortex.

Functional reorganization might, for example, involve the recruitment of a cortical field for a function other than the one it originally performed. Functional mapping of the cortex can be performed using invasive procedures such as electro-corticography and direct cortical electrical stimulation, and also using non-invasive means such as functional magnetic resonance imaging (fMRI) (Matthews *et al.*, 1999) electroencephalography (EEG) (Niedermeyer and Lopes da Silva, 2005) and magneto encephalography (MEG) (Preissl, 2005). Many human and non-human studies have found functional reorganization of the cortex as a result of major changes in function. For example, a transient, enlarged hand representation in S1 was found in patients recovering from a stroke affecting motor control of the upper limbs (Roiha *et al.*, 2011). Functional reorganization of S1 in subjects with spinal cord injury has also been reported (Henderson *et al.*, 2011).

Changes in anatomical organization of the cortex could be of many types including changes in the sizes or shapes of neurons (morphology), changes in their organization, changes in their synaptic connections or changes in their axonal characteristics such as myelinated length or myelinated diameter. Some of these changes might affect the overall gross morphology of the affected cortical region. Thus, anatomical reorganization can be detected via changes in cortical thickness and also the size, shape or volume of cortical regions.

In vivo studies of cortical mapping and cortical morphology are important for several reasons. There is evidence that gross morphological features are

altered in some neurodegenerative disorders. For example, cortical thinning has been reported in the somatosensory and motor areas in Tourette syndrome (Fahim *et al.*, 2010) and in Huntington's disease (Rosas *et al.*, 2008). Focal thinning of the frontal and temporal lobe is detectable even in the early stages of multiple sclerosis (MS) (Sailer *et al.*, 2003). Alzheimer's disease (AD), which is a major health and social problem in countries with long life expectancy, is also known to result in cortical thinning (Tokunaga *et al.*, 2013). Furthermore, early stages in AD can be diagnosed using a criterion that is based on cortical thickness (Querbes *et al.*, 2009). Thus, if changes in cortical morphological features are robustly tracked, these can serve as bio-markers for some neurodegenerative disorders.

Because the cortex plays a key role in several functions, it is important to investigate cortical health for determining the outcome of rehabilitation and treatment efforts. Cortical plasticity studies suggest that the absence of a primary function at birth affects cortical morphology. For example, increased surface area, but reduced thickness of the primary visual fields has been reported in congenitally blind subjects when compared to sighted individuals (Park *et al.*, 2009). Thus, efforts to restore vision in the blind may also require assessment of the visual cortex too, and robust *in vivo* techniques for investigating cortical morphology may enhance the outcome of rehabilitation efforts.

Another important application of studies of *in vivo* cortical morphology is in surgical planning. A correlation of function with anatomy can be established via

cortical mapping (Dick *et al.*, 2012) which can help in refining the area of focus in brain surgery.

While numerous studies exist that investigate the functional organization of the cortex under normal and abnormal conditions, corresponding anatomical studies are comparatively limited. This is because of the challenges involved in imaging the thin, convoluted cortex *in vivo* with enough resolution and contrast to visualize its fine anatomical details. While an *in vivo* investigation of individual neuronal cell morphology is yet not possible, advances in anatomical magnetic resonance imaging (MRI) and brain image processing techniques have made it possible to determine gross morphological features such as cortical thickness and areal boundaries in living subjects. The goal of this thesis is to present a novel technique using longitudinal relaxation time (T_1) -weighted MRI optimized to enhance contrast across the cortex based on its myelin content to study the morphology of motor field in the precentral cortex *in vivo*.

1.2 A little about cortical morphology

The cortex is a layered sheet of tissue, which is typically divided into six layers, as shown in Figure 1.1 (Brodmann, 1909). The layers are numbered I to

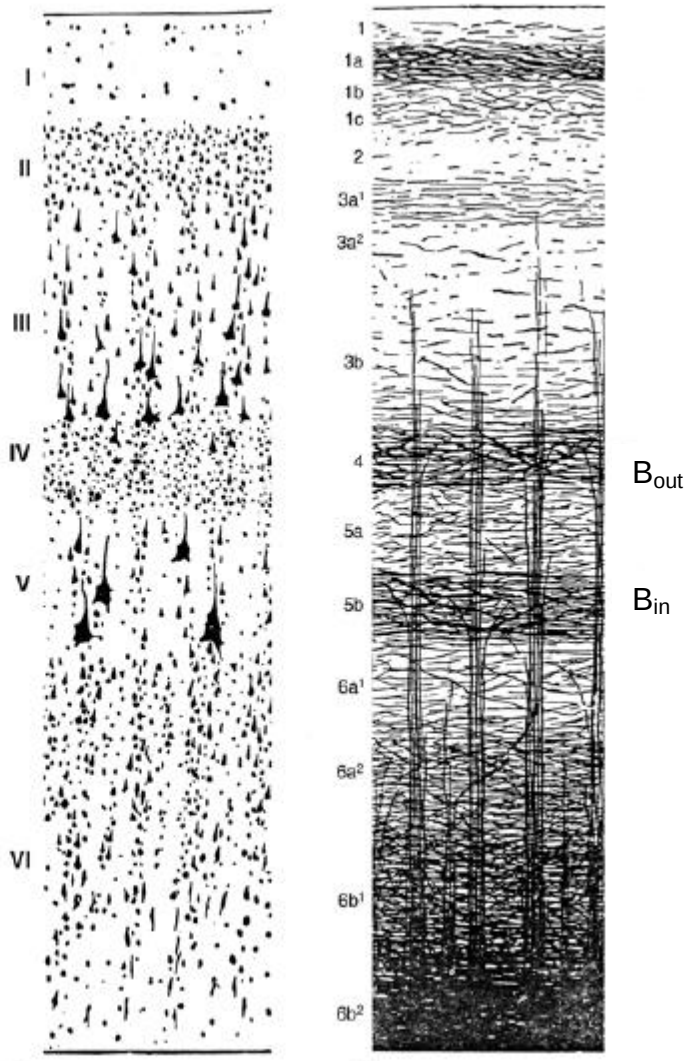

Figure 1.1: The laminar pattern of the human cortex (Reprinted with permission-(Nieuwenhuys *et al.*, 2008)). The left panel shows cortical layers as seen in a Nissl stained section while the right panel shows the layers in a typical myelin stained section.

VI, starting from the most superficial to the deepest layer. The top two layers contain fewer and smaller and neurons of variable shapes than the other layers. Layer III contains pyramidal cells and is considered to contribute to interhemispheric connections. Layer IV contains granular cells and is known to

contribute to the thalamic and intrahemispheric connections. Layer V contains larger pyramidal cells and is known to contribute to corticospinal connections. Layer VI contains cells of various shapes and it is also known to contribute to thalamic connections.

1.3 How to study cortical morphology?

While cortical morphology can be studied using various region-specific features such as neurotransmitters (Geyer *et al.*, 1996) pigment-labelling of the cells (Braak, 1980), cell structures (Brodmann, 1909; von Economo and Koskinas, 1925), myelinated fibers (Vogt and Vogt, 1909; Elliot, 1907; Nieuwenhuys, 2013; Vogt and Vogt, 1928) and many more, the most frequently used anatomical techniques rely on one of the following features to differentiate between various cortical regions:

- Shape, size and packing density of cell bodies in the cortex, referred to as cytoarchitecture.
- Size, orientation and density of myelinated fibers in the cortex, referred to as myeloarchitecture.

A traditional marker of the primary motor cortex on histology is the presence of Betz cells, the largest neurons in the cortex. These giant pyramidal cells are found in the layer V of the primary motor cortex only. Their longest body dimension is reported to be 126 microns in humans (Lewis and Henry, 1877). Thus, to define M1 *ex vivo*, one would need to identify these cells in cortical layer V in histological sections of the precentral gyrus. This means that parcellation

studies using cytoarchitecture require high microscopic resolution to visualize these structures on micron scale along with a means to differentiate between various cell shapes. Consequently, studies of cytoarchitecture are mostly limited to thin slices of excised cortical tissue stained for various cell types and observed under a microscope. The very well-known *ex vivo* cortical mapping study by Brodmann in the early years of the twentieth century divided the human cortex into 52 distinct regions based on cytoarchitecture (Brodmann, 1909). Another more detailed *ex vivo* cytoarchitectonic study by von Economo and Koskinas divided the human cortex into 107 distinct regions (von Economo and Koskinas, 1925). These two pioneering studies provide a wealth of information about the location and cytoarchitecture of various cortical fields. Brodmann's study is frequently referred to in the neuroscience literature with various cortical fields being described as Brodmann's areas (BA).

Myelin is a lipid-protein layered material that ensheathes the axons of neurons in the central and peripheral nervous system. In the central nervous system, myelin is mostly present in the white matter (WM) tracts. Some myelin, referred to as intracortical myelin, is also present in the cortical gray matter (GM). Cortical myelin presumably speeds up axonal conduction and also protects against aberrant synaptic connections (Braitenberg, 1962; Braitenberg, 1974). Detailed *ex vivo* studies of myeloarchitecture in the human cortex have been reported by the Vogts, Hopf and Braak (Vogt and Vogt, 1909; Vogt and Vogt, 1928; Braak, 1980; Hopf, 1954).

Myelinated fibers of various calibers are present in the cortex in radial (along the depth) and horizontal (along the surface) directions. The horizontal fibers constitute the inner and outer bands of Baillarger in layers V-b and IV-b over almost the entire cortex (Baillarger, 1840). The thickness of these bands and of the unmyelinated tissue separating them varies across the cortex. The bands also vary in the density of myelinated fibers across the cortex. The radial fibers are mostly cortical extensions of myelinated axons from the WM underlying the cortex, and their height also varies along the cortex (Braitenberg, 1962; Nieuwenhuys, 2013). The most important feature of intracortical myelin is that the primary functional areas are well myelinated with characteristic features of myeloarchitecture that distinguish them from the adjacent cortex (Nieuwenhuys, 2013; Braitenberg, 1962; Braak, 1980; Vogt and Vogt, 1928; Vogt and Vogt, 1909; Elliot, 1907; Hopf, 1954). The most well-known example is of the primary visual cortex (V1) where the outer band of Baillerger, referred to as the stripe of Gennari, is distinctly well myelinated. The other examples are S1, the primary motor cortex (M1) and the auditory cortex (A1). Figure 1.2 shows a schematic drawing of various regions of the cortex based on myeloarchitectonic analysis of unstained sections of the human cortex by Elliot Smith (Elliot, 1907). This type of parcellation suggests that myeloarchitecture could be used to identify specific cortical areas if it could be imaged using MRI.

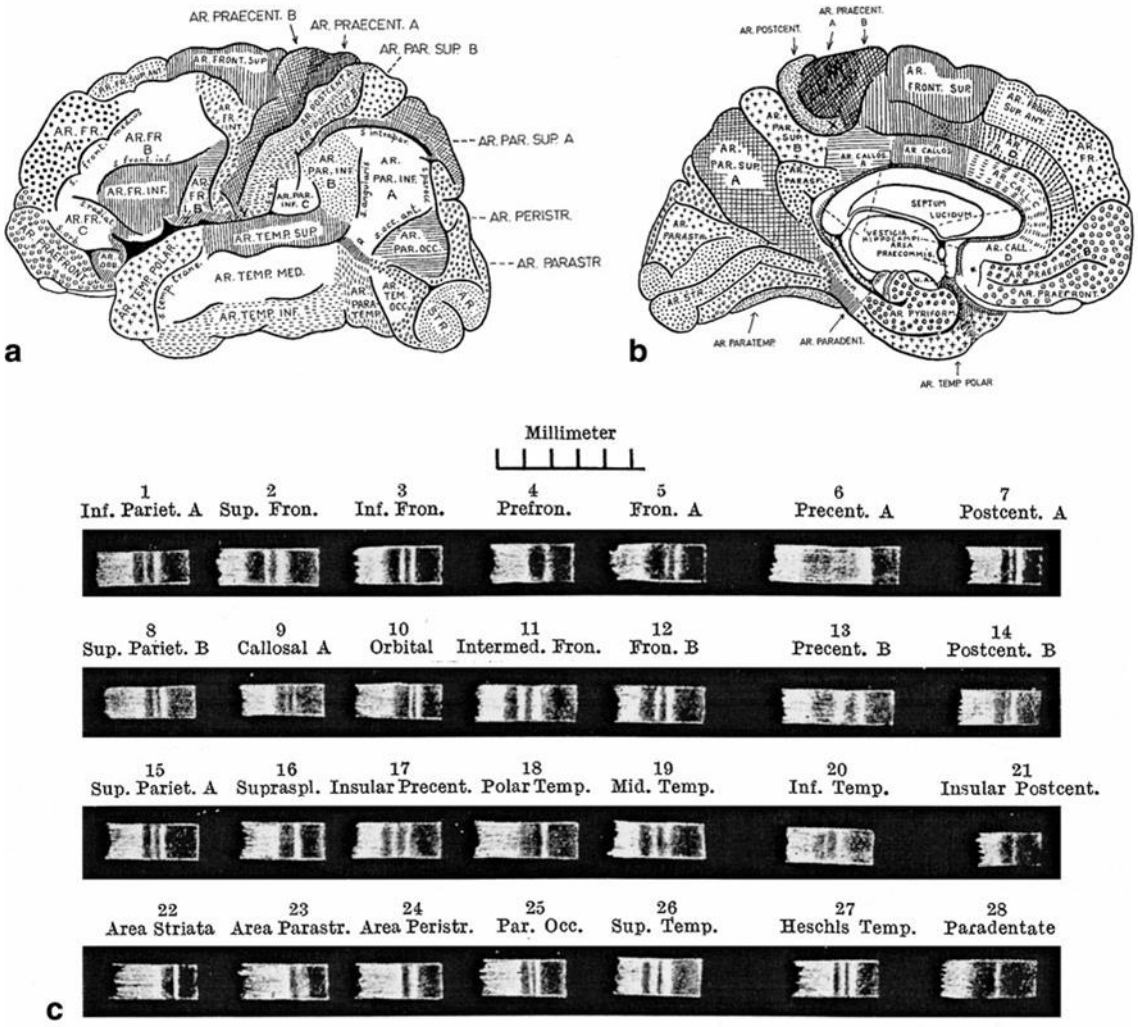

Figure 1.2: Myeloarchitectonic features of various regions in the human cortex. Panels a and b show the variation of intracortical myelin on the cortical surface. Part c shows various cross-sections through the cortex drawn on a blackboard with white chalk to show their myelin content. In these sections, WM is to the left while the outer cortical boundary is to the right. (Original work by (Elliot, 1907)) - reprinted with permission from (Nieuwenhuys, 2013)).

1.4 MRI of intracortical myelin: the possibility of *in vivo* cortical mapping

Myelin affects the values of key magnetic resonance (MR) parameters including longitudinal relaxation time (T_1) and transverse relaxation time (T_2) (Laule *et al.*, 2007). Specialized MRI techniques such as diffusion tensor imaging (DTI) (Schmierer *et al.*, 2007) and magnetization transfer imaging (MTR) (Cook *et al.*, 2004) have also been shown to be sensitive to the myelin content. Furthermore, intracortical myelin persists through an entire layer or several layers in the cortex, thus making it possible to visualize myeloarchitectonic features in *ex vivo* sections, based on their lighter shade in the fresh or formalin fixed brain, even without the aid of myelin staining and with low magnification power (Elliot, 1907; Geyer *et al.*, 2011). This makes identifying intracortical myelin on MRI much easier than identifying cytoarchitectonic features. Cytoarchitectonic features are detectable on MRI only in rare situations such as in the entorhinal cortex, where macro-islands of large neurons are found (Augustinack *et al.*, 2005). Keeping in mind the completely non-invasive nature of MRI, anatomical MRI of intracortical myelin has invaluable potential for *in vivo* cortical mapping studies in humans.

The possibility of *in vivo* cortical mapping based on MRI of intracortical myelin was first revealed in 1992 using proton density -weighted contrast (Clark *et al.*, 1992). It is now becoming increasingly popular for its reproducibility. Various MRI studies have reported detection of intracortical myelin *in vivo* based on T_1 (Barbier *et al.*, 2002) and T_2 –weighted (Yoshiura *et al.*, 2000) contrast.

More recently, the variation in the overall myelin content along the cortex at a middle depth has been used to map several primary and associated regions in group-averaged atlases of the human cortex using T_1 and T_2-weighted (Glasser and Van Essen, 2011) MRI. MRI contrast based on the effective or apparent T_2 (T_2^*), which characterizes the dephasing of the transverse magnetization at a rate faster than T_2 due to the presence of magnetic field inhomogeneities, has also been used to map several cortical regions in group-averaged atlases of the human cortex (Cohen-Adad *et al.*, 2012). *In vivo* cortical mapping based on MRI of intracortical myelin in individual subjects has mostly been limited to targeted regions such as V1 (Trampel *et al.*, 2011; Geyer *et al.*, 2011; Bridge *et al.*, 2005), A1 (Sigalovsky *et al.*, 2006), and M1 (Kim *et al.*, 2009). Some targeted studies have correlated anatomical boundaries determined by MRI of intracortical myelin with functional boundaries in V1 (Bridge *et al.*, 2005; Sereno *et al.*, 2013; Sanchez-Panchuelo *et al.*, 2012) and A1 (Dick *et al.*, 2012). A very recent, whole brain study has investigated the correlation of intensity on T_1- and T_2- weighted MRI due to intracortical myelin with cortical plasticity (Grydeland *et al.*, 2013). No *in vivo* human cortical mapping studies based on MRI of intracortical myelin have yet been reported that investigate cortical plasticity by analyzing morphological features such as the thickness of myelinated cortical layers or the area of heavily myelinated regions.

In vivo cortical mapping using myelin-based contrast faces many challenges. The first challenge comes from the cortical morphology itself. The

cortex is only 2-3 mm thick on average and it is further divided into layers of sub-mm thickness (Brodmann, 1909; Zilles, 2004). Also, it has a high and variable curvature. Furthermore, myelinated GM does not span the entire cortical thickness even in the well-myelinated primary functional areas. Therefore, high and isotropic resolution is required to visualize intracortical details on anatomical MRI. Achieving such resolution inevitably increases imaging time and also results in lower signal to noise ratio (SNR).

Another challenge comes from the fact that the myelin that gives rise to intracortical contrast is also responsible for the overall anatomical contrast between the WM and the cortex in the brain. The myelinated fibers in the cortex are fewer in number and less heavily myelinated compared to the bundles of WM tracts underlying the cortex. Thus, the relatively smaller intracortical contrast appears to be even more diminished because of the dominating contrast between the cortex and the WM. Also, it has been shown that robust detection of intracortical myelin is correlated more with intracortical contrast rather than with SNR in the brain images (Clare and Bridge, 2005). Therefore, unless specific measures are taken to enhance the intracortical contrast, the delineation of cortical regions on the basis of myelin content will be difficult.

In conclusion, morphological studies of the cortex which rely on the detection of intracortical myelin should be performed with optimized MRI and sub-millimeter isotropic resolution. Keeping in mind the discomfort of the subjects and higher probability of motion associated with increased imaging times, the

objective of optimization should be to achieve higher intracortical contrast while keeping the imaging time as short as possible.

1.5 Processing brain images to delineate and measure cortical regions based on intracortical myelin

An important step in cortical mapping studies is to accurately process brain images to extract useful information. The most important part of the processing scheme for a cortical mapping study is to select a feature of the images that can be used as a marker to investigate the regions of interest. Most anatomical MRI studies of cortical mapping have relied on the variation of MR intensity at a middle depth in the cortex to visualize cortical regions (Glasser and Van Essen, 2011; Bock *et al.*, 2013). In this thesis, a novel technique to map the cortex based on morphological properties of the myelin content is presented. The myelinated tissue in the cortex, referred to as myelinated GM or GMm in this thesis, has the following unique characteristic: its thickness and density in the primary functional areas is greater compared to the rest of the cortex. Thus, measurement of the thickness of GMm relative to the total cortical thickness was proposed to delineate and measure the extent of well-myelinated cortical regions. This morphological quantity is referred to as the proportional myelinated thickness. The greatest advantage of using the proportional myelinated thickness for studying cortical morphology is that it is a morphological quantity and hence independent of the scanner, field strength and imaging protocol. Thus, the results can be compared across various centres and in longitudinal studies as well.

1.6 An overview of this thesis

The goal of this thesis was to develop a novel *in vivo* technique to study cortical morphology using T_1-weighted MRI, optimized to enhance contrast across the cortex based on its myelin content, and apply this technique to investigate morphology of the primary motor cortex in humans. T_1-weighted MRI was selected because of its wide clinical use. Also, it has been shown using fixed tissue that MR intensity profiles in T_1-weighted images are better correlated with myeloarchitectonic than cytoarchitectonic profiles (Eickhoff *et al.*, 2005). The first goal of this thesis, therefore, was to optimize a T_1-weighted, 3D MRI sequence to obtain sub-mm isotropic resolution with enhanced intracortical contrast. Ideally, imaging with as high a resolution as possible is desired, but to avoid an overly long imaging time, resolution was limited to 0.7 mm isotropic. Optimization of the MRI protocols is the subject of Chapter 2.

The next goal was to process the images accurately and reproducibly to delineate and measure the extent of the cortical region of interest using proportional myelinated thickness as a metric. Measuring the thickness of GMm in the cortex required segmenting the GMm as a separate tissue. Thus, the most important feature of the processing protocols was that the brain is segmented into four tissues - namely, GMm, GM, WM and the cerebrospinal fluid (CSF). The processing protocols are described in Chapter 3.

The last goal of this thesis was to apply the morphological techniques of cortical mapping to a selected region in the cortex in a group of subjects. The

precentral motor cortex was chosen for application of the technique. The precentral gyrus has several anatomical features that make it a suitable candidate for a pilot study like the one presented here. For example, it is the thickest region of the human cortex at 4.5 mm (Brodmann, 1909; Zilles, 2004) and this region of the cortex is extensively myelinated. Furthermore, myelinated GM in this cortical region is known to persist through several layers (Nieuwenhuys, 2013; Braak, 1980). Thus, intracortical details can likely be visualized in this part of the cortex with the 0.7 mm isotropic resolution used in this study. The morphology of the precentral motor cortex was studied in four male lower limb amputees and their age-matched controls, using the myeloarchitectonic features of the cortex. Thus, the techniques developed in this thesis were used to assess whether the human motor cortex morphology is altered when some part of the motor field is deprived of its prescribed output connectivity. The *in vivo* study of the precentral motor cortex in lower limb amputees is the subject of Chapter 4. The last chapter, Chapter 5, summarizes the important conclusions from the entire thesis and discusses future directions.

2 Developing MR Techniques for Optimized, 3 Dimensional T_1-Weighted Myelin Imaging of M1 in Humans at 3 Tesla

2.1 Introduction

This chapter describes the development of techniques for anatomical MR imaging at 3 Tesla (T) to better visualize and delineate the primary motor cortex (M1) located in the precentral gyrus, based on myelin content. A wider range of longitudinal relaxation time (T_1) compared to transverse relaxation time (T_2) values across the brain tissues renders T_1 weighting the most common technique of choice in anatomical MRI of the brain (Wansapura *et al.*, 1999). An inversion-recovery, T_1 -weighted sequence was used as this family of sequence is known to produce maximal anatomical contrast in high resolution 3D imaging (Deichmann *et al.*, 2000). Optimizing T_1 -weighted MRI to achieve enhanced intracortical contrast based on myelin involves measuring T_1 values in the relevant brain tissues and then optimizing the MRI protocols using those values. T_1 values were measured in the following tissues in the brain: gray matter, myelinated gray matter and white matter. The first section in this chapter describes these T_1 measurements. A 3D magnetization prepared-rapidly acquired- gradient echo (MPRAGE) sequence was used for T_1 -weighted anatomical MRI. The second section describes the optimization of anatomical MRI protocols. This includes simulating the MPRAGE using T_1 values determined and presented in this thesis to achieve greater intracortical contrast and also employing a technique to reduce B1 inhomogeneities. The third section in this

chapter demonstrates imaging of M1 in subjects, using the optimized MRI protocols.

2.2 T_1 measurements in brain tissues

In this section, T_1 measurements at 3 T in three brain tissues of interest are reported: unmyelinated or typical cortical gray matter (GM), myelinated gray matter in the cortex (GMm), and white matter (WM). Unmyelinated or typical cortical gray matter is referred to as gray matter (GM) in this thesis. Intracortical contrast (between the two types of gray matter) is required to delineate the well myelinated, primary sensory and motor areas from the rest of the cortex. Optimizing the T_1 –weighted, 3D imaging sequence for maximal intracortical contrast requires a knowledge of the T_1 values of GM and GMm. Also, it is necessary to measure T_1 in WM to optimize the overall anatomical contrast between GM and WM in the brain. The overall anatomical contrast is beneficial in image post-processing routines such as tissue segmentation.

2.2.1 Methods

T_1 measurements were performed in five healthy, female volunteers aged 22-24 years at St. Joseph's Healthcare, Hamilton. The Research Ethics Board of the institution approved the study and informed consent was obtained from the volunteers before scanning. The study was performed using a GE MR 750 3 T scanner (General Electric Healthcare, Milwaukee, WI, software version 22.0) and a 32 channel receive-only head coil (MR Instruments).

A medial, sagittal slice was chosen as the location for T_1 mapping as a slice in this orientation and location contains regions belonging to all three tissues of interest in the brain, namely WM, GM and GMm. The primary sensory and motor areas of the cortex are highly myelinated whereas the frontal cortex is known to be relatively unmyelinated gray matter (Baillarger, 1840; Elliot, 1907; von Economo and Koskinas, 1925). The corpus callosum is an example of pure white matter. A medial sagittal slice will cut through the primary motor and somatosensory areas along with the frontal cortex and corpus callosum. This observation was guided by myelin-stained sections in an online human brain atlas (http://www.brainmuseum.org). Capturing one such slice in each subject is therefore sufficient to obtain T_1 maps for the purpose of this study.

T_1 maps were made by acquiring T_1-weighted inversion recovery (IR) images with an echo planar imaging (EPI) read-out. EPI images usually suffer from geometric distortions because of the very small bandwidth along the phase-encoding direction. Phase bandwidth in multi-shot EPI is increased by increasing the number of shots or segments thereby resulting in lesser distortion (Bernstein *et al.*, 2004). A multi-shot EPI was thus chosen instead of a single shot EPI. IR sequences use a 180° pulse in the beginning of the sequence to invert the equilibrium longitudinal magnetization M_o to $-M_o$. The inverted magnetization then recovers to the equilibrium value at a rate governed by the longitudinal relaxation time T_1, as given by Equation 2.1:

$$M = M_0\left(1 - 2\,e^{\frac{-TI}{T_1}}\right) \qquad 2.1$$

where *M* is the instantaneous value of longitudinal magnetization and TI is the inversion time from the end of the 180° pulse to the beginning of the readout phase. A typical inversion recovery curve is shown in Figure 2.1.

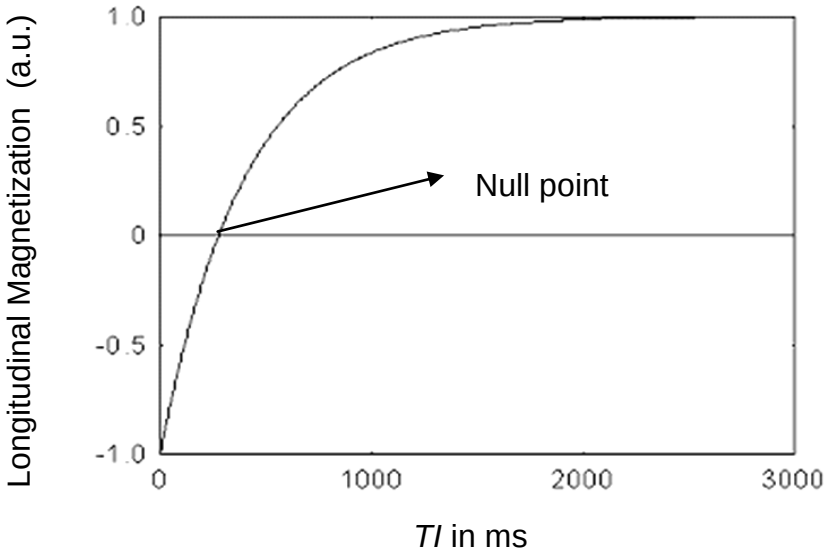

Figure 2.1: Inversion recovery curve according to Equation 2.1 for a tissue with T_1 of 400 ms approximately. The null point is where the magnetization becomes zero while recovering from negative to positive values.

Equation 2.1 and the recovery curve shown in Figure 2.1 indicate that for a certain TI, referred to as the null point, the magnetization becomes zero while recovering from negative to positive values. The null point occurs when $2e^{\frac{-TI}{T_1}} = 1$. For an average T_1 of 1000 ms in the brain based on T_1 values found in the literature for gray and white matter at 3T (Rooney *et al.*, 2007; Wright *et al.*, 2008) the null point occurs at TI = 700 ms. Thus, inversion times were chosen on both

sides of the null point to estimate the behaviour of the curve accurately. Equation 2.1 also indicates that the magnetization would be relaxed back to 99% of its initial value at TI = 5 T_1. Thus, the average time for almost full relaxation is 5000 ms, although tissues with longer T_1 would require significantly greater time. While it is certainly advisable to keep the maximum TI higher to allow for full relaxation for all tissues, it does not affect the accuracy of the fit so long as there are enough points on each side of the null point to guide the fit (Tofts, 2003). A value of 4000 ms was thus chosen for the maximum TI so that the total imaging time is about 30 minutes.

A slice-selective sinc pulse was used for inversion. The following parameters were used for the scans: TE = 34.9 ms, number of EPI segments = 4, recovery time between the excitation pulse and the next inversion pulse = 9000 ms, FOV = 25 cm x 25 cm, Matrix = 256 x 256, Slice thickness = 1mm, Number of averages = 5, TI (selected randomly on either side of the null point) = 50, 300, 500, 800, 1000, 2000, 3000, 3500, and 4000 ms, approximate total time for mapping = 32 minutes.

Equation 2.1a describes the signal for an IR sequence.

$$S = K\,(1 - 2\,e^{\frac{-TI}{T_1}}) + C \qquad 2.1\,a$$

The variable K here is proportional to the proton density and C is an absolute bias added for fitting purposes to accommodate signal variations due to scanner gain. Using a non-linear, least squares algorithm in Matlab (MathWorks), these T_1-weighted EPI images were fit pixel-by-pixel to a three parameter, single

exponential T_1 recovery curve according to Equation 2.1a to generate T_1 maps. As the data from the scanner was obtained in the magnitude form, a modulus of Equation 2.1a was used, as given below in Equation 2.1b.

$$S = \left| K\ (1 - 2\ e^{\frac{-TI}{T_1}}) + C \right| \qquad 2.1\ b$$

The sum of the squared differences between the fitted curve and the experimental data was minimized by varying the three parameters: *K*, T_1 and C. To eliminate low SNR data, pixels with intensity value shorter than 60% of the mean intensity in the longest TI (4000 ms) image were removed from the fit by thresholding. The maximum TI of 4000 ms implies that the signal for tissue with T_1 close to and greater than 4000ms will not cross the null point. The maximum TR of 9000 ms was also not sufficient for complete relaxation of the signal for tissues with T_1 values greater than 1800 ms (5 x T_1= 9000 ms for T_1 = 1800 ms). Calculated T_1 values above 4000 ms were therefore removed from T_1 maps using thresholding.

T_1 in GM, GMm and WM tissues in the brain were measured from T_1 maps using ImageJ software (http://rsb.info.nih.gov/ij) as the mean T_1 pixel value in a region of interest (ROI) drawn in each of the tissues. The ROI locations were selected through comparison with myelin-stained sections in the online human brain altlas (http://www.brainmuseum.org) to ensure that all three types of the tissues were measured in the maps. For GM, the ROI was placed in the frontal

cortex, for GMm, in the medial portion of the precentral gyrus and for WM, in the genu of the corpus callosum.

Statistical analyses were performed using SPSS software (IBM SPSS Statistics Version 20.0, IBM Corp.). T_1 data were first assessed for normality using the Shapiro-Wilk test. Levene's test of equality of error variances was then used to test the homogeneity of variances of the T_1 values across tissues types. A one-way ANOVA followed by a Tukey HSD post-hoc test was used to test pair-wise significant differences in T_1 values between tissue types.

2.2.2 Results

Figure 2.1a shows T_1 maps obtained from the five subjects. All images are cropped to remove extraneous areas and are displayed at the same window and level.

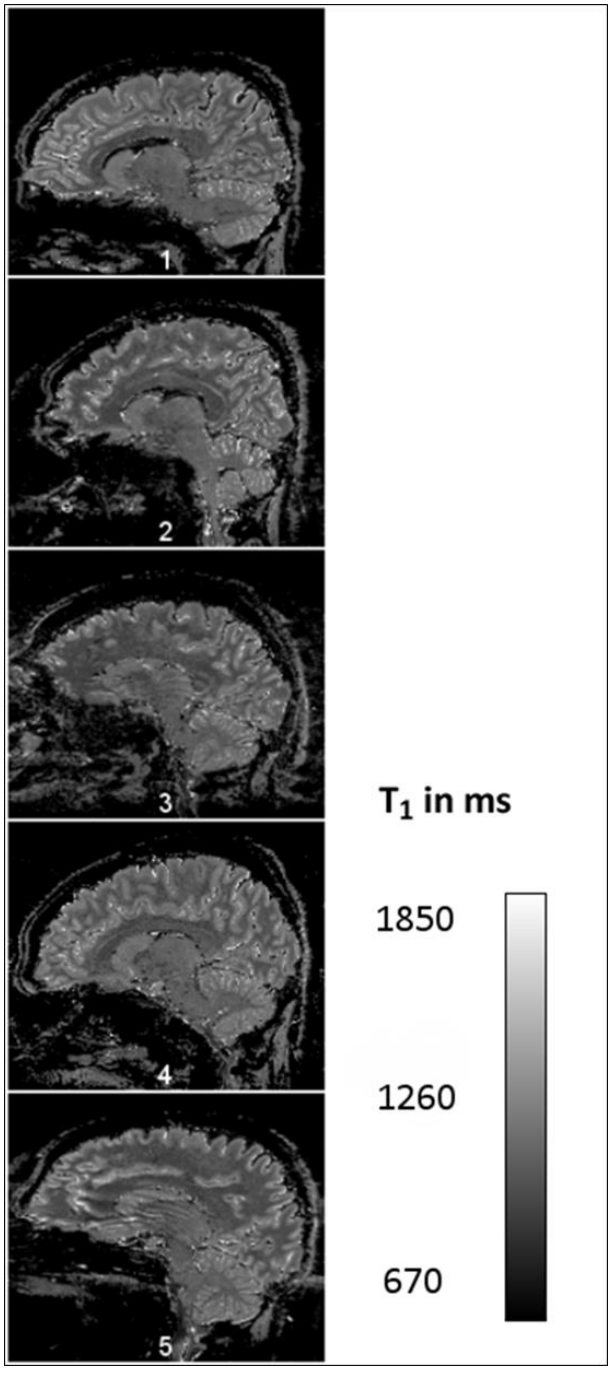

Figure 2.2a: T_1 maps in five healthy female subjects, ages 22-24 years, through a medial sagittal slice in the right hemisphere of each subject. T_1 values higher than 2000 ms or smaller than 600 ms have been thresholded for display.

Figure 2.2 shows a representative map in greater detail with ROIs corresponding to the three brain tissues.

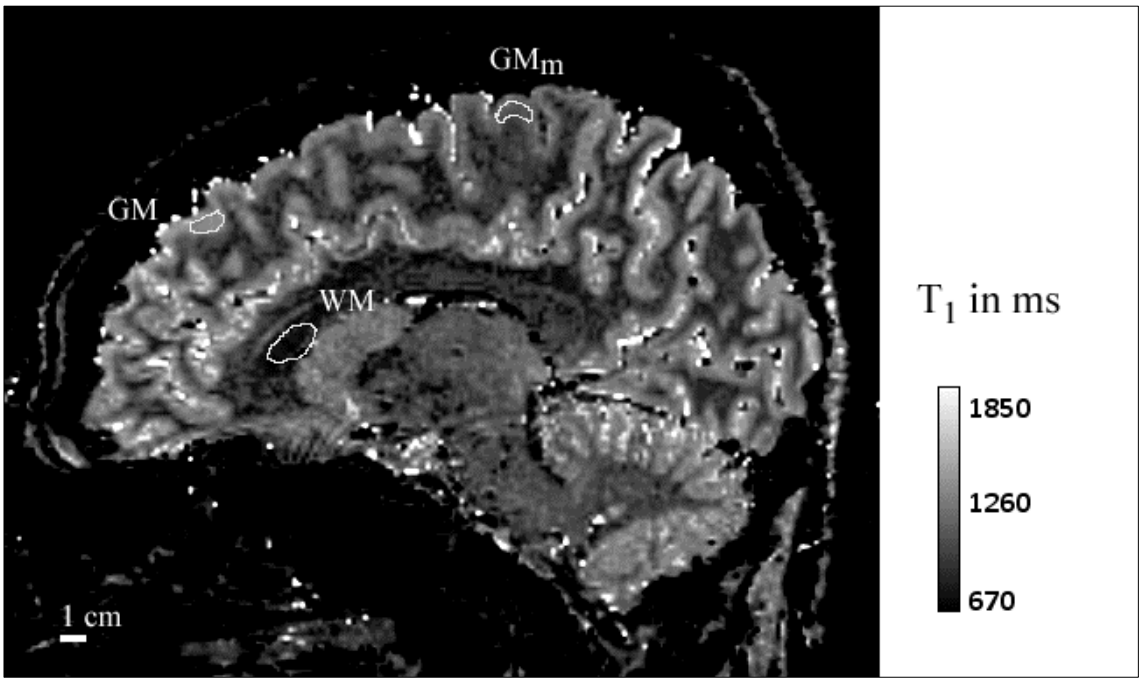

Figure 2.2: A representative T_1 map at 3T with ROIs corresponding to GM, GMm and WM.

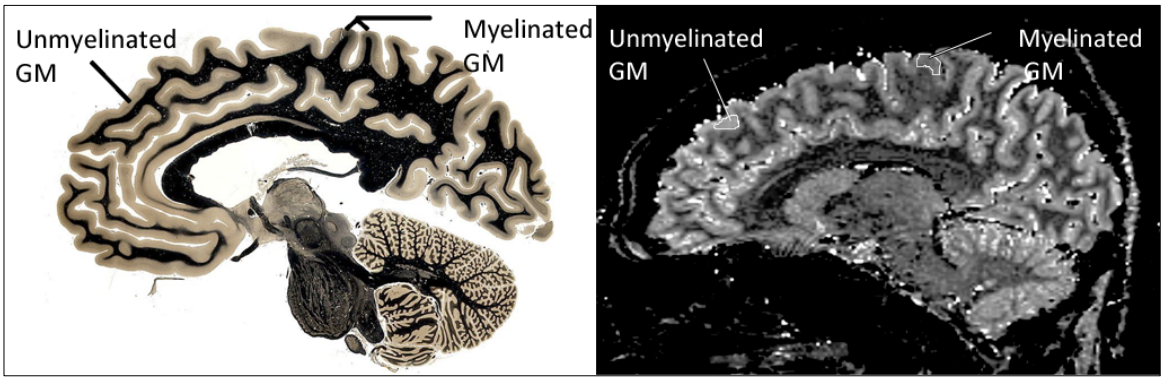

Figure 2.3: A comparison of a fiber-stained section (left- from http://www.brainmuseum.org) with a T_1 map (right), both approximately in the same location and orientation in the brain.

Figure 2.3 is a comparison of a representative T_1 map with a fiber-stained section in approximately the same brain location, obtained from the online atlas (http://www.brainmuseum.org) used to guide slice and ROI selection. Myelinated cortex appears darker in the fiber-stained section; myelination in the pre- and postcentral gyrus is clearly visible corresponding to the location of the primary motor and somatosensory cortex respectively. The frontal cortex has less myelin and appears to be lighter; this is where the ROI for unmyelinated or typical GM was placed.

Table 2.1 summarizes the mean T_1 values for n=5.

Tissue	**T_1 in ms (Mean ± SD, n=5)**
GM	1280 ± 20
GMm	1110 ± 40
WM	740 ± 30

Table 2.1: Mean T_1 values in the brain of healthy subjects (n=5) at 3 T. SD = Standard deviation of the sample.

WM T_1 was 740 ±30 ms, GM T_1 was 1280 ± 20ms, and GMm T_1 equalled 1110 ± 40 ms. These values are in good agreement with other studies at 3 T: for WM, T_1 in the genu of the corpus callosum is reported to be 721 ms (Lu *et al.*, 2005); for GM, T_1 in frontal gray matter is reported to be 1322 ms (Wansapura *et al.*, 1999). A difference in T_1 of 170 ± 40 ms (mean ± standard deviation of the paired differences, n=5) between GM and GMm was found across the subjects. Thus, the mean T_1 in GMm is 13 % shorter compared to that in GM. A mean

difference in T_1 of 540 ± 50 ms was measured between GM and WM across the subjects. The differences in T_1 values at 3T between the three tissues were significant at the $p<0.05$ level.

2.2.3 Discussions

Several methods for T_1 measurement, such as inversion recovery, saturation recovery and stimulated echoes, can be found in the literature; however, IR sequences are considered the gold standard for T_1 measurement (Crawley and Henkelman, 1988). The only problem with IR sequences is their long TR which makes the imaging time very long. This can be dealt with by employing a readout such as EPI, which is not only faster but also has the advantage that it does not affect the longitudinal magnetization. EPI has another great benefit of being routinely available on every clinical scanner, while some of the other comparatively efficient protocols such as Look-Locker (Look and Locker, 1970; Henderson *et al.*, 1999; Crawley and Henkelman, 1988) are not available on every platform. For these reasons, IR-EPI was chosen as the method of measuring and mapping T_1.

The measured T_1 values were compared with literature values to test their accuracy. Table 2.2 summarizes T_1 literature values at 3T for the three tissues that were measured.

Reference	Sequence	Age± SD/ Sex	WM		Cortical GM	
			Region	T_1±SD	Region	T_1±SD
(Gelman *et al.*, 2001)	TOMROP, MultS	29 ± 6,B	Frontal WM	847±43	PFC	1763±60
(Wansapura *et al.*, 1999)	Variable TR-SE, SS	28± 51,B	Frontal WM	838±18	Frontal GM	1322±34
(Wansapura *et al.*, 1999)	Variable TR-SE, SS	28 ± 51,B	-	-	Occipital GM	1283±37
(Wright *et al.*, 2008)	MPRAGE	24 ± 43,B	-	840±50	cGM	1600±110
(Zhu and Penn, 2005)	TESO-IRFSE,SS	34.3 ± 9.4,B	Genu-Corpus Callossum (CC)	724±33	Over All	1421±43
(Marques *et al.*, 2010)	MP2RAGE	34 ± 5,M	CC	780±40	Motor cortex	1320±70
(Marques *et al.*, 2010)	MP2RAGE	34 ± 5,M	-	-	Temporal cortex	1390±70
(Clare and Jezzard, 2001)	IR-EPI,MultS	31 ± 5	CC	820±40	-	-
(Lu *et al.*, 2005)	IR-GRASE(EPI RO), SS	28 ± 5, B	Genu-CC	721±68	Frontal GM	1209±109
(Lu *et al.*, 2005)	IR-GRASE(EPI RO)SS	28 ± 5, B	-	-	Occipital GM	1122±107
(Lin *et al.*, 2001)	FSE, SS	31.2 ± 10.3,B	-	791±27	-	1445±119

Table 2.2: A survey of T_1 measurements at 3T from the literature. The second column gives a short description of the MRI protocol used. B: both male and female, cGM: cortical GM, M: male, MultS: multiple slices, PFC: pre-frontal cortex, and SS: single slice.

A comparison of values in Tables 2.1 and 2.2 shows that T_1 values measured in this study correspond with values quoted in the literature. Of note is that values measured with IR-EPI in this study and in Lu *et al*. (Lu *et al.*, 2005) are lower than values measured with any other protocol. TOMROP (T-One by

Multiple Readout Pulses - (Gelman *et al.*, 2001) which is a variant of Look-Locker, results in the highest T_1 values.

Factors which may contribute to inaccurate T_1 measurements include non-ideal slice profiles, incomplete inversion, and subject motion due to long TR. Also, this study has focused on measuring mono-exponential T_1 recovery rates of hydrogen in water. Biological tissues usually consist of several compartments, each with water in a different molecular environment and hence with a different relaxation rate. However, it has been shown that the exchange rate between different compartments is faster than T_1 in any compartment (Hazelwood *et al.*, 1974) and therefore, a single T_1 recovery can be assumed in these calculations.

The T_1 values in these three tissues indicate a larger difference of 540 ms between the cortex and the underlying WM, and a smaller difference of 170 ms between cortical GMm and GM. This explains why overall anatomical contrast in T_1- weighted MRI is easier to obtain than intracortical contrast and that a careful optimization of the MRI protocols is needed to achieve greater intracortical contrast on the basis of smaller difference of 170 ms across the cortex.

2.3 Developing the MR techniques

The primary motor cortex, located in the most posterior position in the frontal lobe, is located in the anterior wall of the central sulcus and extends dorsally to the top of the hemisphere and anteriorly onto the precentral gyrus. It then traverses the precentral gyrus in a medio-lateral and slightly caudo-rostral fashion (Figure 2.4). On the other side of the central sulcus, in the parietal lobe, is

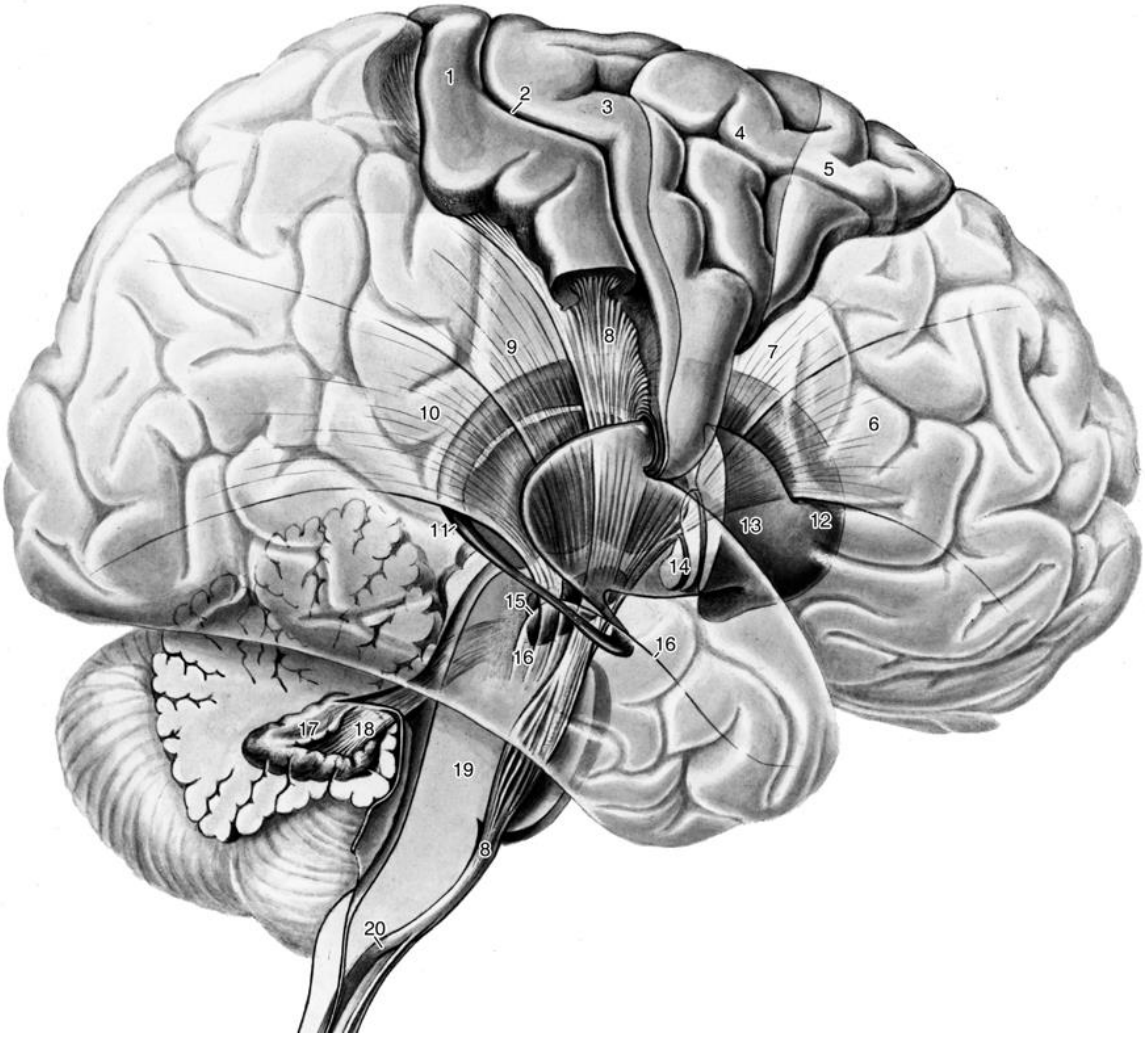

Figure 2.4: The primary motor cortex is labelled as 3. The primary somatosensory cortex, labelled as 1, is to the left of the primary motor cortex and separated from it by the central sulcus, labelled as 2. The non-primary motor cortex is labelled as 4 and 5. A detail of the rest of the labels can be found in the referenced text (Reprinted with permission-(Nieuwenhuys *et al.*, 2008)).

the primary somatosensory cortex (S1) in the postcentral gyrus. The location and anatomy of M1 therefore requires that the field-of-view (FOV) of the imaging experiment should be about an 8 cm thick coronal slab, centered at the central sulcus. This relatively thick slab ensures that the precentral gyrus is entirely

captured as required for the study of its morphology, taking into account person-to-person variations in the overall size of the brain and also including S1 for reference.

In this section, the optimization of MRI protocols is described to produce high quality images where M1 can be demarcated for quantitative measurements as required for this project. The need for optimization arises for a number of reasons, the foremost being resolution. Myelinated layers in M1 span about 2.2 mm of its 3.75 mm thickness, and are the deepest layers adjacent to WM (Zilles and Amunts, 2012). This indicates that sub millimeter resolution is needed to prevent WM signal from encroaching into voxels containing the myelinated cortical tissue and causing partial-voluming which will result in loss of contrast. The number of myelinated axons in the cortex is much smaller compared to their number in WM. This explains the relatively small T_1 variation of only 13 % across the cortex and 38% T_1 variation between the cortex and WM as measured in this study. As a result, the intracortical contrast, essential for delineation of the myelinated layers, is expected to be significantly lower than the WM-GM contrast in T_1-weighted images. In general, the parameters determining the contrast in T_1-weighted anatomical MRI also affect blurring as determined by the point spread function (PSF) (Deichmann *et al.*, 2000; Bock *et al.*, 2013). Therefore, it is necessary to optimize the sequence to achieve the greatest intracortical contrast with least blurring.

Scan time is yet another parameter to be optimized. Higher resolution images need more time to acquire, yet as scan time increases, the probability of subject's motion increases. Hence, resolution and contrast should be optimized while keeping the scan time short to reduce the possibility of motion.

Inhomogeneity in the receive (B_1^-) and transmit (B_1^+) radiofrequency field may result in loss of signal and contrast and produce an intensity shading artifact across the cortex. As the intracortical contrast is already low, it is therefore necessary to take measures to reduce this inhomogeneity as much as possible. In this work, post-processing involving an additional 3D scan with little T_1-weighting was applied to remove B_1^- and B_1^+ inhomogeneities.

2.3.1 3D pulse sequence for enhanced T_1 -weighted imaging

The 3D sequence that was chosen for T_1-weighted anatomical imaging of M1 inverts the longitudinal magnetization and then samples its recovery to the equilibrium value with a series of low angle, spoiled-gradient echoes (SPGR (GE), aka FLASH). This is called a MPRAGE (magnetization prepared rapidly acquired gradient echo) sequence on Siemens scanners. To get the same sequence on a GE scanner, a modified 3D Fast SPGR (spoiled gradient echo) was used.

The spoiled gradient echo block or SPGR (GE) used to sample the recovering magnetization is referred to as FLASH (fast low angle shot) (Figure 2.5). FLASH, in the absence of a magnetization preparation block before it,

usually employs a steady state of the longitudinal magnetization. This steady state is produced by multiple, closely spaced RF pulses which do not allow complete T_1 relaxation. RF-spoiling or a spoiler gradient at the end of each TR is used to disperse any remaining transverse magnetization (Figure 2.5). Thus, the FLASH signal is usually T_1 or proton-density –weighted depending on the flip angle of excitation pulses.

The steady-state magnetization (M_z) and signal (S_{SF}) in FLASH is written as follows (Nishimura, 1996):

$$M_z = \frac{M_0\,(1- e^{\frac{-TR}{T_1}})}{(1-\cos\alpha\, e^{\frac{-TR}{T_1}})} \qquad 2.2$$

$$S_{SF} = \frac{M_0\,(1- e^{\frac{-TR}{T_1}})}{(1-\cos\alpha\, e^{\frac{-TR}{T_1}})} \cdot \sin\alpha \cdot e^{\frac{-TE}{T_2^*}} \qquad 2.3$$

where α represents the angle of each excitation pulse, TE, the echo time when the free induction decay is re-phased by the gradient and M_0, the initial magnetization. Also, T_2^* represents the apparent or effective transverse relaxation time constant. The FLASH signal is maximum when α is equal to the Ernst angle (α_E) given by Equation 2.4.

$$\cos\alpha_E = e^{\frac{-TR}{T_1}} \qquad 2.4$$

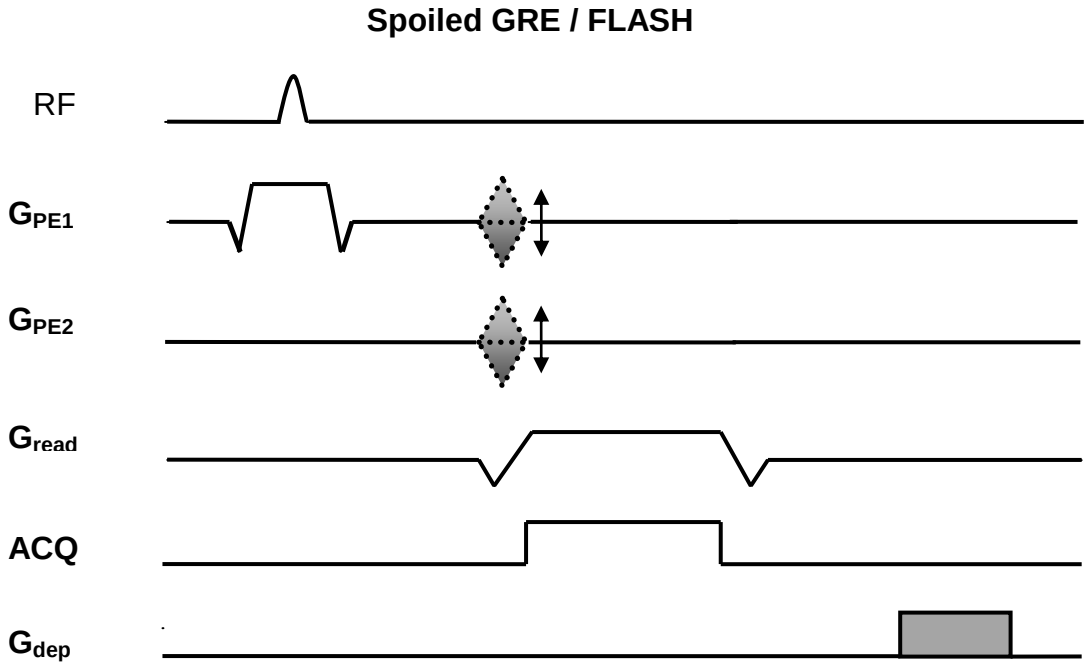

Figure 2.5: A schematic diagram of 3D, spoiled GRE sequence. ACQ stands for acquisition, G represents gradient, 'pe1' and 'pe2' are the two phase-encodes and 'dep' stands for dephasing. Shaded blocks with dashed-outline represent variable gradients.

Although steady state FLASH is frequently used in anatomical imaging for high SNR, the transient state can also be used to achieve higher contrast in the images. In FLASH, transient state is the period before the steady state in which contrast decreases after each α pulse before becoming constant in the steady state (Deichmann *et al.*, 2000). As the overall contrast in an image is mainly controlled by the central lines in k-space (Holsinger and Riederer, 1990), images with a desired contrast can be made with the transient state if the central lines are acquired in that state. The MPRAGE sequence utilizes this scheme to achieve enhanced contrast by employing centric phase encoding and

magnetization preparation such that the central lines of k-space are acquired in a transient state with enhanced contrast relative to the steady state of a typical FLASH sequence.

For magnetization preparation in MPRAGE, a 180° pulse is placed before the FLASH to invert the longitudinal magnetization. Figure 2.6 shows the effect of a 180° pulse in the rotating frame.

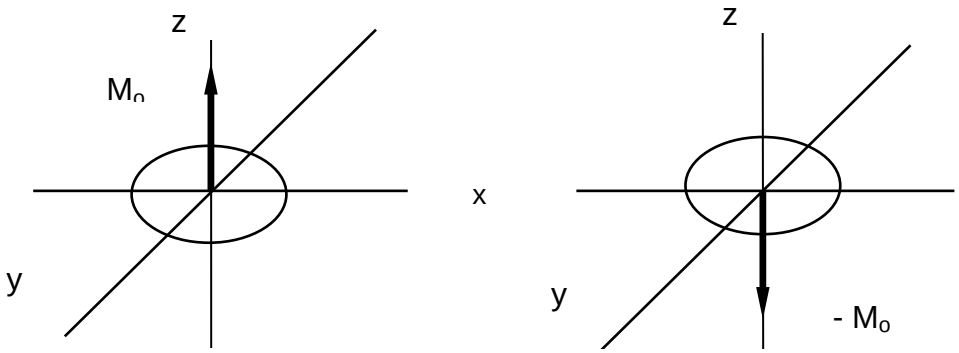

Figure 2.6: The role of 180° pulse is to invert the initial magnetization.

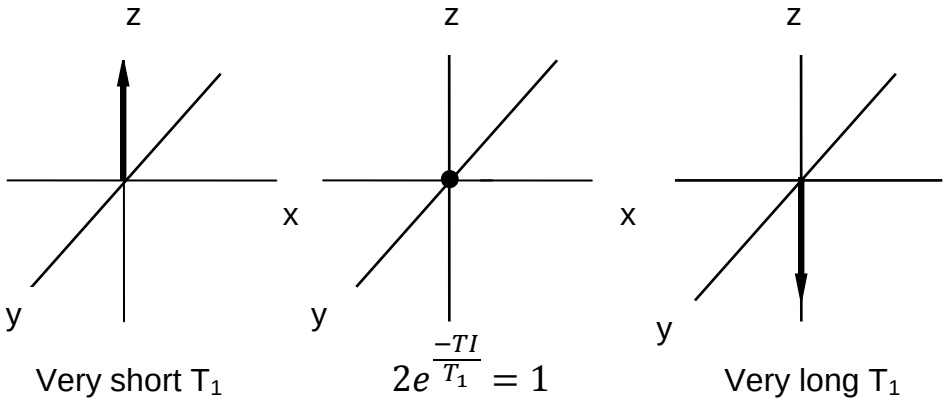

Figure 2.7: At time TI, tissues with the longest T_1 would have recovered the least while tissues with very short T_1 would have recovered to the starting value. For $2e^{-TI/T_1} = 1$, the longitudinal magnetization is passing through the null point. (Modified from (Sarty, 2005)).

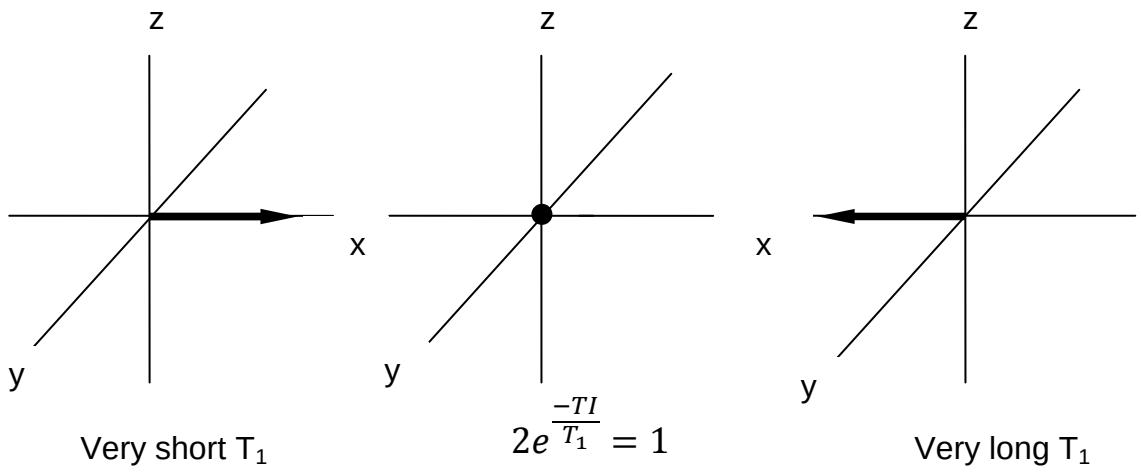

Figure 2.8: The outcome of applying a 90° excitation pulse to the inverted magnetization. (Modified from (Sarty, 2005)).

TI is the inversion time, between the 180° pulse and the beginning of the *α* train, during which the inverted longitudinal magnetization undergoes T_1 relaxation. Figure 2.7 shows three extreme possibilities of tissue relaxation at time TI. The excitation pulse *α* applied at time TI would tilt the partially recovered magnetization to the transverse plane (Figure 2.8). Thus, the effect of inversion is to double the dynamic range of magnetization available for excitation, from (0 to M_0) to ($-M_0$ to M_0). This results in enhanced T_1 contrast which is useful for differentiating fine structures in anatomical images.

Figure 2.9 is a schematic diagram of an MPRAGE sequence which consists of an inversion recovery block added before FLASH.

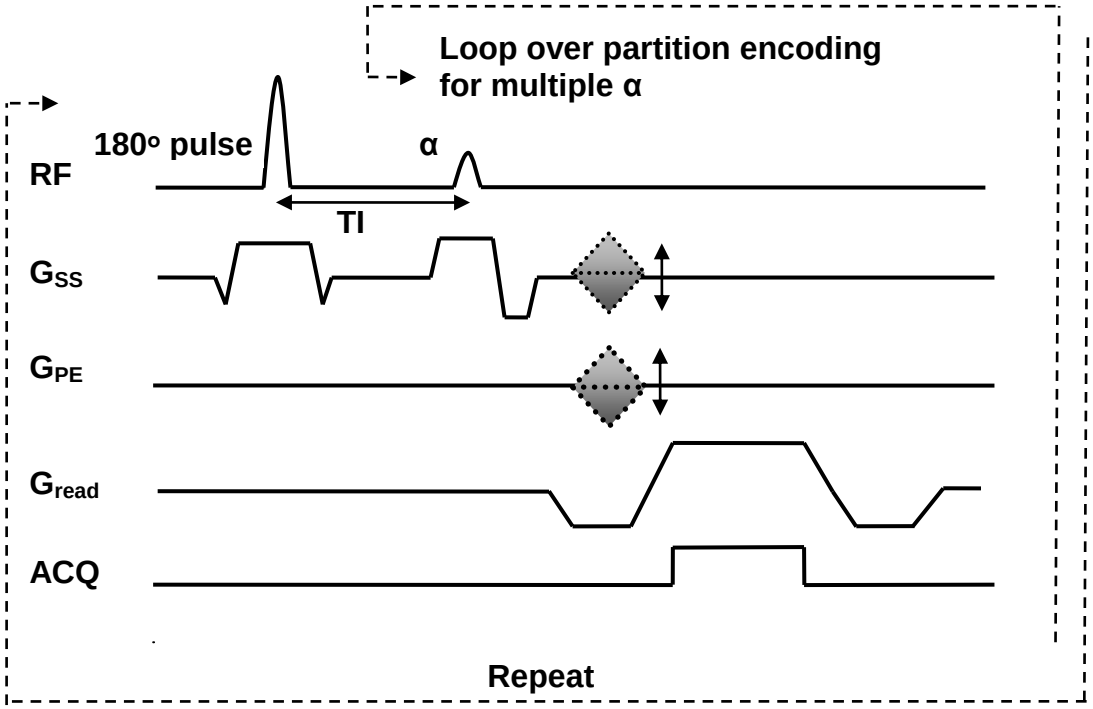

Figure 2.9: (Modified from (Haacke *et al.*, 1999)): Schematic diagram of MPRAGE. G_{ss}, G_{PE} and G_{read} represent the slice select, phase encoding and readout gradients respectively. Excitation angle in the FLASH block is *α* and TI is the inversion time.

2.3.2 Optimizing MPRAGE: Mathematics and simulations

The MPRAGE was optimized to achieve greater intra-cortical contrast at sub-millimeter resolution while keeping the imaging time short. Optimization was performed by simulating the MPRAGE signal in Matlab (MathWorks). For this purpose, the analytical signal equations derived by Deichmann *et al.* (Deichmann *et al.*, 2000) were used. The derivation is summarized in the following paragraphs.

Figure 2.10 is a simplified diagram of MPRAGE showing only the pulses that are played and time gaps between them.

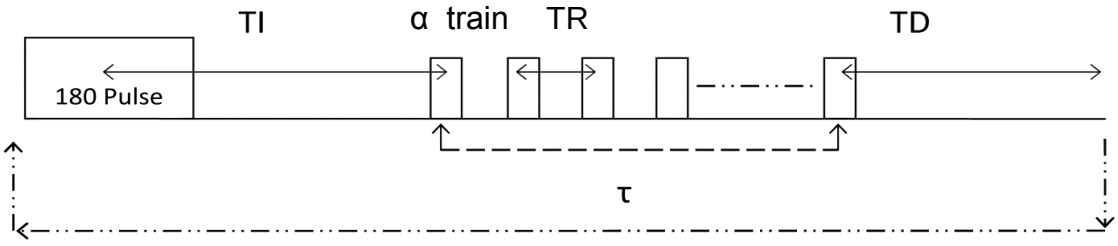

Figure 2.10: Pulses and inter-pulse gaps in MPRAGE.

In Figure 2.10, TI is the inversion time, TR is the spacing between consecutive *α* pulses and TD is the time delay at the end of *α*-train before applying the next pulse. The duration of the acquisition block is given by τ.

During the FLASH segment, magnetization reaches a steady state. If M_0 represents the equilibrium magnetization, M, the longitudinal magnetization, and T_1, the longitudinal relaxation time, then steady state magnetization can be found as follows:

If M^- and M^+ represent the longitudinal magnetization immediately before and after an *α*-pulse, then:

$$M^+ = M^- \cos\alpha \qquad 2.5$$

The longitudinal magnetization $M(\mathrm{t})$ at any time t between any two consecutive alpha pulses, can be written as:

$$M(t) = M^+ \cdot e^{\frac{-t}{T_1}} + M_0(1 - e^{\frac{-t}{T_1}}) \qquad 2.6$$

The magnetization M_1 just before the FLASH block is the same as that before the first *α*-pulse, $M^- = M_1$, and hence $M(t)$ becomes:

$$M(t) = M_1 \cos\alpha \cdot e^{\frac{-t}{T_1}} + M_0(1 - e^{\frac{-t}{T_1}}) \quad 2.7$$

Just before the second α-pulse,

$$M(TR) = M_1 \cdot \cos\alpha \cdot e^{\frac{-TR}{T_1}} + M_0(1 - e^{\frac{-TR}{T_1}}) \quad 2.8$$

Now, this longitudinal magnetization is flipped by the second *α*-pulse, and then it evolves according to Equation 2.6. Extending this framework, we can write the magnetization just before an *n*th *α*-pulse as

$$M(nTR) = M_{(n-1)TR} \cos\alpha \cdot e^{\frac{-TR}{T_1}} + M_0(1 - e^{\frac{-TR}{T_1}}) \quad 2.9$$

Now, one can solve it for the steady state value, M_0^*, which must satisfy

$$M_0^* = M_0^* \cos\alpha \cdot e^{\frac{-TR}{T_1}} + M_0\left(1 - e^{\frac{-TR}{T_1}}\right) \quad 2.10$$

Hence,

$$M_0^* = M_0 \frac{1 - e^{\frac{-TR}{T_1}}}{1 - \cos\alpha \cdot e^{\frac{-TR}{T_1}}} \quad 2.11$$

One can define an effective relaxation time, T_1^*, (Deichmann and Haase, 1992) as:

$$e^{\frac{-TR}{T_1^*}} = \cos\alpha \cdot e^{\frac{-TR}{T_1}} \quad 2.12$$

On rearranging, this yields:

$$\frac{1}{T_1^*} = \frac{1}{T_1} - \frac{\ln(\cos\alpha)}{TR} \qquad 2.13$$

The steady-state magnetization, M_0^*, now becomes:

$$M_0^* = M_0 \frac{1 - e^{\frac{-TR}{T_1}}}{1 - e^{\frac{-TR}{T_1^*}}} \qquad 2.14$$

Now, using the effective relaxation time (T_1^*) and the steady-state magnetization (M_0^*), and following the relaxation trend described in Equation 2.6, one can write M_2, the magnetization after the first acquisition block of τ seconds, as:

$$M_2 = A_1 + B_1 \cdot M_1 \qquad 2.15$$

where

$$A_1 = M_0^* \left(1 - e^{\frac{-\tau}{T_1^*}}\right) \text{ and } B_1 = e^{\frac{-\tau}{T_1^*}} \qquad 2.16$$

During the time delay TD, magnetization recovers at the normal rate T_1. At the end of TD, magnetization is given by:

$$M_3 = A_2 + B_2 \cdot M_2 \qquad 2.17$$

with

$$A_2 = M_0 \left(1 - e^{\frac{-TD}{T_1}}\right) \text{ and } \quad B_2 = e^{\frac{-TD}{T_1}} \qquad 2.18$$

After *TD*, there is an inversion pulse which leaves the magnetization M_3 as $-M_3$. Therefore, after the inversion time *TI*, the magnetization has the value:

$$M_4 = A_3 + B_3 \cdot M_3 \qquad 2.19$$

with

$$A_3 = M_0\left(1 - e^{\frac{-TI}{T_1}}\right) \text{ and } \quad B_3 = e^{\frac{-TI}{T_1}} \qquad 2.20$$

Notice that using Equation 2.17 for M_3, M_4 can be written as

$$M_4 = A_3 + B_3(A_2 + B_2 \cdot M_2)$$

$$M_4 = A_3 + B_3 \cdot A_2 + B_3 \cdot B_2 \cdot M_2 \qquad 2.21$$

And using M_2 from Equation 2.15, M_4 which is the magnetization just before the next FLASH block, is given by:

$$M_4 = A + B \cdot M_1$$

where

$$A = A_3 + A_2 \cdot B_3 + A_1 \cdot B_2 \cdot B_3$$

$$\text{and} \quad B = B_1 \cdot B_2 \cdot B_3 \qquad 2.22$$

In the outer 2D loop, a steady state is reached after a few complete cycles. With linear phase encoding in this direction, the steady state would already have been reached when the central k-space lines determining the overall contrast are acquired. Therefore,

$$M_4 = M_1 \text{ and } M_1 = \frac{A}{1-B} \qquad 2.23$$

For brevity, let

$$EI = e^{\frac{-TI}{T_1}}, \qquad ED = e^{\frac{-TD}{T_1}}, \qquad E\tau^* = e^{\frac{-\tau}{T_1^*}},$$

$$ETR = e^{\frac{-TR}{T_1}} \text{ and } ETR^* e^{\frac{-TR}{T_1^*}} \tag{2.24}$$

Using Equations 2.14, 2.15, 2.18, 2.20, 2.23 in Equation 2.22, M_1 can be explicitly written as

$$M_1 = M_0 \frac{(1-EI) - EI.(1-ED) - ED \cdot EI \cdot \frac{1-ETR}{1-ETR^*}(1-E\tau^*)}{1 + ED \cdot EI \cdot E\tau^*} \tag{2.25}$$

For centric phase encoding in the 3D direction (inner loop), the central k-space lines are acquired first and determine the overall contrast in the image. The signal at the center of k-space, S_c, would not have any T_1^* relaxation losses and can simply be written as in Equation 2.26 below.

$$s_C = M_1 \sin\alpha \tag{2.26}$$

In general, if *n* represents one of the N_{pe1} phase encoding steps in the inner loop, then the signal for this line is:

$$s_C = \left\{ M_1 e^{\frac{-nTR}{T_1^*}} + M_0^*(1 - e^{\frac{-nTR}{T_1^*}}) \right\} \sin\alpha \tag{2.27}$$

Equation 2.27 indicates that the signal is decaying exponentially with N_{pe1}. It also tells that the sequence parameters that determine the signal and contrast are the excitation angle *α,* time delays TI and TD, and length of FLASH acquisition block τ. As τ is a product of TR and number of phase encodes in the inner loop, N_{pe1}, the signal will also depend on image resolution. Furthermore, at

a given resolution, changing TI or TD will inevitably change the imaging time. It was decided to keep imaging time at fifteen minutes or shorter to reduce the probability of motion and to make the protocol more applicable to clinical imaging, remembering that the motor cortex was to be imaged at 0.7 mm isotropic resolution to gain better resolving power across the cortex. The objective of this optimization, hence, was to find values α, TI, and TD that would produce the greatest contrast with least blurring at 0.7 mm isotropic resolution in 15 min at a field strength of 3 T.

Using Equation 2.27, the signal $S_c(t)$ was simulated in Matlab as the signal over centric k-space in the first segment of FLASH. t in $S_c(t)$ indicates that this signal evolves with phase encodes, N_{pe1}, i.e. time. The signal equation also includes the tissue parameters, T_1, and proton density, ρ. T_1 values measured here were used to simulate the signal for each of the tissues GM, GMm and WM. The proton density determines the initial magnetization, M_o, for these tissues. The proton density was estimated from a non-human-primate study (Bock *et al.*, 2009) (Table 2.3). As an estimation of the signal in any voxel, the point spread function (PSF) was calculated as the inverse Fourier transform, $S(f)$, of $S(t)$. The contrast between any two tissues was determined as the absolute difference in the peaks of their PSFs(Deichmann *et al.*, 2000). Representing the peak of PSF as A:

$$\text{Calculated PSF contrast} \equiv \text{Contrast}_{\text{PSF}} = \left|\text{A}_{\text{tissue1}} - \text{A}_{\text{tissue2}}\right| \qquad 2.28$$

Image blurring was calculated from the value of the pixel in the PSF immediately next to the peak pixel, expressed as a percentage of the peak (Figure 2.11).

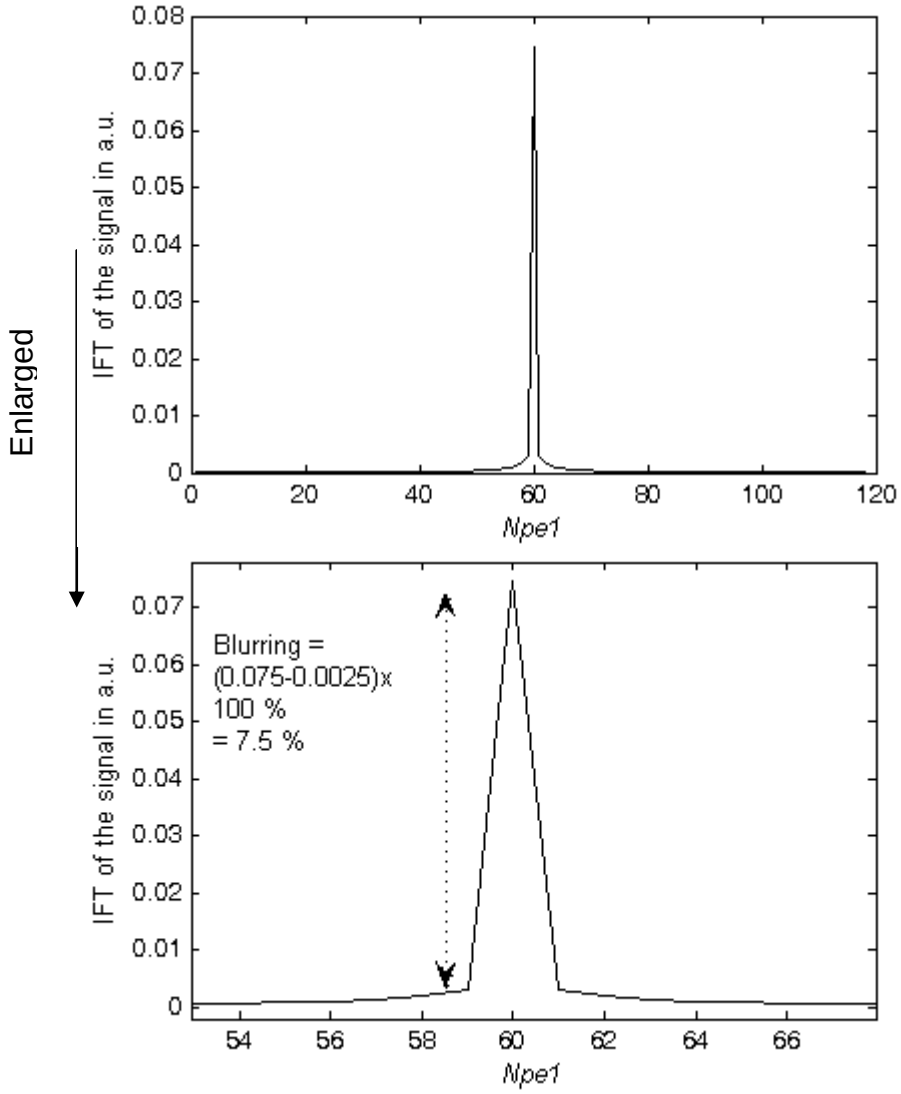

Figure 2.11: Blurring was calculated as the percentage difference between the peak and the adjacent pixel in the inverse Fourier transform of the stimulated signal in any tissue.

The sequence time can be calculated as:

$$\text{time} = (TI + \tau + TD) \cdot N_{pe2} \qquad 2.29$$

where N_{pe2} represents the number of phase encodes in the outer loop.

The optimization was performed in the following order:

The effect of increasing TD on the MPRAGE signal, contrast and blurring was simulated. Next, the effect of varying TI and α, while keeping the imaging time constant by correspondingly adjusting TD, was evaluated (Table 2.4). The acquisition matrix was chosen to cover an 8 cm FOV with 0.7 mm isotropic resolution.

Tissue	T_1 in ms	ρ
GM	1283	1.0
GMm	1112	0.97
WM	735	0.86

Table 2.3: The tissue parameters, T_1 and relative proton density, ρ, used in simulations.

Parameter	Value
$FOV_{readout}$ x FOV_{pe1} x FOV_{pe2}	240 mm x 80 mm x 192 mm
$N_{readout}$ x N_{pe1} x N_{pe2}	344 x 118 x 274
TR (between successive α pulses)	10 ms
TI	100: 3000 ms
TD	100: 6000 ms
α	1°: 20°

Table 2.4: The sequence parameters used in simulations.

Noise in magnitude MRI images is considered to be Rician and depends on voxel size, receiver bandwidth and number of averages in the image acquisition (Gudbjartsson and Patz, 1995). In other words, noise in the image depends on the acquisition block, the FLASH block in this case. Since the FLASH

parameters remain unchanged in simulations, the noise can be considered to remain unchanged when TD and TI are changed. Thus, variations in signal and contrast are proportional to changes in SNR and contrast-to-noise ratio (CNR) respectively.

2.3.3 Results of the MPRAGE optimization

In the first part of the simulations, TD was varied over 0-10,000 ms in steps of 50 ms at a fixed TI of 1000 ms and FLASH excitation angle of 12°. Using $2e^{\frac{-TI}{T_1}} = 1$, TI was calculated to be greater than the time required for magnetization in all three tissues of interest to pass through the null point assuming complete relaxation before the inversion pulse. The initial value for α was chosen to be greater than the Ernst angle in each tissue to ensure T_1 contrast.

The simulations showed that GM-WM contrast as well as GMm-GM contrast increases with increasing TD. When TD is of the order of several T_1, the contrast reaches a saturation value indicating that the magnetization in the tissues have relaxed to the equilibrium value before the next inversion pulse. It is thus advantageous to image at a longer TD to a point to achieve greater contrast; however, any contrast gains will diminish as one approaches this saturation. Figure 2.12 shows the plot of tissue contrast vs. TD.

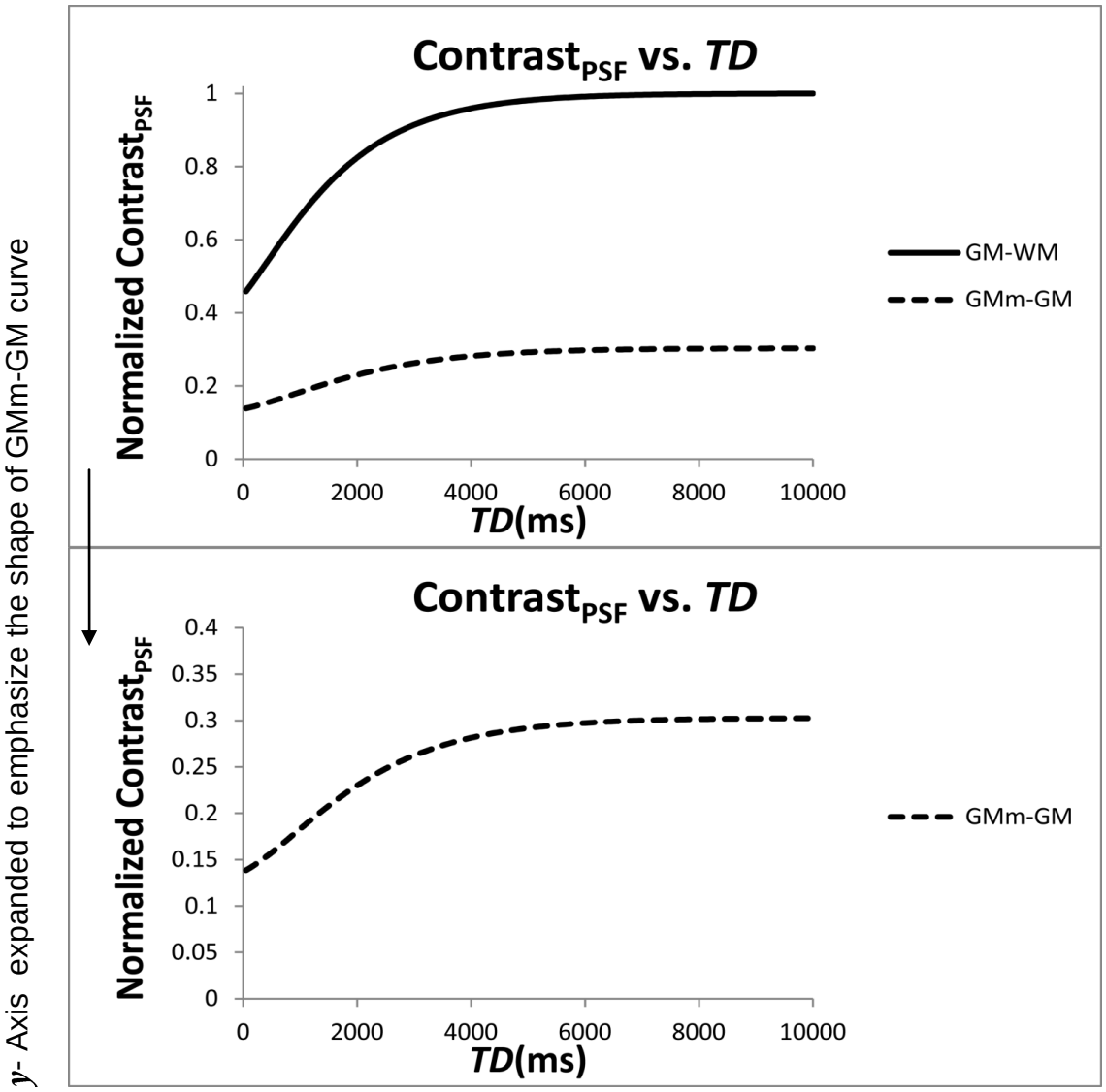

Figure 2.12: Graphs showing variation of contrast$_{PSF}$ with increasing TD. Both panels have the same TI = 1000 ms and α = 12°. The lower panel has a magnified y-range to show the similarities in GM-WM and GMm-GM contrast$_{PSF}$.

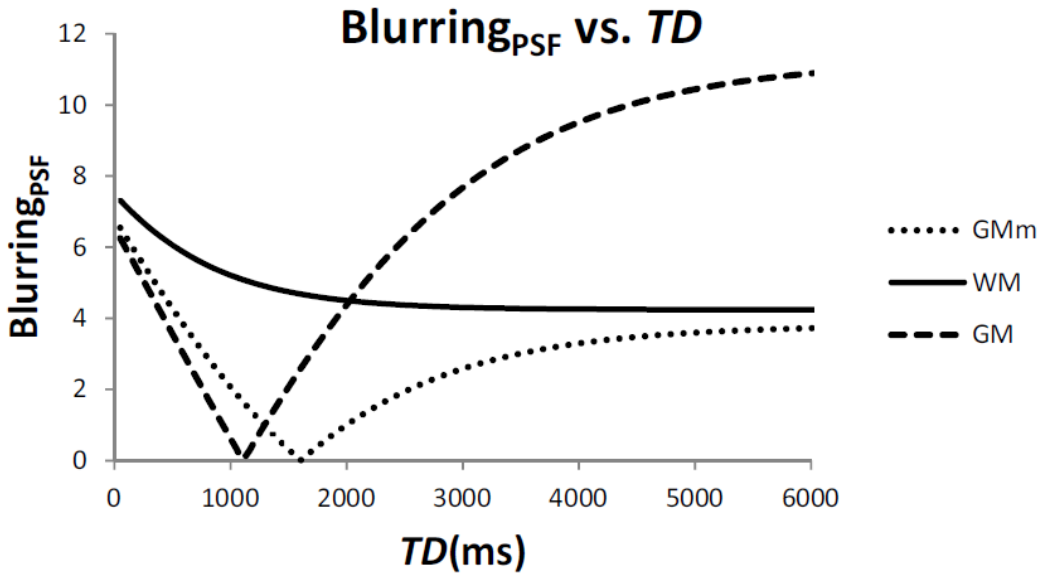

Figure 2.13: Image blurring as the value of the pixel adjacent to the peak pixel in PSF for each of the three tissues, expressed as percent of the peak. TI = 1000 ms and α = 12°.

Image blurring, which is determined by the evolution of magnetization over the FLASH segment (Deichmann *et al.*, 2000; Bock *et al.*, 2013) also changes with TD. The graph in Figure 2.13 shows the variation of blurring with TD for all the three tissues under the same conditions as in Figure 2.12. Figure 2.13 shows that no value of TD results in a minimum blurring for all three tissues simultaneously. A TD between 1000-2000 ms will produce less than 2% blurring for GM and GMm and the final choice will depend on other parameters such as total scan time.

Next, the effect of varying TI and *α* together, while keeping the scan time fixed at 15 min by appropriately adjusting TD, was assessed for effect on contrast. For the selected imaging matrix (Table 2.4), a 15 min scan results if

successive inversion pulses are 3270 ms apart (Equation 2.29). Therefore, for each TI, TD was calculated as:

$$\text{cycle } TR \stackrel{\text{def}}{=} \text{Time between two successive } 180^0 \text{ pulses} = 3270 \text{ ms}$$

$$TD(\text{ms}) = \text{cycle } TR - TI - \tau \qquad 2.30$$

The results are shown as contour plots in Figures 2.14.

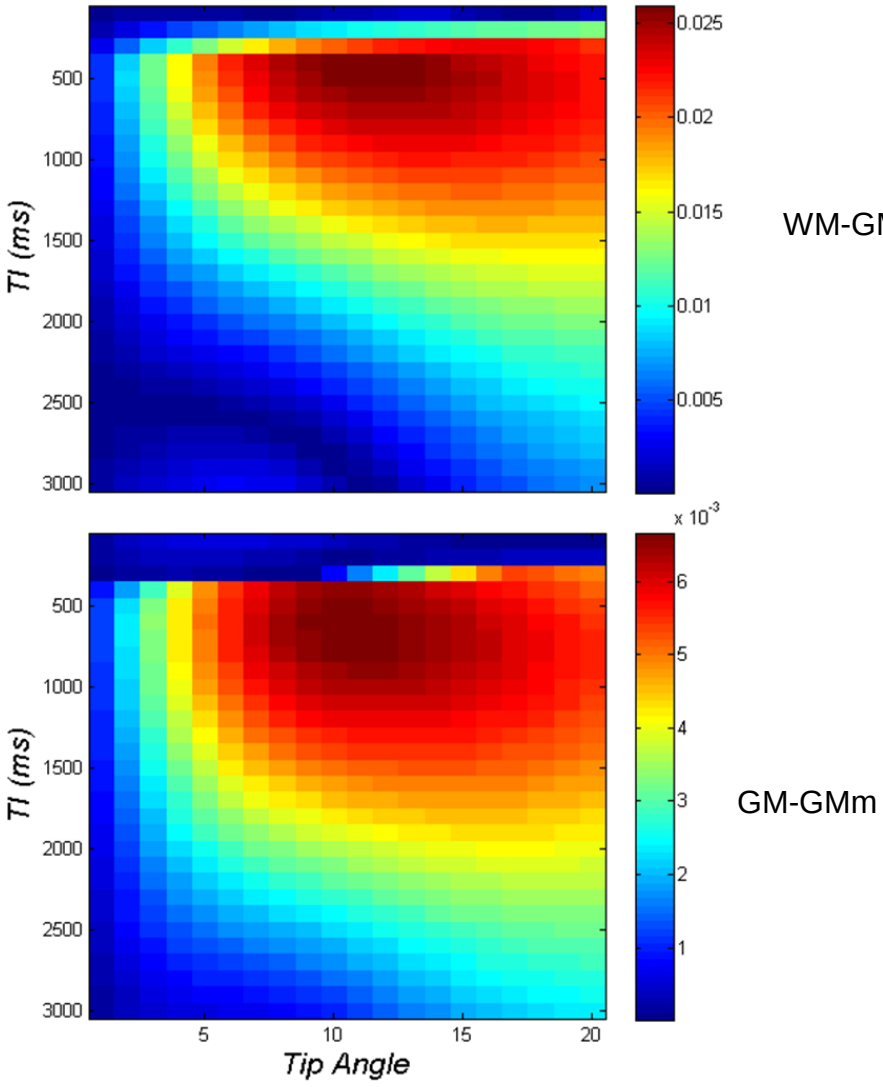

Figure 2.14: The variation of WM-GM (top) and GM-GMm (bottom) $contrast_{PSF}$ with α and TI. The imaging time and imaging matrix are kept constant.

The plots in Figures 2.14 show that both, the overall anatomical contrast (WM- GM) and the intracortical contrast (GM-GMm) are at their respective peaks for TI between 500: 1000 ms and α between 9°: 12°. To avoid phase errors due to a negative signal resulting from too short a TI, it is important to look at the magnetization plot for the tissue with the longest T_1 (i.e. GM) to make sure that TI is greater than its null point. Figure 2.15 shows the behavior of magnetization for GM for changing α and TI simultaneously while keeping the imaging time and imaging matrix fixed. The plot shows that the GM magnetization is negative for TI up to ≈750 ms for all values of α. This narrows the range of TI for the best contrast to 800: 1000 ms. Corresponding values for TD are 1090: 1290 ms.

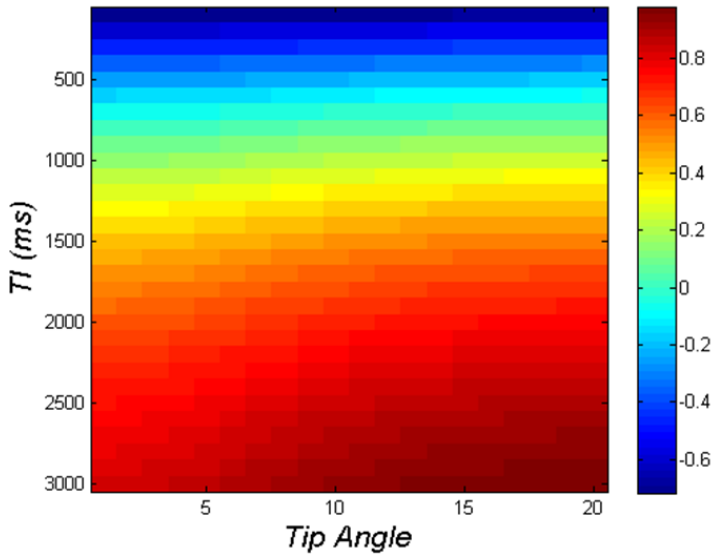

Figure 2.15: Magnetization for GM when α and TI are changed simultaneously.

Next, image blurring for WM, GM and GMm, for a 15 minute scan with variable TI (100: 3000 ms) and α (1°: 20°) was investigated (Figures 2.16).

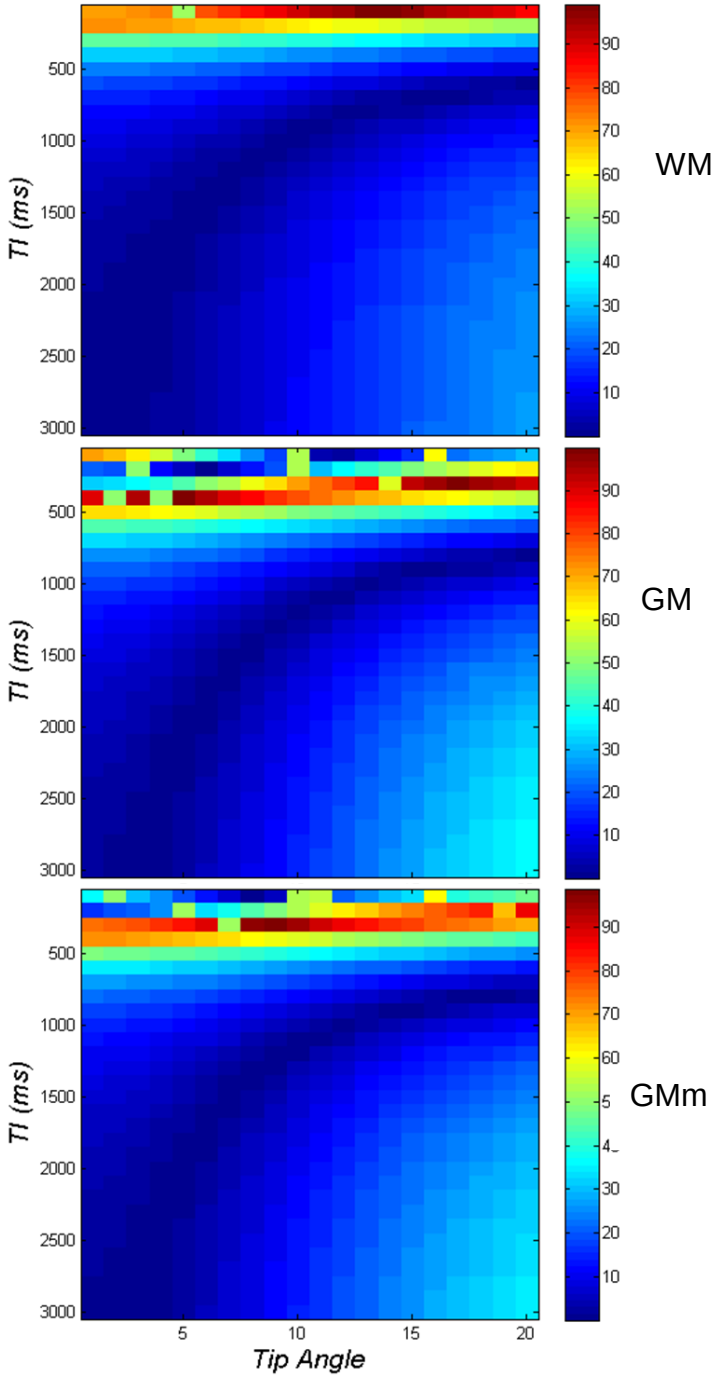

Figure 2.16: Image blurring, defined as value of the pixel adjacent to the peak in PSF expressed as percent of the peak, for WM (top), GM (middle) and GMm (bottom). Image blurring for very short TIs for GM and GMm exhibits non-uniform variations likely due to the signal crossing the null point.

All three plots in Figure 2.16 show that blurring is high for large *α* and for small TI. Blurring for GM (Middle- Figure 2.16) and GMm (Bottom- Figure 2.16) was investigated for the previously arrived at range for *α* (9°: 12°) and TI (800: 1000 ms). It was found that within this range, blurring is the least (less than 5% for both GMm and GM) for *α* = 12° at TI = 1000 ms. Also, WM experiences less blurring compared to the other two tissues within this range of *α* and TI.

Combining all the results, the optimized parameters for MPRAGE are *α* = 12° at TI = 1000 ms and TD = 1100 ms for a 15 min scan at 0.7 mm isotropic resolution using a 3 T MRI scanner.

2.3.4 Reducing radio-frequency field inhomogeneities

Intensity inhomogenieties due to transmit (B_1^+) and receive (B_1^-) radio frequency fields are present in almost all brain MRIs to some extent (Belaroussi *et al.*, 2006; Arnold *et al.*, 2001). These artifactual variations in intensity can cause errors in tissue classification. In order to minimize their effect, the technique proposed by Van de Moortele *et al*., which makes use of an additional image with very little T_1 weighting to significantly reduce the transmit and receive field effects (Marques *et al.*, 2010; Van de Moortele *et al.*, 2009) was used. The additional image is usually obtained using a FLASH sequence with very small FA (4º in our case). The T_1 -weighted image is then divided by the FLASH image during post-processing to reduce B1 effects. Given below is a brief theoretical explanation, based on the work by Marques *et al*., of how the technique works (Marques *et al.*, 2010).

The MPRAGE signal S_{MP} is weighted by the receive field profile B_1^- as follows:

$$S_{MP} \propto M_{MP} \cdot |B_1^-| \cdot \sin(\alpha) \cdot e^{\frac{-TE}{T_2^*}} \quad 2.31$$

where M_{MP} is the MPRAGE magnetization and α is the prescribed flip angle (FA) in the FLASH block of MPRAGE. If the B_1^- is not uniform, but changes with spatial position in the image, then the MPRAGE signal will also change with position.

The flip angle is proportional to the transmit field profile B_1^+ (Bernstein *et al.*, 2004; Haacke *et al.*, 1999):

$$FA \propto \gamma \cdot B_1^+ \cdot \tau_{FA} \quad 2.32$$

where γ is the gyromagnetic ratio of the spins and τ_{FA} is the duration of RF pulse. In the presence of transmit field inhomogeneities, B_1^+ changes with spatial position in the image. Thus, the actual FA deviates from the prescribed FA by an amount governed by B_1^+, and it also becomes a function of the spatial position. Under these circumstances, one can define the actual FA as a fraction of the prescribed FA:

$$Actual\ FA = Prescribed\ FA \cdot B_1^+ \quad 2.33$$

Therefore, the MPRAGE signal, which now depends on the spatial position in the image, is given by:

$$S_{MP} \propto M_{MP} \cdot |B_1^-| \cdot \sin(\alpha |B_1^+|) \cdot e^{\frac{-TE}{T_2^*}} \quad 2.34$$

Similarly, including the receive and transmit field inhomogeneities, the FLASH signal S_F is given as:

$$S_F \propto M_F \cdot |B_1^-| \cdot \sin(\beta |B_1^+|) \cdot e^{\frac{-TE}{T_2^*}} \quad 2.35$$

Here, M_F is the FLASH magnetization and β is the nominal FA for FLASH. Considering very small flip angles, the first order approximation $sin(\theta) \approx \theta$ and assuming the same echo time, band width and receive and transmit coil profiles for both acquisitions, the ratio of the two signals simplifies to the following.

$$\frac{S_{MP}}{S_F} = \frac{M_{MP} \cdot \alpha |B_1^+|}{M_F \cdot \beta |B_1^+|} \quad 2.36$$

The ratio is thus independent of the receive field inhomogeneity B_1^-. Taking a ratio of two images with the same B_1^- profiles, therefore, is advantageous in removing that inhomogeneity effect.

As for the transmit field effects, it should be noted that the two magnetizations M_{MP} and M_F also depend on respective FAs. Therefore, taking into account the variation of FA due to B_1^+ inhomogeneity, the ratio should be written as in the equation below.

$$\frac{S_{MP}}{S_F} = \frac{M_{MP}\{x,y,z\} \cdot \alpha}{M_F\{x,y,z\} \cdot \beta} \quad 2.37$$

The notation $M_{MP/F}\{x,y,z\}$ is used to indicate variation of $M_{MP/F}$ with spatial coordinates x, y and z in the image, as a result of change in FA due to

B_1^+. However, the magnetization M_{MP} does not depend on FA the same way as M_F does. The steady-state longitudinal magnetization in FLASH is given by Equation 2.2.

$$M_F = M_0 \frac{1 - E_{T_1}^{TR}}{1 - E_{T_1}^{TR}.\cos\beta} \qquad 2.2$$

Using a small angle approximation (since $\beta = 4^\circ$),$\cos\beta \approx 1$, M_F becomes M_0 and spatial dependence of M_F can be ignored.

The longitudinal magnetization in MPRAGE, given in Equation 2.25, has many terms that depend on FA. Equation 2.25 is reproduced here with the simplification that terms independent of spatial dependence $(TISP)$ are not elaborately written.

$$M_{MP} = M_0 \frac{TISP1 - \frac{TISP2}{\left(1 - E_{T_1^*}^{TD}\right)} \cdot \left(1 - E_{T_1^*}^{\tau}\right)}{1 + TISP3 \cdot E_{T_1^*}^{\tau}} \qquad 2.38$$

Here, T_1^* is the effective longitudinal relaxation time, as defined in the Equation 2.14, which depends on the FA.

Therefore, dividing the two images or the two magnetizations cannot fully eliminate the B_1^+ effects. However, in the small angle limit and assuming $TD \gg T_1, T_1^*$ approaches T_1. Therefore, M_{MP} can be simplified to the following expression.

$$M_{MP} = M_0 \left[1 - 2E_{T_1}^{TI}\right] \qquad 2.39$$

Under these restricted conditions, the ratio image will be independent of FA and hence will not be affected by the transmit field inhomogeneity. It is understood that $TD \gg T_1$ does not hold for all the tissues, and therefore, the B_1^+ effects are not completely removed. But the ratio image would have significantly reduced B_1^+ and completely removed B_1^- effects.

2.3.5 Discussion and conclusions

The goal of sequence optimization was to enhance intracortical contrast based on the small T_1 difference (171 ms in our study) between GMm and GM in the cortex. Typically, anatomical imaging is optimized on the basis of the larger T_1 difference (548 ms in our study) between WM and GM.

Simulations indicated that contrast increases with TD before saturating at a TD ≈ 6000 ms. Keeping in mind that T_1 = 1283 ms for GM at 3T (the slowest relaxing tissue in the study), this behavior confirms the 5 x T_1 rule of thumb, i.e. as TD increases, longitudinal magnetization has a longer time to relax, eventually reaching its equilibrium value at about 5 x T_1 after which there cannot be an increase in contrast. It is important to notice that this result is general. Although the simulations assumed a specific matrix size, excitation angle and TI, these parameters do not affect the rate of post FLASH relaxation.

The simulations indicate that there is no unique value of TI and *α* that would result in minimum blurring in all three tissues simultaneously. We

therefore, chose the parameters TI and α so that no tissue has more than a few percent blurring with GMm having the least blurring.

As discussed before, the goal of optimization was to find the set of parameters that will produce the greatest contrast with least blurring at 0.7 mm isotropic resolution in 15 min at field strength of 3 T. It was found, based on simulations, that α = 12°, TI = 1000 ms and TD = 1100 ms should result in the best anatomical as well as intracortical contrast under these conditions. These values are specific to the current imaging protocol and might change if for example a different resolution or scan time were chosen.

Dividing the T_1-weighted images with pre-dominantly proton density -weighted images is advantageous for completely removing the effects of receive field inhomogeneities when both images have same the receive field profiles. This transmit field inhomogeneity is also significantly reduced. Also, a small flip angle of 4^0 for the FLASH images resulted in insignificant T_1-weighting in the images. The FLASH images are thus mainly pd-weighted and division of the T_1-weighted images with the FLASH images has the further effect of enhancing the T_1 contrast in the images

The anatomical imaging protocol optimized to achieve enhanced intracortical contrast based on myelin thus consists of making T_1-weighted images with optimized MPRAGE and FLASH images.

2.4 Demonstrating imaging of M1 in subjects

To verify the findings of the MRI optimization, one subject was scanned with the protocol consisting of optimized MPRAGE and FLASH. To compare the effect of lengthening TD on contrast, a second MPRAGE image with scanner's default TD of 0 ms (referred to as short TD-MPRAGE) was also acquired in the same subject. To increase the SNR, the MPRAGE and FLASH scans were repeated twice. The entire imaging was performed in one session.

2.4.1 Methods

A healthy 25 year old male subject was scanned at St. Joseph's Healthcare using a 3 T, GE MR 750 scanner (software version 22.0), with a body transmit coil (GE) and a 32-channel receive-only head coil (MR Instruments). The protocol was approved by Research Ethics Board of the institution and informed consent was obtained from the subject prior to imaging.

The 3D acquisition was performed over an 8 cm slab, approximately in the centre of the anterior-posterior (AP) axis. The slab covered the entire head along superior-inferior (SI) and right-left (RL) axes, and was rotated about the AP axis to ensure the alignment of anterior and posterior commissures (AC-PC). A set of oblique-coronal slices was thus acquired. The same FOV and slab was used for all the images. A slab-selective, 180° sinc pulse was used for inversion in both MPRAGE images. Table 2.6 lists the parameters for all the scans: optimized MPRAGE, short TD-MPRAGE and FLASH.

Parameter	Optimized MPRAGE	Short TD-MPRAGE	FLASH
$FOV_{readout}$ x FOV_{pe1} x FOV_{pe2}	240 mm x 80 mm x 192 mm	240 mm x 80 mm x 192 mm	240 mm x 80 mm x 192 mm
$N_{readout}$ x N_{pe1} x N_{pe2}	344 x 118 x 274	344 x 118 x 274	344 x 118 x 274
Resolution	0.7 mm isotropic	0.7 mm isotropic	0.7 mm isotropic
Receive Band Width	31.25 KHz	31.25 KHZ	31.25 KHZ
TR (between successive α pulses)	9.9 ms	9.9 ms	9.9 ms
Excitation angle α	12°	12°	4°
TI	1000 ms	1000 ms	-
TD	**1100 ms**	**0 ms**	-
Time	15 min	10 min	5.3 min
Repeats	2	2	2

Table 2.5: Sequence parameters for the optimized MPRAGE, short-TD MPRAGE and FLASH scans. TD (indicated in bold) is the only parameter that was assigned different values for the optimized MPRAGE and short-TD MPRAGE scans.

2.4.1.1 Comparison of optimized- and short TD-MPRAGE

In the MPRAGE images, ROIs were drawn in regions of GM, WM, GMm in multiple sagittal slices using the software Amira (Visage Imaging). ROIs for GMm were drawn in the pre- and post-central gyri and sulci while ROIs for GM were drawn in the unmyelinated frontal cortex. ROIs for WM were drawn in the subcortical WM in the proximity of the GM and GMm ROIs. All the three ROIs in any one slice were drawn close to each other to avoid artifactual variations in the signal due to receive and transmit field inhomogeneities. Tissue signals were determined by measuring the mean intensity of these ROIs. An ROI was also drawn in the background for measurement of noise. The signal difference between two tissues was divided by the standard deviation of the noise to obtain CNR for that pair of tissues. This is analogous to CNR defined earlier in Equation 2.28 for simulated signal. As the two scans differed in the total imaging time,

CNR was normalized by dividing with the square-root of imaging time to make the comparison between the two scans meaningful. The normalized CNR is referred to as the CNR efficiency.

2.4.1.2 Creation of the ratio image

Initial post-processing involved calculating the ratio image by dividing the optimized MPRAGE image with the FLASH image. The images for the study consisted of two MPRAGE images and two FLASH images in each subject. To account for any motion between the scans, the images were co-registered before further calculations. The first MPRAGE was used as a reference to which the other T_1-weighted image and the two FLASH images of the same subject were rigidly registered using a linear, affine registration in Amira (Visage Imaging). Lanczos resampling was used to apply the transformations needed to complete the registration. The two registered FLASH images were added together. As the radio-frequency field inhomogeneities are known to be smoothly varying (Sled *et al.*, 1998; Belaroussi *et al.*, 2006) the sum of FLASH images was smoothed using a 3D median filter of kernel size 3 to eliminate any high-frequency variations in the intensity. As Amira does not allow an increase in size of the median filter kernel beyond 3, the process was repeated twice to obtain the desired smoothing. The sum of the two co-registered T_1-weighted images was divided by the filtered, average FLASH image to obtain the ratio image with significantly reduced B_1^+ and B_1^- inhomogeneities. This ratio image was used for all the further processing to obtain morphological measurements.

2.4.2 Results and discussions

Table 2.6 summarizes the results of contrast measurements in the two MPRAGE images. These measurements were obtained by measuring the mean signal intensity in multiple ROIs in several slices in each tissue.

Tissues	CNR in a.u.		CNR efficiency	
	Long (optimized) TD	Short TD	Long (optimized) TD	Short TD
WM-GM (anatomical contrast)	26	18	6.6	5.6
GM-GMm (intracortical contrast)	12	9	3.1	2.8
GMm-WM	14	9	3.5	2.8

Table 2.6: CNR data for optimized and short-TD MPRAGE images. CNR efficiency is calculated by dividing CNR with the square-root of acquisition time (N =1).

Figure 2.17 shows a representative slice for qualitative comparison from each of the optimized and short-TD MPRAGE scans, in approximately the same position. It is a medial, sagittal slice cutting through the primary motor cortex, and is an example of the slice used in signal measurements. The slice in the left panel was taken from the image acquired with optimized MPRAGE while that on the right is from short TD-MPRAGE image. Myelinated gray matter in M1 is brighter in both images compared to unmyelinated gray matter.

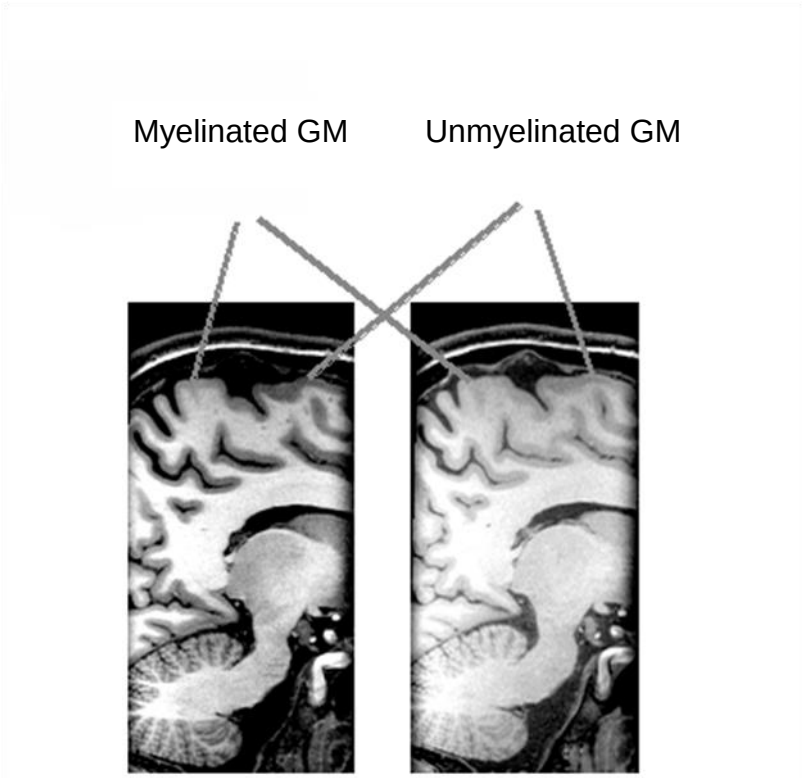

Figure 2.17: Qualitative comparison of the optimized and short TD MPRAGE images. A slice in a similar location is shown from both scans. Both slices are normalized to the intensity value in WM in the corpus callosum in the long TD scan. The slices are also being displayed at the same window and intensity level.

The MPRAGE image made with a long TD, shown in the left panel of Figure 2.17, has greater overall contrast. More importantly, there is more intracortical contrast in this image making the myelinated gray matter more distinguishable from the unmyelinated gray matter in this image.

Figure 2.18 shows a representative slice from the ratio image.

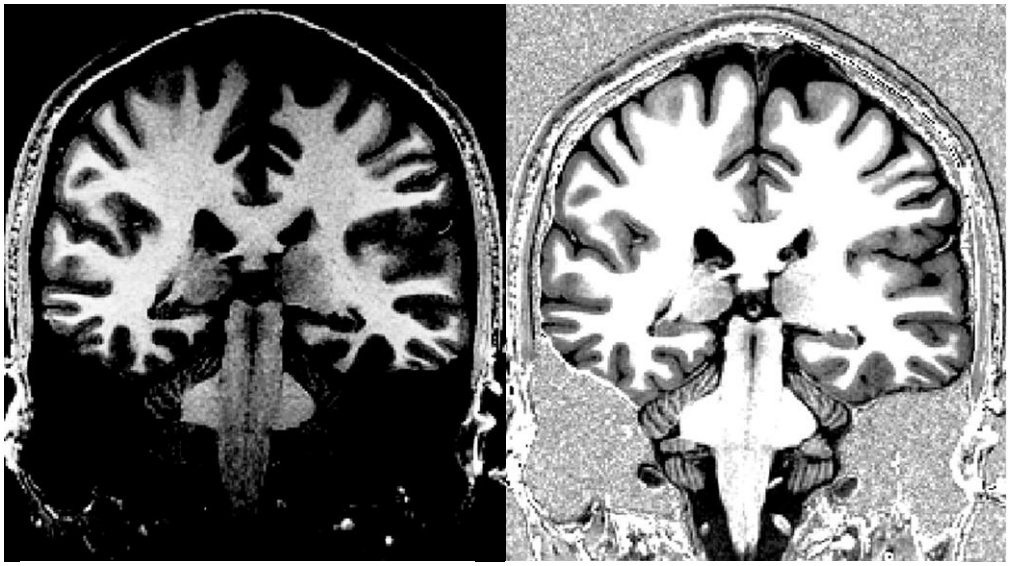

Optimized MPRAGE Ratio

Figure 2.18: Coronal slices from optimized MPRAGE (left) and ratio (right) images. The slices have been normalized to the same maximum intensity and are being displayed at the same window and level. A very high contrast level has been chosen to emphasize the variations in GM intensity.

For comparison, the same slice from the optimized MPRAGE image is also shown in Figure 2.18. Both images have been normalized to the same maximum intensity and they are being shown with the same window and level. The MPRAGE image has artifactual intensity variations, presumably due to radio-frequency field inhomogeneities, superimposed on the actual tissue-related intensity variations. The variation is more prominent along the SI axis, making the cortex in the most superior location almost invisible. This variation is almost absent in the ratio image. The ratio image also has greater intracortical and overall anatomical contrast.

To summarize, there is an increase in CNR and CNR efficiency for all three tissue pairs, GM and WM, GM and GMm and WM and GMm, in the images obtained with optimized MPRAGE. Thus, there is an increase in the overall anatomical contrast between WM and GM. There is also greater contrast within the cortex, between myelinated and typical GM. With an increase in the contrast between GMm (in the deeper layers in the cortex) and the underlying WM, it is easier to distinguish between the cortex and the underlying WM. Therefore, the optimized scan offers better definition of the three tissues which is important for image post-processing. Furthermore, dividing the optimized MPRAGE images with predominantly proton density-weighted images eliminates the B_1^- inhomogeneities and significantly reduces the B_1^+ inhomogeneities.

To conclude, the best way to increase the intracortical contrast in MPRAGE images for a given resolution and imaging time is to increase the time delay (TD) between the end of an acquisition block and the next inversion pulse. It was determined that for 0.7 mm isotropic resolution and imaging time of 15 min, the following MPRAGE parameters produce the best intracortical contrast with the least blurring: TD = 1100 ms, TI = 1000 ms and FA = 12º. These optimized MPRAGE images have enhanced intracortical contrast necessary for visualizing the boundary between M1 and rest of the cortex on the basis of myelination. Lastly, it is concluded that dividing the optimized MPRAGE image by a FLASH image, acquired with FA = 4º over the same FOV and with the same receive RF profile, significantly removes the artifactual intensity variations, presumably due

to RF field inhomogeneities, from the images. Therefore, the imaging protocol for the morphological study of M1 in humans consisted of making two MPRAGE images with optimized parameters and two FLASH images in each subject. The ratio image thus calculated was used for all future post-processing to delineate the heavily myelinated motor cortex.

3 Image processing protocols for visualization of intracortical myelin in the precentral gyrus based on the proportional myelinated thickness

3.1 Introduction

The goal of medical image processing is to extract useful information from images accurately, which could be either buried in image artifacts or simply not available directly from the images. Image processing therefore complements imaging. The selection of image processing protocols depends on several factors such as the specific goal of the imaging, imaging modality, image contrast and the imaged object. For anatomical MRI studies of the brain, a general sketch of processing protocols would include most of the following steps: removing non-brain tissues, image segmentation into various tissues/structures, surface or volume rendering for visualization and quantitative measurements in regions-of-interest.

The goal of the work described in this chapter was to measure the surface area of the well-myelinated region of the precentral motor cortex *in vivo* in humans, based on myeloarchitectonic features, using T_1-weighted MRI with optimized intracortical contrast. Measurement of the surface area of the well-myelinated region of the precentral motor cortex involved processing the MR images to visualize variation in intracortical myelin in the precentral gyrus so that the boundaries of the well-myelinated region within the precentral gyrus could be demarcated to measure its surface area based on its myeloarchitectonic features.

In this chapter, a detailed description of image processing for visualizing the variation of intracortical myelin in the precentral gyrus is given. The myeloarchitectonic feature that was used for delineating the primary motor areas in the precentral gyrus was the thickness of myelinated gray matter in the cortex relative to total cortical thickness. Deeper cortical layers are well-myelinated almost everywhere in the cortex (Nieuwenhuys, 2013). In the primary functional areas, the myelinated gray matter is relatively dense compared to the density of fibers in the intervening cortex (Braak, 1980; Braitenberg, 1962). Also, heavy myelination generally persists through most of the cortical thickness in the primary functional areas (Braitenberg, 1962; Braak, 1980; Vogt and Vogt, 1909). Therefore, the relative thickness of myelinated gray matter in the cortex can serve as a metric to demarcate the heavily myelinated motor region from the adjacent cortex. The thickness of deeper, well-myelinated cortex relative to total cortical thickness is referred to as the proportional myelinated thickness (p). This was calculated by dividing the thickness of well myelinated gray matter in the cortex with the total cortical thickness and involved measuring cortical thickness as well as the thickness of the myelinated gray matter in the cortex. Thickness in the cortex is defined as the distance between an outer and an inner surface. Therefore, measuring the myelinated thickness involved defining the outer and inner boundaries of the well-myelinated tissue in the cortex. The well-myelinated tissue in the cortex is located in the inner most layers in the cortex, its inner boundary is the boundary between the cortex and the underlying WM. To

determine the outer boundary however, the cortex required segmentation into well-myelinated and unmyelinated tissue. Thus, brain tissue was segmented into four tissue classes: cortical gray matter (GM), myelinated gray matter in the cortex (GMm), white matter (WM) and cerebrospinal fluid (CSF). This is a novel approach as most neuroimaging studies including studies of intracortical myelin segment brain into GM, WM and CSF only (Dahnke *et al.*, 2013; Glasser and Van Essen, 2011; Hutton *et al.*, 2008; Li *et al.*, 2012; Lusebrink *et al.*, 2013).

Image processing protocols in this study consisted of the following three major steps.

1. Segmenting brain tissue into GM, GMm, WM and CSF
2. Generating boundaries between adjacent tissues representing the cortical surfaces
3. Obtaining thickness measurements

These processing steps were performed on the ratio image determined by dividing the T_1-weighted image with the pre-dominantly proton density-weighted image. Prior to these processing steps, some pre- processing steps were performed to remove extraneous tissues. Some of the preliminary processing steps were performed using FreeSurfer's automated pipeline (https://surfer.nmr.mgh.harvard.edu/), while some others requiring manual intervention were performed in Amira (Visage Imaging Inc.). Tissue segmentation was performed using a clustering technique and a level set method was used to obtain the thickness measurements. These processing steps were performed

using CBS brain processing tools (http://www.nitrc.org/projects/cbs-tools/) in MIPAV (http://mipav.cit.nih.gov/). This selection was based on a number of reasons as follows. CBS tools can be used with sub-mm resolution data contrary to other software such as FreeSurfer, which are designed for 1 mm isotropic resolution. The CBS tools allow thickness measurements between any two surfaces previously obtained or modified with any other program. In contrast, FreeSurfer only calculates the thickness between the pial and WM surfaces obtained through its own pipeline. Along with providing a pre-assembled pipeline for processing the brain images starting from the pre-processing step to a given endpoint, say cortical thickness measurements, the CBS tools also provide stand-alone plugins for individual processing steps. Thus, users of CBS tools can easily construct their own image processing pipeline based on the goals of their study. Surface generation and visualization was performed using Amira. Figure 3.1 is a flow chart that briefly describes the image processing pipeline and software used for each step.

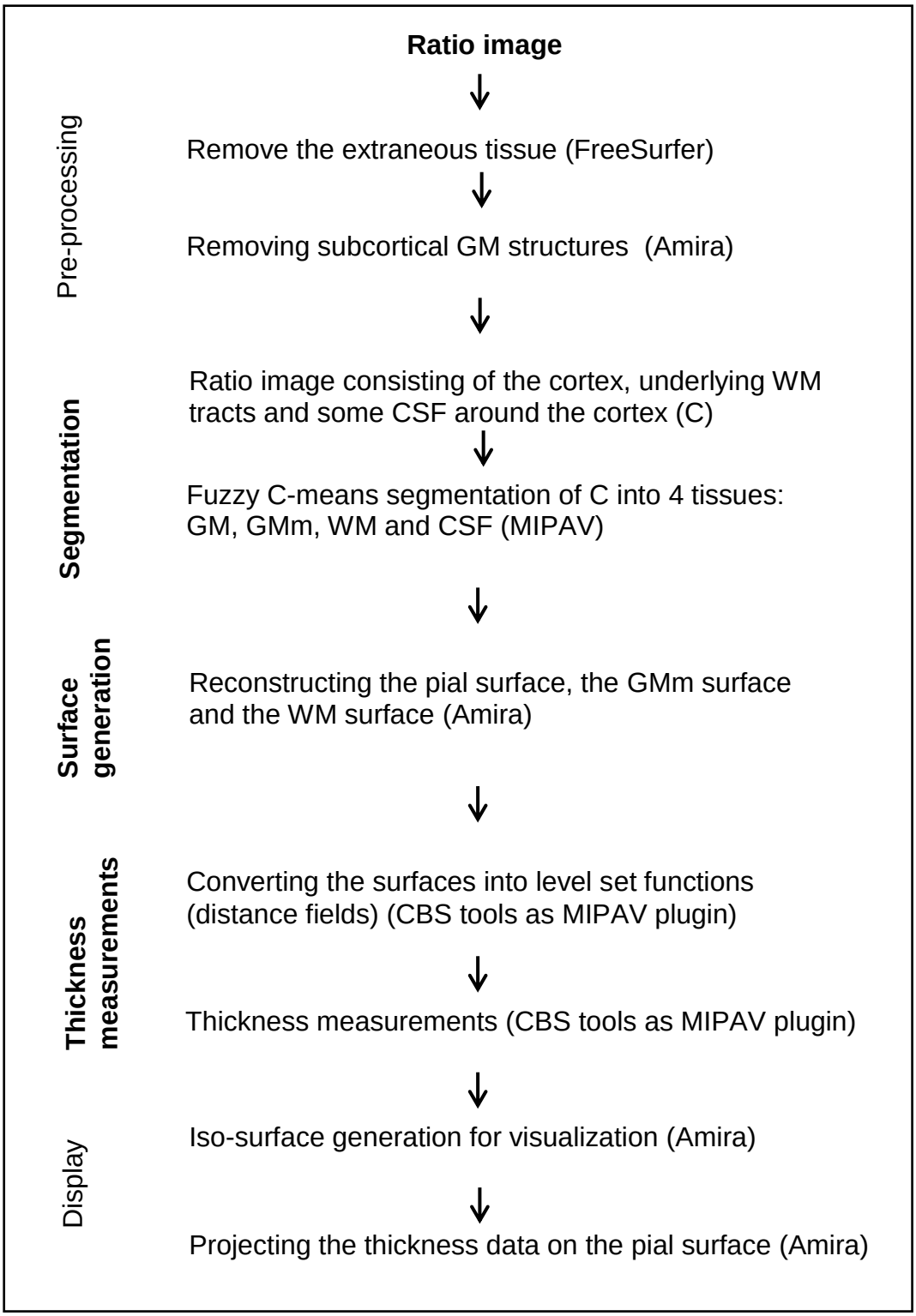

Figure 3.1: Flow chart describing major steps in the image processing protocols

3.2 Pre-processing of the ratio image

Pre-processing prepares images for segmentation. These steps were performed in the following order.

1. Removing the skull and extraneous tissue from the ratio image

FreeSurfer (http://surfer.nmr.mgh.harvard.edu/) (Fischl, 2002) was used to extract a rough brain mask by removing the skull and extraneous tissue from the ratio image. As FreeSurfer only takes images with 1 mm isotropic resolution, the 0.7 mm isotropic ratio image was resampled to a 1 mm isotropic grid using Amira. FreeSurfer's output consists of two surfaces representing the pial surface for each hemisphere. These surfaces were labeled as the outer boundary for each hemisphere and were resampled back to 0.7 mm isotropic resolution using Amira. The hemispherical labels were then multiplied with the ratio image in Amira, to remove dura mater, cerebellum and extraneous tissues thus producing masked hemispherical images.

2. Refining the masked images

The boundary between cortex and CSF in the masked ratio image obtained from FreeSurfer does not visibly follow the outer boundary of the cortex. This can happen from resampling of the FreeSurfer output to 0.7 mm isotropic resolution. Therefore, the mask was grown to include a few voxels of CSF everywhere along the cortical boundary. At this point, the masked hemispherical ratio image now consisted of some CSF around the cortex, the cortex itself, WM tracts underlying the cortex and subcortical GM structures such as basal ganglia

and thalamus. The sub-cortical GM structures were removed because they are not included in the segmentation scheme in this study. Thus for the last pre-processing step, the basal ganglia and thalamus were manually removed from the masked ratio image. Each masked hemisphere was then visually inspected, slice by slice, for any remaining dura mater and also for missing brain tissue. Remaining dura mater was manually removed and missing brain tissue was manually labelled in Amira. Finally, the two hemispheres were recombined in Amira to make a single whole brain mask ready for segmentation. The recombining was performed to ensure that the segmentation output would not affected by any interhemispheric differences.

At the end of pre-processing, the ratio image consisted only of cortex, underlying WM tracts and some CSF surrounding the cortex. Figure 3.2 shows a representative slice from a masked ratio image.

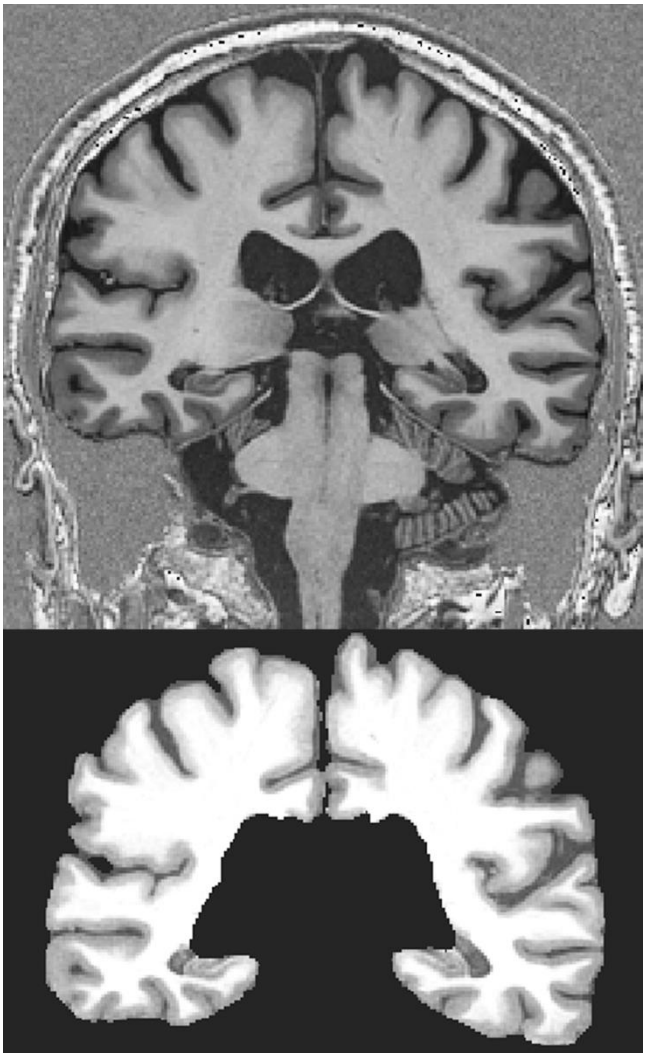

Figure 3.2: The top panel shows a coronal slice of a representative ratio image. The bottom panel is the same slice from masked version of the ratio image.

3.3 Segmenting the brain tissue into GM, GMm, WM and CSF

Image segmentation is the process of dividing an image into sets of pixels or voxels that represent various distinct objects or features (such as the brain and the skull) in the image. Image segmentation methods can either be fully data driven using no other information or they can use a priori information in the form of atlases or look up tables (LUT), along with the image data. Commonly used

segmentation techniques include thresholding, region growing, clustering, edge detection and atlas-based segmentation.

The choice of a particular method for segmentation depends on several factors including the imaged object and information that is needed from the image. The fuzzy C-means clustering algorithm as implemented in MIPAV (http://mipav.cit.nih.gov/) was used in this study. The algorithm is completely data-driven and is easy to implement. Furthermore, MIPAV's implementation of fuzzy C-means allows the user to segment the brain into any number of tissues.

Fuzzy C-means is a clustering-based segmentation algorithm (Bezdek, 1984; Dunn, 1973). In imaging, cluster analysis involves dividing the pixels or voxels in the image into a number of subsets (clusters), each centered on a central value called the centroid. Assigning a specific pixel or voxel to a cluster is based on minimizing of similarity measure, for example the Euclidean distance between the pixel's value and the centroid. The centroids are selected so that there is maximum similarity between pixel values in the same cluster and maximum contrast between pixel values from different clusters. The clusters are usually disjoint and reproduce the original image when recombined. In imaging, there are always some pixels or voxels that lie on the boundary between multiple tissues and therefore contain more than one tissue type. This is referred to as partial voluming of the tissues. Fuzzy C-means takes into account the partial volume effects. Thus, it is an extension of the k-means or hard C-means algorithms which considers all pixels or voxels to be filled by one tissue only. The

fuzzy C-means allows one pixel or voxel to belong to multiple clusters simultaneously.

The implementation of fuzzy C-means involves defining a membership function for each pixel value in the image based on the similarity that the pixel value has with each cluster (Bezdek, 1984). Therefore, each pixel value has a membership in every cluster; a membership value close to unity means very strong resemblance with that cluster and a membership value close to zero means very weak resemblance. The sum of all the membership functions for a given pixel is 1.

In MIPAV's implementation of the fuzzy C-means algorithm for image segmentation, image intensity is taken as the similarity measure. Thus, the centroids are also chosen based on the image intensity values. The algorithm is independent of any voxel's spatial position in the image. I summarize MIPAV's implementation of the algorithm in the following paragraphs which is based on Pham and Prince's work (Pham *et al.*, 2000; Pham and Prince, 1999). Consider an image with N pixels or voxels:

$$Intensity\ of\ the\ pixel\ /\ voxel\ \ in\ ith\ position\ \stackrel{\text{def}}{=}\ x_i\ with\ i = 1{:}\,N,$$

$$C > 2\ is\ the\ number\ of\ clusters,$$

$$f_z\ is\ a\ constant\ that\ defines\ fuzziness,$$

$$\mu_{ij}\ \stackrel{\text{def}}{=}\ membership\ function\ for\ x_i\ \in\ \ cluster\ with\ centroid\ c_j \qquad 3.1$$

The algorithm starts with a pre-defined C. It selects the initial centroids by equally dividing the intensity range between the minimum to maximum intensity into the desired number of classes. Initially, random membership values are assigned to pixels or voxels. The algorithm proceeds by iteratively updating the membership values and cluster centroids. The following objective function is minimized during iterations.

$$E = \sum_{j=1}^{C} \sum_{i=1}^{N} \mu_{ij}^{f_z} \left\| x_i - c_j \right\|^2 \quad 3.2$$

The minimization is achieved through two computations. First, the membership function for a given pixel or voxel is updated using the current centroids, as given below.

$$\mu_{ij} = \frac{\left\| x_i - c_j \right\|^{\frac{-2}{f_z - 1}}}{\sum_{j=1}^{C} \left\| x_i - c_j \right\|^{\frac{-2}{f_z - 1}}} \quad 3.3$$

Then, the centroids are updated using the current membership function, as follows.

$$c_j = \sum_{i=1}^{N} \frac{\mu_{ij}^{f_z} \cdot x_i}{\mu_{ij}^{f_z}} \quad 3.4$$

The iterations continue until the user-specified maximum number of iterations occurs or when convergence is achieved. Convergence occurs when all membership functions over all pixel locations *i* change by less than the tolerance value between two iterations. As the centroids are iteratively updated, the final

centroids reflect the tissue classes that they represent, irrespective of their initial values.

Figure 3.3 below is a screen shot of the dialogue box for the user to start fuzzy C-means segmentation in MIPAV. The desired exponent value refers to the fuzziness function or variable f_z in the above equations. Signal threshold specifies the minimum intensity value in the image. Background cropping when checked, finds the smallest bounding box in the image outside of which all intensities are below the threshold.

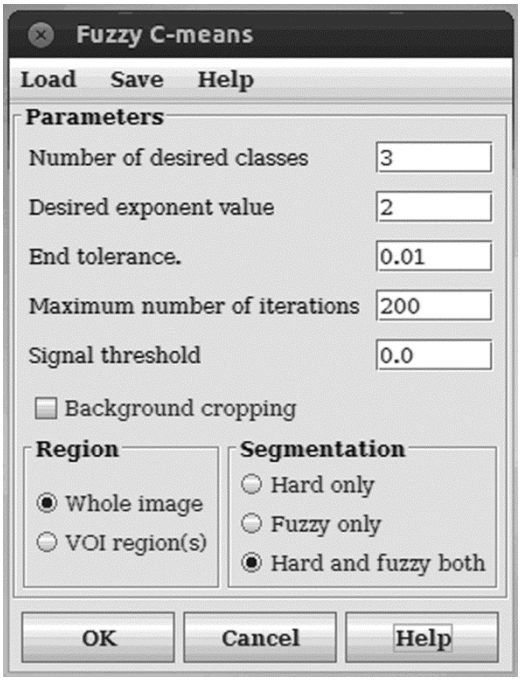

Figure 3.3: User defined parameters for fuzzy C-means segmentation.

Using MIPAV's implementation of fuzzy C-means, the masked ratio image was segmented into GM, GMm, WM and CSF by selecting the following values for the parameters: number of desired classes = 4, desired exponent value = 2

(default), end tolerance = 0.01 (default), maximum number of iterations = 200 (default), signal threshold = 1, background cropping = checked, segmentation output = hard and fuzzy both. The segmentation output consisted of membership function for each tissue as well as a gray-level image containing four levels corresponding to the hard segmentation output for the four tissues. The gray level image is shown in Figure 3.4.

After segmentation, the hemispheres were split again so that the medial wall in each hemisphere could be visualized without obstruction. The processing steps described in the next sub-sections were performed on each hemisphere separately.

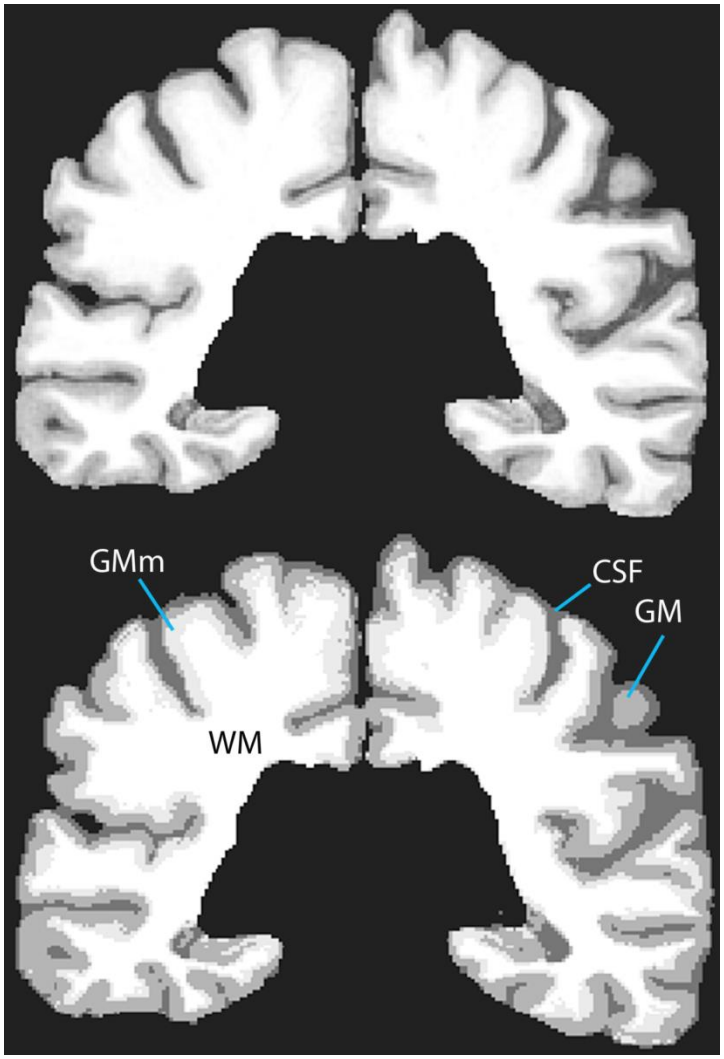

Figure 3.4: The top panel shows a slice from the masked ratio image. The bottom panel shows fuzzy C-means hard output with four tissues showing as various levels of gray.

3.4 Generating the boundaries between adjacent tissues representing the cortical surfaces

Cortical surface reconstruction means generating a geometrically accurate representation of any surface in the cortex or bounding the cortex. The correct geometrical representation is consistent with the true geometry of the cortex

including the gyral folds and narrow sulci. In digital image processing, the term surface often refers to a polygonal mesh used for visualizing the outer edge of an image or structure and obtained using surface rendering techniques applied to the edge voxels (Dale *et al.*, 1999). Thus, in general vertices of a surface are not the image voxels. In this thesis, the term “surface” represents the boundary of a structure or tissue in the image. The outer most voxels of a structure or tissue in the image define its boundary. To avoid confusion, the term “iso-surface” is used to represent the polygonal mesh generated for visualization of a surface or boundary using surface-rendering techniques.

In the first step in boundary reconstruction, binary masks (labels) representing the three tissues, GM, GMm and WM, were defined using the fuzzy C-means hard segmentation output. The GM mask is a binary image where GM, GMm and WM are represented as 1 and CSF is included in the background which is at 0. The outer boundary of the GM mask defines the boundary between CSF and the cortex and thus represents the pial surface. The GMm mask is a binary image where GMm and WM are represented as 1 and GM and CSF are included in the background which is at 0. The outer boundary of the GMm mask defines the boundary between GM and GMm and represents the GMm surface. Similarly, the WM mask is a binary image where WM is represented as 1 and GMm, GM and CSF are included in the background which is at 0. The outer WM boundary of the WM mask defines the boundary between GMm and underlying WM and represents the WM surface. Masks were further refined by removing

small groups of voxels unconnected from the main body of the mask. This was accomplished using the 3D remove-islands built-in tool in Amira. This completes the reconstruction of the GM and GMm boundaries. However, the WM boundary reconstruction required one further step.

In the gyral crowns, most of the voxels adjacent to WM voxels are filled with GMm. As a result, these WM voxels have intensities lower than true WM intensity due to partial voluming of GMm caused by insufficient resolution. Thus, the hard segmentation process commonly assigns these WM voxels to GMm. Therefore, to account for these thin WM tracts, the WM surface was modified using the fuzzy WM membership function level of 0.1. This essentially means that a voxel with a 10% or higher probability of belonging to the WM is included in WM. The 0.1 membership level was empirically selected by manual inspection and subsequently used consistently across all images. At this level the cortical thickness in the precentral gyrus agrees closely with the histological measurement of 4.5 mm (Zilles, 2004). A level higher than this results in underestimated thickness values in the precentral gyrus.

The output of this processing step was the three nested surfaces which represent the outer (the pial surface) and inner (the WM surface) boundaries of the cortex and the outer boundary of cortical GMm in each hemisphere. Figure 3.5 shows the three boundaries from a representative brain.

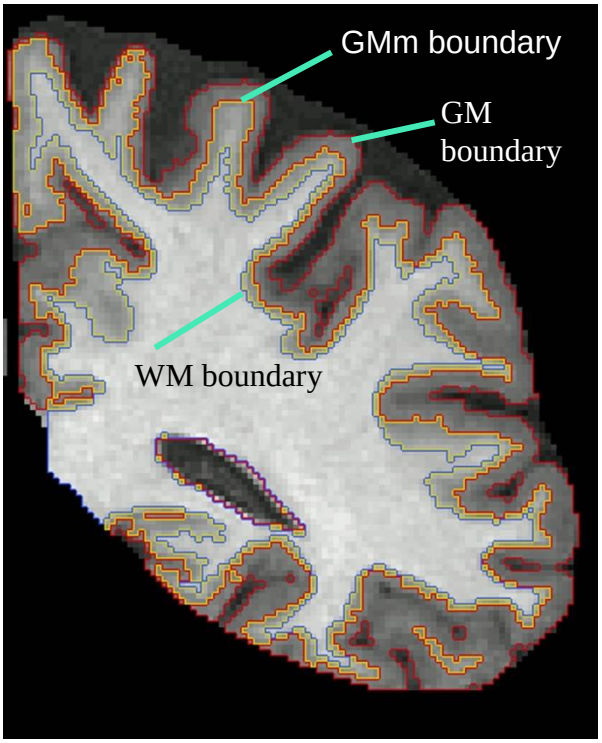

Figure 3.5: The three surfaces (boundaries) in a representative slice in the right hemisphere only.

3.5 Obtaining the thickness measurements

Cortical thickness is the distance between the GM/CSF boundary (the outer cortical surface) and the GM/WM boundary (the inner cortical surface). Measuring cortical thickness from digital images involves defining a geometric measure for this distance and then numerically implementing the defined measurement. Defining cortical thickness is challenging for the following reasons. The cortex is a 3D, highly convoluted, thin sheet of tissue with variable thickness. Furthermore, the variations in thickness are twofold. Certain cortical regions are known to be thicker than others, for example the anterior bank of the central

sulcus is much thicker than its posterior bank (Brodmann, 1909; Zilles, 2004). Also, the gyral crowns are known to be thicker than the sulcal depths within regions (Sereno *et al.*, 2013; Waehnert *et al.*, 2013). Consequently, correct thickness measurements require that the line of measurement should be orthogonal to the cortex and measurement should be performed at every vertex on either boundary. Due to the lack of a standard mathematical definition of thickness between two 3D curved surfaces, there are various definitions of cortical thickness adopted by different researchers. The most frequently used definitions are the following.

- T_{near}: the distance from a vertex on the outer surface to the nearest vertex on the inner surface (MacDonald *et al.*, 2000).
- $T_{link:}$ the distance between corresponding points on the two surfaces (la Fougere *et al.*, 2011; MacDonald *et al.*, 2000).
- T_{norm}: the orthogonal distance between the two surfaces.

Because the two surfaces are curved, orthogonal distance can be defined in various ways (e.g. distance along the normal to the surfaces (Fischl *et al.*, 2002; MacDonald *et al.*, 2000) or distance from a vertex on one surface to the closest triangular face on the other surface along the face normal (Osechinskiy and Kruggel, 2012). Surface normal is the average of normals defined on several adjacent faces. FreeSurfer defines cortical thickness as the average of two-way orthogonal distances, shown as d1 and d2 in Figure 3.6, between linked vertices P and P’ on the two surfaces.

Figure 3.6 illustrates some of these 3D scenarios using a 2D cartoon.

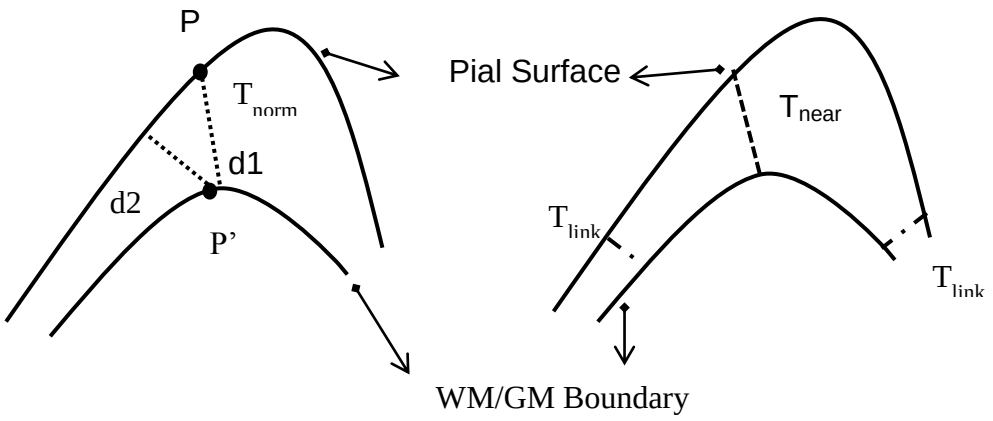

Figure 3.6: A schematic diagram in 2D showing various ways to define thickness of the 3D cortical ribbon.

For thickness to be an anatomically meaningful quantity, all thickness definitions must meet two criteria: there should be 1-1 mapping between points on the two surfaces, and thickness should be the same whether measured at the outer surface or at the inner surface. T_{near} does not satisfy any of these while the other two definitions, T_{link} meets both of these requirements in general, but it runs into problems if one surface is displaced with respect to the other: for example when the line of measurement is not orthogonal to one of the surfaces. T_{norm} is the most robust thickness definition and is widely accepted by neuroscientists (Li *et al.*, 2012). T_{norm} was used for cortical thickness measurements in this thesis.

There are several ways to numerically implement T_{norm}. One approach is to find the orthogonal distance by explicitly determining the two surfaces representing the two boundaries by means of parametric (Dale *et al.*, 1999; Xu *et al.*, 1999) or geometric deformable models (Han *et al.*, 2001) and then calculating the Euclidean distances between vertices. Another approach is to use some geometric property of the two surfaces as a measure of the orthogonal distance. For example, for surfaces in a Laplacian framework (Jones *et al.*, 2000) the gradient of the Laplacian function is by definition normal to either of the iso-potential surfaces and hence represents a measure of the orthogonal distance. Another way to numerically implement the orthogonal distance is by using the level set approach. The level set function numerically describes the evolution of curves or boundaries along normals (Sethian, 1996). Therefore, the level set function is inherently orthogonal to the boundary. To determine the thickness of tissue between two boundaries, one can imagine expanding the inner boundary towards the outer or contracting the outer boundary towards the inner and finding the amount of displacement. However, displacing a boundary is the same as curve evolution (contraction or expansion) and it can be modelled using a level set function. In the level set method (LSM) for cortical thickness measurements, the level set functions represent the various boundaries and their expansion and contraction (Han *et al.*, 2003). Defining a level set function thus requires only specifying the boundary between the object volume and the background and does not require explicit calculation of the surface. Therefore, implementing LSM

for cortical thickness measurements is easy as it works with a set of two binary volumes. Also, because the level set function exists everywhere in the image volume, the calculated thickness is also a volume. This allows the user to treat the calculated thickness volume as any other image and directly perform arithmetic operations, which are often needed during image processing, on the thickness volume. Also, most other software usually define and calculate the thickness on the pial surface only. However, the LSM generates a cortical thickness volume and one can intercept this volume by any anatomically meaningful surface to obtain the thickness measurements at that surface. Thus, the LSM for thickness calculations is beneficial in obtaining surface displays and was used for thickness measurements in this thesis, as it is an easy to implement technique for the most robust definition of cortical thickness based on orthogonal distance.

In the following sub-sections, the theory and general implementation details of LSM are described, followed by a description of cortical thickness calculations with LSM using CBS tools in MIPAV.

3.5.1 The level set method for cortical thickness measurements

The level set method is a numerical technique to describe curves that evolve with time and occupy new spatial positions as determined by relevant forces. The method works by defining an auxiliary function, called the level set function, for the evolving curve or boundary. The function evolves in space and time and its configuration at any space-time point represents a configuration of

the curve at that point. The initial curve represents the zero level set of the level set function.

LSM is frequently used for cortical surface reconstruction and cortical thickness studies (Dahnke *et al.*, 2013; Liu *et al.*, 2008; Osechinskiy and Kruggel, 2012). Cortical thickness measurements by LSM involve defining level set functions for the two cortical surfaces. Each level set function describes expansion of the surface in the space outside the boundary and contraction in the space enclosed by the boundary. Thus, in the space between the two surfaces, the level set functions describe evolution of one surface towards the other. Therefore, subtracting the two level set functions yields the distance between the two surfaces.

To obtain the thickness of GMm in the cortex and the cortical thickness, calculations were performed on level set functions representing the three boundaries: the outer boundary of GM, the outer boundary of GMm and the outer boundary of WM. The appropriate level set functions were subsequently subtracted to accomplish the two thickness measurements. Below, a description of the theory behind, and implementation of LSM is detailed before describing thickness measurements performed with LSM in MIPAV.

3.5.1.1 Formal definition and implementation of LSM for tracking moving interfaces

In order to track a moving boundary numerically, one should first represent the boundary as an analytical function. Then, one can apply the laws of conservation and information about forces governing motion of the boundary to derive an equation of motion to determine the future configurations of the boundary. It is nearly impossible to arrive at an exact analytical representation for the boundaries that one encounters in the real world as these boundaries often have complex, variable and unknown shapes. The level set method circumvents this problem by using an auxiliary function $\varphi\ (x)$, referred to as the level set function, to track the spatial configuration of a moving interface. Thus, one can select any appropriate, well-defined function that is easy to work with, as the level set function and use the velocity information and conservation laws governing the motion of the boundary to track its future configurations. Although there are numerous choices for the level set function, the signed distance function is preferred widely for this purpose, for its stability in numerical computations (Han *et al.*, 2003).

Below, the theory of LSM is summarized with the help of the following works: Han *et al*., Osher *et al*. and Sethian (Han *et al.*, 2003; Osher and Paragios, 2003; Sethian, 1996).

By definition, the level set function changes sign at the boundary. It is therefore zero at the boundary. Given an evolving interface $\Gamma\ (x, t)$ in real

space, bounding a region Ω, a smooth level set function $\Phi\ (x),\ x \in R$ can be associated with $\Gamma(x,t)$ that follows the motion of Γ in time.

$$\Phi\ (x) < 0 \quad for\ x\ \in\ \Omega \qquad (\text{inside region } \Omega^{-})$$

$$\Phi\ (x) > 0 \quad for\ x \notin\ \Omega \qquad (\text{outside region } \Omega^{+})$$

$$\Phi\ (x(t), t = 0) =\ 0 \quad for\ x\ \in\ \partial\Omega = \Gamma(t)\ (\text{the interface}) \tag{3.5}$$

The signed distance function d gives the distance of a point from the boundary with the typical convention that $d < 0$ for points inside the region and $d > 0$ for points outside the region. Therefore, for all points $\in R^n$, the signed distance function defines the level set function as follows.

$$\Phi\ (x) = -d(x) \quad for\ x\ \in\ \Omega^{-}$$

$$\Phi\ (x) =\ 0 \qquad for\ x\ \in\ \partial\Omega$$

$$\Phi\ (x) = +\ d(x)\ for\ x\ \in\ \Omega^{+} \tag{3.6}$$

And the signed distance is defined as follows.

$$d\ (x) =\ \min_{x_c\ \in\ \partial\Omega} |x - x_c| \tag{3.7}$$

The signed distance function has useful properties that make the computation of level sets easier. The most important property is that its gradient is a unit vector, normal to the level set function. Calculation of the two important geometric properties of the interface, the unit normal and the curvature thus become simpler.

$$unit\ normal\ to\ \Phi = n = \frac{\nabla\Phi}{|\nabla\Phi|} = \nabla\Phi$$

$$Curvature\ of\ \Phi = \kappa = \nabla.\mathrm{n} = \nabla.\nabla\Phi = \text{Laplacian}\ \Phi \qquad 3.8$$

Having defined the appropriate level set function, the next objective is to use it to determine the new position of interface at all later times. As the level set function is defined in a way that it vanishes at the boundary, the future configuration of the boundary Γ can be identified as the one for which Φ vanishes. Therefore, moving the interface is equivalent to updating Φ.

One can update Φ by using the initial Φ, which is completely defined ($\Phi\ (x(t), t = 0) = 0$) and using the information about velocity of the boundary. Suppose $x(t)$ is a particle trajectory on the interface $\Gamma(t)$, moving with velocity $v = \dot{x}\ (t)$. The velocity may depend on factors such as the local curvature, expansion and contraction speeds and the overall advancement speed. By definition, $\Phi\ (x\ (t), t = 0) = 0$. Differentiating with respect to time (t), one obtains the following equation.

$$\dot{\Phi} + v.\ \nabla\Phi = 0 \qquad 3.9$$

As the gradient of Φ is by definition normal to Φ, one only needs the normal component of velocity in order to update Φ.

$$\dot{\Phi} + v_n\ |\nabla\Phi| = 0 \qquad 3.10$$

This is the fundamental level-set equation.

The fundamental level-set equation, Equation 3.10, is a first order partial derivative equation that relates the spatial and time derivatives of a quantity under some conservation principle. Such equations, referred to as Hamilton-Jacobi equations, frequently appear in classical mechanics and therefore, their solutions are well established. The important point to notice is that the information about the spatial derivatives of the boundary is not available because the boundary cannot be defined using an analytical function. However, one can obtain this information for the auxiliary function Φ which is completely defined.

The LSM algorithm initiates by assigning random distance values to all the grid points and defining a force field and velocity v_n of a point on the boundary. The algorithm then proceeds by calculating the new distance value for each grid point after a discrete time interval Δt by calculating the distance travelled by the boundary at the rate v_n in time Δt. The algorithm calculates finite differences to approximate the derivatives in the level set equation under the condition that the velocity does not change sign. This is referred to as the upwind numerical method of calculating spatial derivative (Han *et al.*, 2003; Zhao, 2005). Denoting a grid point by x_i and the discrete time scale as t_m, the resulting equation to update the level set function after each time step Δt thus becomes the following.

$$\Phi\,(x_i, t_{m+1}) = \Phi\,(x_i, t_m) + \Delta t\, \Delta\Phi\,(x_i, t_m) \qquad 3.11$$

Therefore, for finding the future configuration of interface, one can iteratively update the above equation for each grid point until convergence or for a user-defined number of time steps.

Most LSM implementation schemes use the following two simplifications for the sake of speed and to meet other computational requirements.

- Instead of updating the level set function everywhere, the process is limited to a narrow band in the vicinity of the evolving interface. This is referred to as the narrow band approach (Osher and Paragios, 2003).
- In situations where the velocity field does not change sign and the interface marches forward only or backward only and it never crosses a given grid point twice, the level set function is re-initialized after each calculation. This is referred to as the fast marching method (FMM) (Zhao, 2005). The upwind schemes employ FMM. The fast marching method is helpful in situations where the speed is not constant and therefore, the level set function starts deviating from the distance function as one moves away from the initial interface. A re-initialization means that the new level set now becomes the zero-level set and one can implement it as a new distance function with easy to calculate geometric properties.

3.5.2 LSM for cortical thickness calculations using CBS tools in MIPAV

For cortical thickness calculations, LSM takes the two cortical surfaces as the zero level values of their respective level set functions and considers evolution of the level set function under relevant forces to determine what one

boundary will look like when displaced towards the other boundary. Thus, in LSM, thickness at any point on the grid is simply the sum of two level set functions.

$$Thickness\ (x) = \ \Phi outer\ (x)\ + \Phi inner\ (x) \qquad 3.12$$

Notice that in the region between the two surfaces, the outer level-set function describes contraction of the outer surface while the inner level-set function describes the expansion of the inner surface. Thus, they have opposite signs. As a result, one should subtract the two functions to get the correct thickness measure.

$$Thickness\ (x) = \ \Phi outer\ (x) - \Phi inner\ (x) \qquad 3.13$$

This definition of thickness results in the same thickness measurement on all the points on either boundary or between the two surfaces. Also, notice that as the distance fields are calculated in the entire volume, the thickness data is also a volume. One can intercept the volume by any surface, and find the thickness values on the surface nodes by interpolation.

Thickness calculations with the CBS tools consists of two major steps: representing each surface as the zero level set of a level set function using distance fields and adding the two level-set functions to obtain the thickness measurements throughout the image volume. The details of these two steps are explained in the next sub-sections.

3.5.2.1 Distance fields for the two boundaries

The signed distance function defines the level set function for each surface. I calculate the distance field using the module “Distance Field v1.53R” available as JIST plugin for MIPAV (version 7.0.1, http://mipav.cit.nih.gov/). For every point on the grid, the module calculates the minimum Euclidean distance of that point from the boundary of the volume and saves all these distance values as a distance map. The points exactly on the boundary therefore have a zero value in the distance field. The default sign convention of the JIST plugin is that distances inside the original volume are positive and those outside are negative. One can change this default convention via the “Flip Sign” button (Figure 3.7). The other parameters that the user can adjust are iso-level and maximum distance (Figure 3.7). The parameter maximum distance defines the maximum positive or negative distance allowed in the calculations. It therefore is an estimate of the maximum expansion or contraction that can happen when the boundary evolves. The parameter iso-level value implements the expansion and contraction of the volume in all three directions. It can have any value between 0 and 1. Based on the chosen iso-level, distance field values change in discrete steps from voxel to voxel. An iso-level value of 1 implies expansion only, a value of 0 implies contraction only while a value between 0 and 1 implies both, expansion and contraction. For example, for the contraction only case, the distance field values outside the image volume are 0 while the values inside are positive numbers with a maximum governed by the maximum distance

parameter. The intensities in close proximity to the boundary are weighted averages of the intensities of the neighboring voxels. The module calculates the distance fields using the fast marching method.

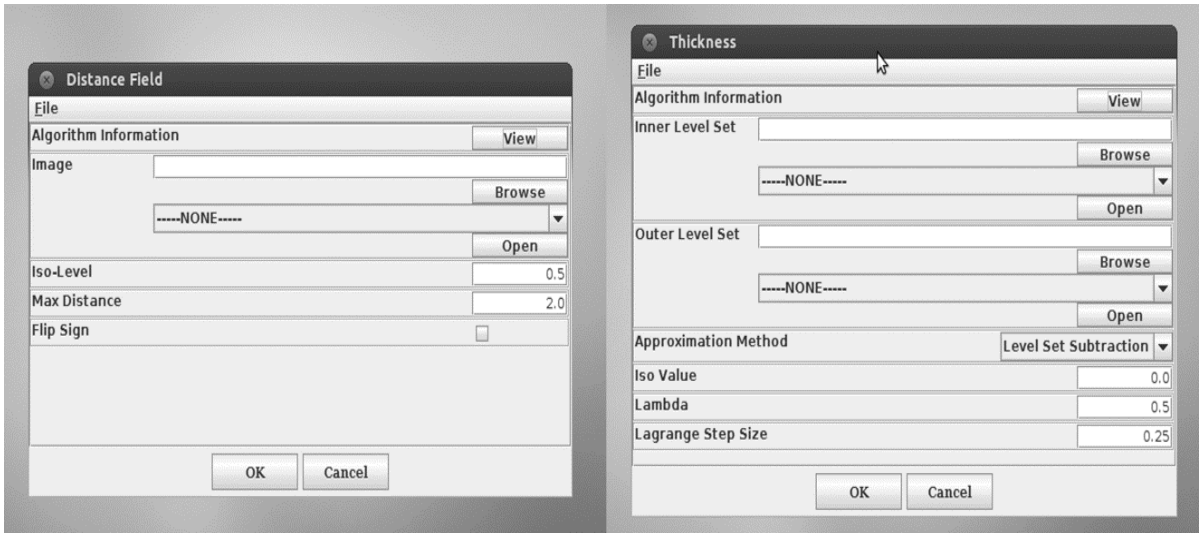

Figure 3.7: Screen shot of the JIST Distance Field (left) and Thickness (right) modules.

Using the distance field module, the level set functions for each of the outer boundaries of GM, GMm and WM were calculated. The following three level set functions were defined:

$$Levelset\ function\ for\ the\ GM\ outer\ boundary = \Phi_p\,,$$

$$Levelset\ function\ for\ the\ GMm\ outer\ boundary = \Phi_m\,,$$

$$Levelset\ function\ for\ the\ WM\ outer\ boundary = \Phi_w \qquad 3.14$$

Figure 3.8 shows a coronal slice through the level set function of the GM boundary from a representative dataset.

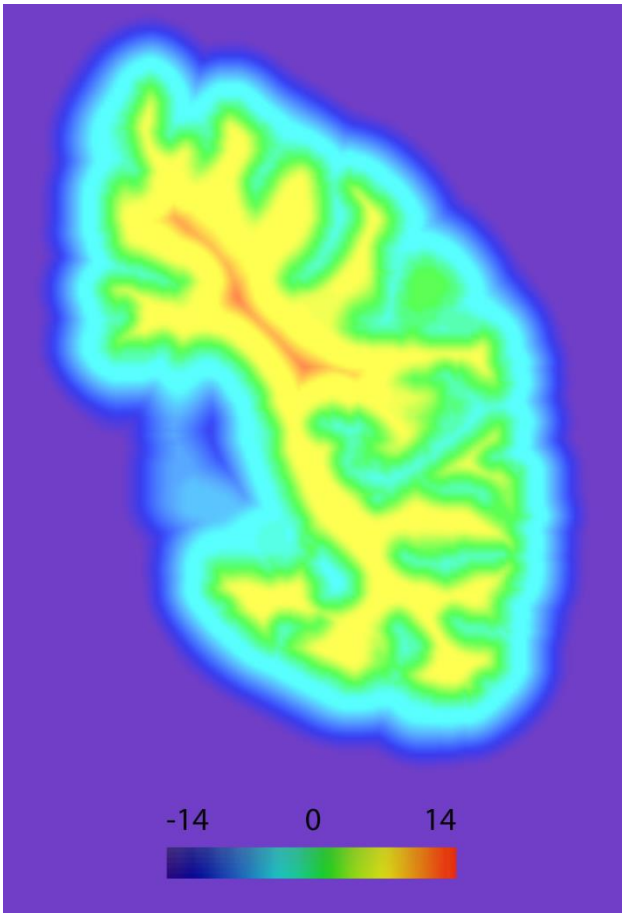

Figure 3.8: A slice through the level set function (distance field) for the GM boundary. The color map is shown using the color bar at the bottom. The background is at -15. The zero-level corresponds to the actual boundary.

3.5.2.2 Thickness calculations using distance fields

Thickness calculation of the tissue enclosed between any two boundaries was performed using the module "Thickness v1.5R" available as JIST plugin for MIPAV. The module takes the two level-set functions as input images. The user-defined parameters for the thickness module are iso-value, lambda and Lagrangian step size (Figure 3.7). The parameter iso-value defines the level-set

value in the two level-set functions that corresponds to the two surfaces. The only meaningful value for this parameter is 0, as all the boundaries are represented as the zero-level-set of respective functions. The lambda parameter is a regularization term that is associated with smoothness of the iso-surfaces as controlled by minimizing some meaningful cost function (for example volume). The parameter Lagrangian step size defines the step size used for changing lambda while finding the minimum of the associated cost function. The default values for these parameters, 0.5 and 0.25 respectively, were selected for calculations in this thesis.

The following thickness measurements (Figure 3.9) needed to obtain the proportional myelinated thickness, were defined:

$$Cortical\ thickness = t$$

$$Thickness\ of\ the\ strongly\ myelinated\ band\ in\ the\ deeper\ layers\ in\ the\ cortex\ = m \qquad 3.15$$

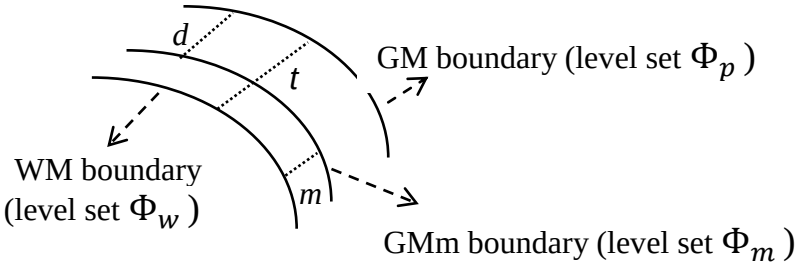

Figure 3.9: A schematic diagram showing the various thickness measurements in the cortex.

Cortical thickness t was obtained by subtracting the WM level set function Φ_w from the GM levelset function Φ_p . However, m was not calculated directly. Instead, the depth d of the outer boundary of myelinated band inside the cortex was found by subtracting the GMm level set function Φ_m from the GM set function Φ_p , and then m was calculated as a difference of t and d. Performing all the thickness measurements as distances from the pial surface ensures that the thickness data can be projected on the pial surface for display.

$$Thickness\ of\ the\ unmyelinated\ GM\ in\ the\ outer\ layers = d \qquad 3.16$$

Thus,

$$t = \Phi_p - \Phi_w$$

$$d = \Phi_p - \Phi_m$$

$$m = t - d \qquad 3.17$$

The equality between m and $t - d$ holds for nested surfaces and in regions where strong myelination persists continuously in all the deeper layers of the cortex.

3.5.3 The proportional myelinated thickness

The morphological quantity that was used to determine the extent of M1 in the precentral gyrus is the relative thickness of myelinated tissue in the cortex. The proportional myelinated thickness p was defined as the ratio of myelinated thickness to the cortical thickness.

$$Proportional\ myelinated\ thickness\ (p) = \frac{m}{t} \qquad 3.18$$

Therefore,

$$p = \frac{t - d}{t} \qquad 3.19$$

In the presence of partial volume effects, the measured thickness values are altered. The effect of partial voluming on proportional myelinated thickness is approximated as follows. The segmentation error *e* was expressed as a fraction f of the cortical thickness t. Let t_1 and m_1 represent the cortical thickness and myelinated cortical thickness respectively, altered due to partial voluming of GMm into WM (Figure 3.10).

$$t_1 = t + f \cdot t, \qquad m_1 = m + f \cdot t \qquad 3.20$$

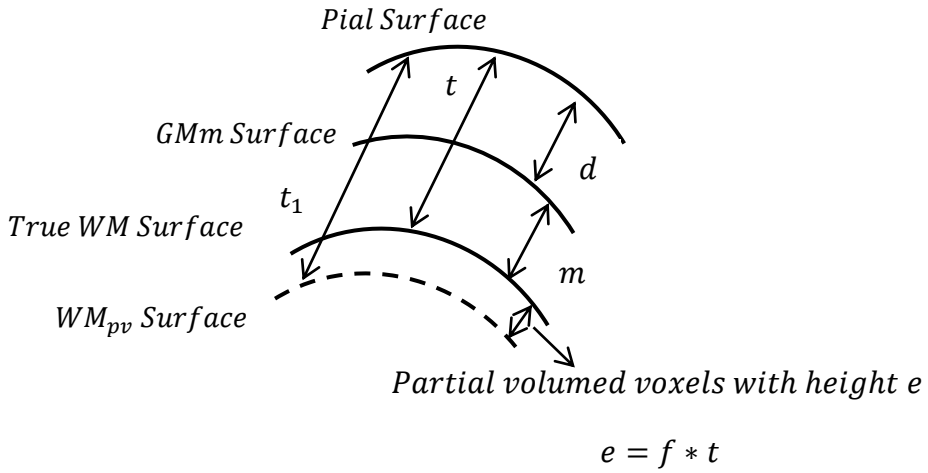

Figure 3.10: A schematic drawing of the cortex as a set of three nested surfaces. The WM boundary is displaced towards the WM due to significant partial voluming effects at this high-curvature boundary. The displaced WM boundary is shown by the dotted line (***WM_{pv} Surface***).

The definition of the WM boundary is affected by partial volume (pv) effects the most, because of its higher curvature. The partial voluming at the GM and GMm boundaries is presumably smaller in comparison with the partial voluming at the WM boundary. Therefore, it was assumed that the quantity d, does not change significantly in the presence of partial voluming errors.

$$Proportional\ myelinated\ thickness\ p = \frac{t-d}{t} = 1 - \frac{d}{t} \qquad 3.21$$

$$Error\ in\ the\ proportional\ myelinated\ thickness = \partial p$$

$$\partial p = \partial t \cdot \frac{dp}{dt}$$

$$\partial p = (f \cdot t) \cdot \left(\frac{d}{t^2}\right)$$

$$\partial p = f \cdot \frac{d}{t} = f \cdot (1 - p) \quad 3.22$$

The fractional error in p therefore becomes the following.

$$\frac{\partial p}{p} = f \cdot \frac{1 - p}{p} \quad 3.23$$

For comparison, one can calculate the fractional error in the thickness of the myelinated cortex as follows.

$$Fractional\ error\ in\ the\ myelinated\ cortical\ \ thickness = \frac{\partial m}{m}$$

$$\frac{\partial m}{m} = \frac{f}{p} \quad 3.24$$

A comparison of the fractional error in p (Equation 3.23) and m (Equation 3.24) indicates that for regions of the cortex where myelinated gray matter spans more than half of the cortical thickness, partial voluming error in the proportional myelinated thickness p is lesser than the corresponding errors in myelinated thickness m, regardless of the magnitude of f. Figure 3.11 shows the variation of fractional error in p and m versus p and f. The graph shows that even if 50% of the pixels in the cortex are wrongly classified due to partial volume effect, the error in p is less than 30% for areas of high myelinated thickness. Therefore, proportional myelinated thickness is a robust morphological metric for cortical

mapping. Being a ratio of the two thickness measures, it is relatively immune to the partial volume effects which severely affect the cortical thickness measurements.

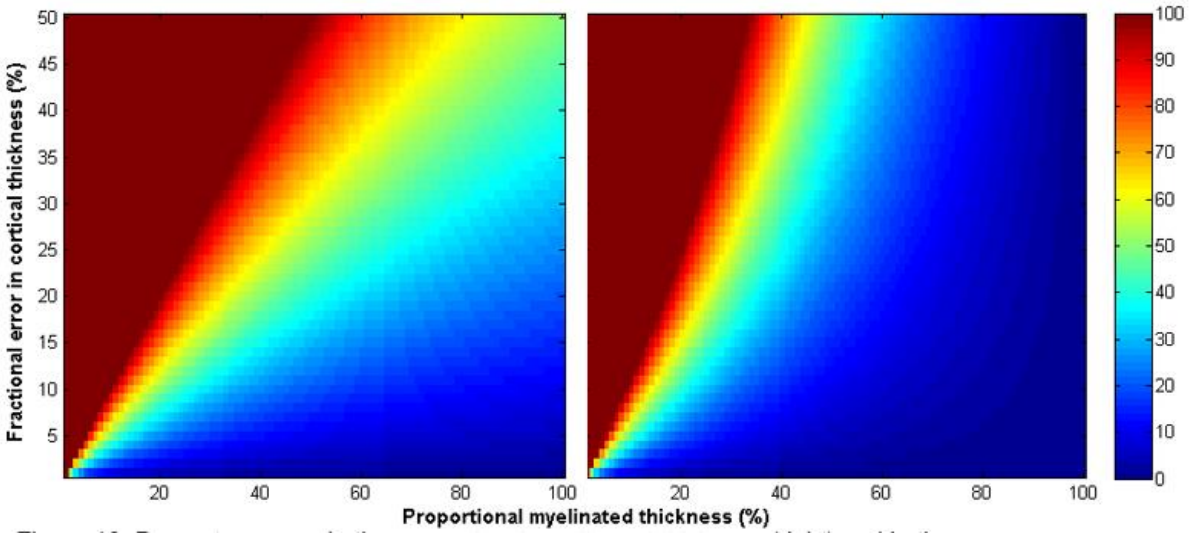

Figure 3.11: Percentage error in myelinated thickness (left) and proportional myelinated thickness (right) as a function of percentage error in cortical thickness (y-axis) and proportional myelinated thickness (x-axis).

3.6 Visualization

Using the pial surface labels, triangulated iso-surfaces were generated in AMIRA, using the fast marching cube (FMC) algorithm. The algorithm takes 8 neighboring points as vertices of a cube and determines the triangle representing part of the iso-surface passing through the cube (Lorensen and Cline, 1987). The algorithm then connects the triangles to generate the iso-surface.

The proportional myelinated thickness data and the total cortical thickness data were projected onto the iso-surface representing the pial boundary. For

visualization purpose only, the surface was smoothed and slightly inflated so that the sulcal boundaries would become visible. Figure 3.12 shows a representative pial surface.

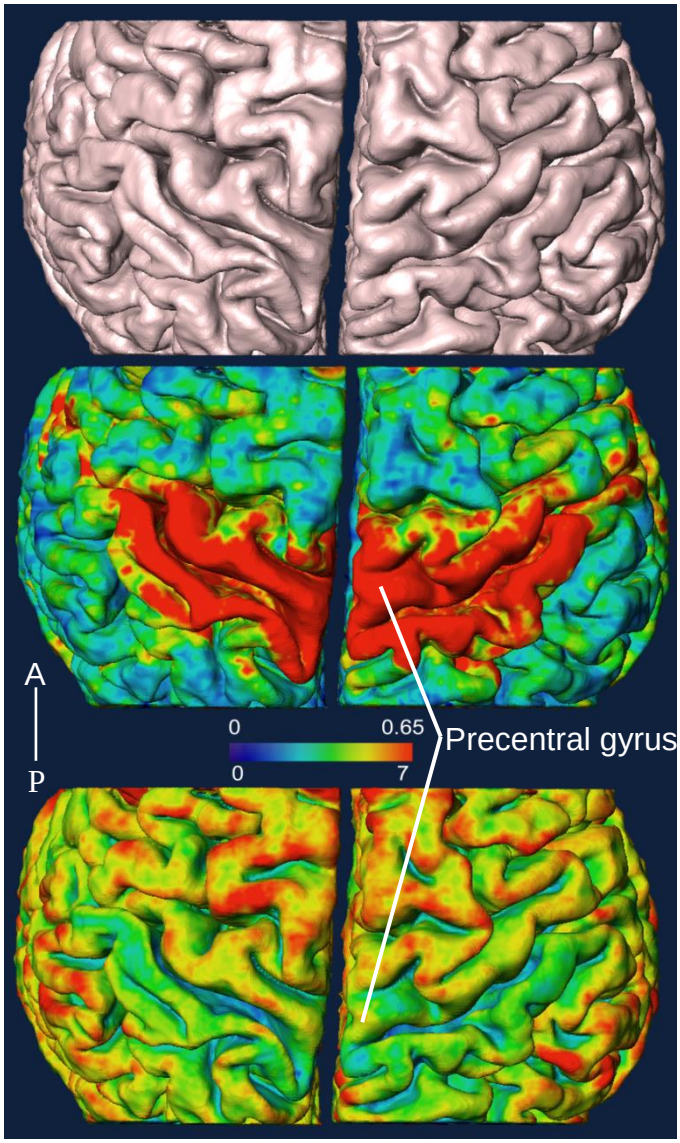

Figure 3.12: Dorsal view of a representative pial surface with no thickness data (top panel), proportional myelinated thickness data (middle panel) and cortical thickness data (bottom panel). The numbers at the top of the color bar correspond to the middle panel while those at the bottom correspond to the bottom panel. A = Anterior and P = Posterior.

3.2 Discussion

The goal of this image processing pipeline was to prepare brain images for measurement of the surface area of motor fields in the precentral gyrus as defined using the proportional myelinated thickness. Measurement of the surface area involves demarcating the ROI comprising of the precentral gyrus and then cropping it to perform area measurement. As Figure 3.12 shows, the proportional myelinated thickness data when projected on the pial surface, makes it possible to mark the anterior boundaries of the precentral gyrus in the frontal cortex. Furthermore, the cortical thickness data and anatomical location information help in delineating the ROI from the posteriorly adjoining postcentral gyrus. Thus at the end of image processing, one can demarcate an ROI consisting of the precentral gyrus in each hemisphere. The ROI cropping and surface area measurements based on the proportional myelinated thickness data are presented in the next chapter.

The image processing protocols mostly used freely available software and required minimum manual work. With the current scheme, it takes about one week to process one dataset completely. The challenges in constructing this pipeline are many. The first challenge was dealing with the sub-mm resolution. Most of the brain image processing software only works with 1 mm isotropic resolution. Higher resolution also increases the processing time because the data size is increased. The second challenge was that images in this study consisted of partial brain scans, roughly over the middle one-third of the brain. Thus, using

FreeSurfer, which is designed to start its processing pipeline with whole head images, results in labels with some missing gyri especially in slices close to the beginning and end of the image where there are abrupt changes in intensity. Fixing these labels requires some manual intervention. The third challenge came from the novel four-tissue segmentation scheme used in this study. Many neuroimaging software packages do not have provision for more than three tissues. The manual work is involved in the refinement of the brain mask and in image cropping. While CBS tools provide options for brain mask refinement, so far these options work with whole brain data set segmented into three tissues of GM, WM and CSF only. Manual work in brain mask refinement can be minimized if whole brain images with good SNR are acquired in all the subjects. In that case, the whole brain images can be registered to a common template, such as the Talairach atlas (Talairach and Tournoux, 1988). The refining and cropping steps can be performed on the registered dataset, and results can be propagated back to the individual images. Registration to standard atlases however will need down sampling of the high resolution data. Therefore, some manual touch-up of the refined masks will be required when the data is sampled back to the original resolution.

4 Morphological study of the primary motor cortex in four lower limb amputees and age- and sex-matched controls

4.1 Introduction

Functional plasticity studies in the primate cortex show reorganization in the primary functional regions as a consequence of major changes in function (Roiha *et al.*, 2011; Qi *et al.*, 2010; Rockstroh *et al.*, 2000). For example, in upper limb amputees, the face and stump muscle representations in the primary motor cortex have been shown to be displaced toward the former hand representation (Lotze *et al.*, 2001). Such evidence of functional reorganization as a result of disrupted motor output pathways suggests that there may be accompanying changes in the structure of the primary motor cortex. With recent advances in neuroimaging using anatomical magnetic resonance imaging (MRI) and image processing techniques, it is now possible to investigate the morphological features of cortical areas associated with primary functions, such as the precentral motor cortex, for plasticity studies.

In this thesis, T_1 -weighted anatomical MRI was used to investigate whether the anatomical structure of the motor fields in the precentral motor cortex is altered as a result of lower limb amputation in humans. Specifically, intracortical myelin was imaged, whose distribution can delineate motor regions in the human cortex (Glasser and Van Essen, 2011). In a basic description of the motor system, upper motor neurons in the motor cortex synapse with lower motor

neurons in the spinal cord which then project to muscles. The descending axons of the motor neurons are well myelinated (Bishop and Smith, 1964). Limb amputation severs the axons of the lower motor neurons that were innervating the now lost limb, thereby disrupting that motor pathway. The question then arises whether this affects cortical structure. For instance, the upper motor neurons and their axons that were contributing to the movement of muscles in the previously intact limb could degenerate when their prescribed output pathway is disrupted. Or the upper motor neurons in that region may remain viable and rewire to serve other body areas.

A degeneration of upper motor neurons and their associated myelinated axons could affect several structural features in the motor cortex, including cortical gray matter volume and the thickness of the cortex. The available data on structural changes in the brain resulting from the loss of motor output is limited and in some cases, contradictory. For example, one volumetric study in amputees reported a loss of gray matter in the primary motor cortex M1 (Preissler *et al.*, 2013) while another study found no loss of gray matter (GM) in M1 (Draganski *et al.*, 2006). A cortical thickness study in subjects with temporary limb immobilization in response to injury found a decrease in cortical thickness in the contralateral M1 (Langer *et al.*, 2012).

Another structural feature of the cortex that could be affected by the degeneration of upper motor neurons is the overall surface area of the primary motor cortex. There are no studies yet available which investigate changes in the

surface area of the motor cortex as a result of amputation. As the motor cortex is known to have a somato-topic representation of the various limbs (Penfield and Rasmussen, 1950), referred to as the motor homunculus (Figure 4.1), one can speculate that a loss of upper motor neurons dedicated to the previously intact limb's movements might result in a reduced surface area in the contralateral primary motor cortex as that part of the homunculus disappears.

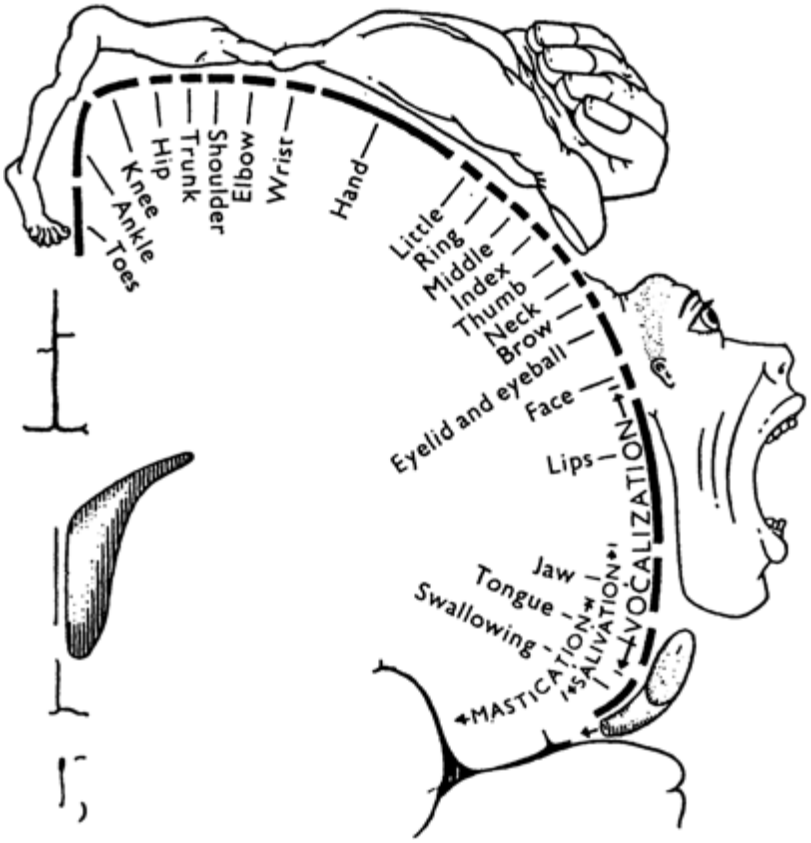

Figure 4.1: Motor homunculus showing the somatotopic organization of various body parts in the primary motor cortex in the precentral gyrus (Original work by (Penfield and Rasmussen, 1950)- reprinted with permission from (Nieuwenhuys *et al.*, 2008)).

For *in vivo* anatomical imaging studies of the cortex, one of the challenges is to accurately identify the boundaries of the primary functional fields from structure alone. A distinguishing structural feature of the primary functional areas is the high myelin content in comparison with the intervening cortex. Recent anatomical MRI studies have shown that the variation of overall myelin content along the cortical surface can be used for *in vivo* cortical mapping in humans (Cohen-Adad *et al.*, 2012; Glasser and Van Essen, 2011). For the present study, features of the myeloarchitecture of the precentral gyrus were used to identify motor areas. The cortex was imaged using a T_1-weighted MRI sequence at 3T, optimized to obtain enhanced contrast across the cortex based on intracortical myelin (Bock *et al.*, 2013). The precentral gyrus is the thickest part of the cortex at 4.5 mm (Zilles and Amunts, 2012) and it was imaged using 0.7 mm isotropic resolution to improve visualization of intracortical myelin versus a typical anatomical MRI at 1 mm isotropic resolution. Intracortical myelin mostly consists of horizontal and radial myelinated fibers of variable caliber. Two structures the horizontal fibers constitute are the inner and outer stripes of Baillarger (B_{in} and B_{out}) in sub-layers V-b and IV-b of the cortex (Braitenberg, 1962). B_{in} and B_{out} vary across the cortex in their thickness and in the density of myelinated fibers they contain. The thickness of unmyelinated GM between B_{in} and B_{out}, referred to as the intra-striate gap, also varies across the cortex (Braak, 1980; Braitenberg, 1962; Nieuwenhuys, 2013). Studies of myeloarchitecture indicate that the dorso-medial part of the precentral gyrus and the anterior wall of the central sulcus have

a unique myelination pattern (Braak, 1980; Braitenberg, 1962; Nieuwenhuys, 2013; Vogt and Vogt, 1919; Vogt, 1951). Here, the strongly myelinated B_{in} and B_{out} merge together and also with the underlying cortical layers, a characteristic referred to as *astriate* in the myeloarchitecture literature. The radial bundles of myelinated fibers in this part extend beyond the outer stripe of Baillarger to the deeper parts of the upper pyramidal layer, a characteristic referred to as *euradiate* in the myeloarchitecture nomenclature. With an indiscernible inner granular layer and a well- developed external pyramidal layer, the *astriate* and *euradiate* features suggest that dense myelination persists through most of the cortical thickness in this area (Figure 4.2). Myeloarchitecture of the remaining precentral motor region differs from the above description (Braak, 1980; Braitenberg, 1962; Vogt and Vogt, 1919), with the overall myelin density being reduced in the lateral parts of the gyrus. Also, due to the presence of unmyelinated GM between B_{in} and B_{out}, the outer stripe of Baillarger can be distinguished from the inner stripe which is still mostly merged with the underlying cortical layers (Figure 4.2). Thus, we postulated that the precentral motor region can be thought of as consisting of two sub-regions: a dorso-medial core region with dense myelination that persists through most of the cortical thickness starting from the deepest layer and extending continuously to a very superficial layer, and an outer belt with relatively reduced myelin density and myelination not spanning most of the cortical thickness. The heavily myelinated core region consists of the complete Brodmann's area 4 and a portion of area 6 (Brodmann,

1909; Zilles, 2004). This region, which contains the entire functionally defined primary motor cortex, is referred to as M_m in this study, while the rest of the precentral motor cortex which is relatively unmyelinated is referred to as M_u. The unique myeloarchitectonic feature of M_m is that the myelinated portion of the cortex is thicker than in the adjacent cortex and this can be used to distinguish it from M_u. The ratio of thickness of myelinated tissue to the total cortical thickness, referred to as the proportional myelinated thickness (p) in this study, is higher in M_m. Therefore, the proportional myelinated thickness was used as a metric to distinguish between M_m and M_u in this study.

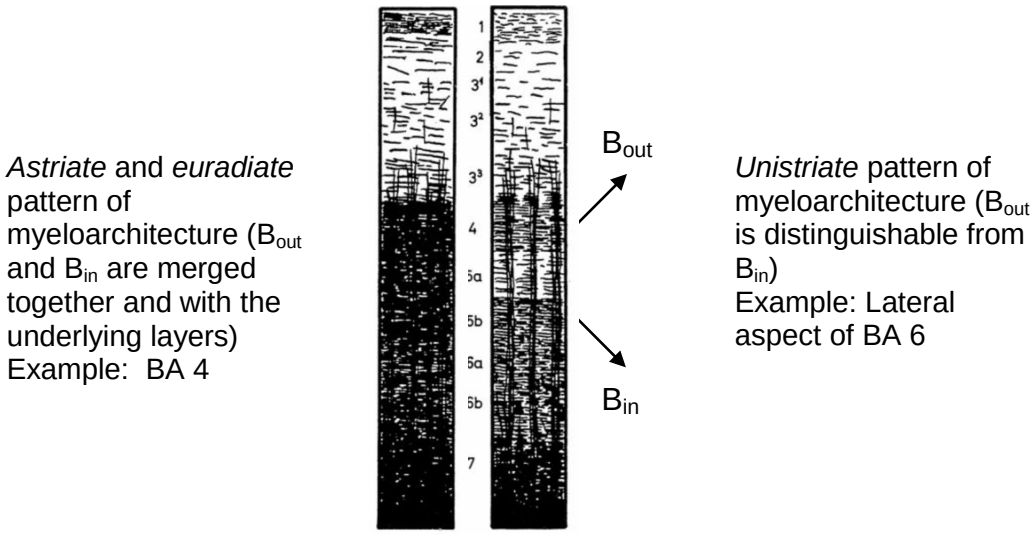

Figure 4.2: A schematic diagram of two types of myeloarchitectonic patterns in the precentral motor cortex. The Arabic numerals between the two panels represent cortical layers, with 1 being the outermost (Reprinted with permission - (Nieuwenhuys, 2013)).

Functional studies of the homunculus in humans indicate that upper motor neurons in the most dorsal and medial parts of M1 project to those lower motor neurons that innervate the lower limbs (Figure 4.1) (Penfield and Rasmussen,

1950). Therefore, we hypothesize that if structural degeneration of these upper motor neurons happens as a consequence of lower limb amputation, a decrease in the proportional myelinated thickness in M_m could be observed. There could also be a reduction in the area of M_m. Using the proportional myelinated thickness in the precentral motor cortex, the area of M_m was measured in four lower limb amputees and also in their age and sex matched healthy controls for comparison. Through this, we hoped to gain insight whether upper motor neurons degenerate when they are deprived of their original output, resulting in changes in the morphology of cortical fields associated with the primary motor function.

4.1.1 Methods

4.1.2 Subjects

Four male, lower-limb amputees and four male age-matched controls were scanned for this study. None of the subjects reported neurological conditions. The nature of the injuries in the amputees is summarized in Table 4.1. The study was approved by the Research Ethics Board (REB # 11-3598) at St. Joseph's Healthcare (Hamilton, ON, Canada) and informed consent was obtained from all subjects prior to imaging.

	Age of amputee (years)	Lost limb	Years since loss	Age of matched subject (years)
1	46	Left leg; below knee	37	44
2	51	Right leg; below knee	49	50
3	72	Left leg; below knee	65	64
4	49	Right leg; below/ above knee	39/4	50

Table 4.1: Subject information

4.1.3 MRI

Subjects were scanned using a GE 3 T MR750 scanner (General Electric Healthcare, Milwaukee, WI, Software Version DV 22.0) with a whole body single element transmit coil (GE) and a 32 channel receive array head coil (MR Instruments). The details of the imaging protocols are summarized in Table 4.2. A 3D, T_1-weighted magnetization prepared, gradient echo sequence (BRAVO-GE's version of MPRAGE) was optimized to obtain enhanced intracortical contrast, suitable for visualizing intracortical myelin at 0.7 mm isotropic resolution (Bock *et al.*, 2013). To reduce the imaging time, partial brain images in the anterior-posterior (AP) direction were acquired to reduce the phase encode steps along that axis. The field-of-view (FOV) was a rectangular axial slab which fully encompassed the central sulcus, approximately centered at the precentral gyrus along the AP axis. The FOV covered the brain fully along the other two anatomical axes. The T_1-weighted BRAVO scan was followed by a predominantly proton density-weighted, 3D FSPGR (Fast Spoiled Gradient Recalled echo, aka FLASH - Fast Low Angle Shot) acquisition over the same FOV, to be used in post-processing to compensate for RF field inhomogeneities (Marques *et al.*, 2010; Van de Moortele *et al.*, 2009). The total acquisition time for the protocol was about 40 min per subject.

Parameter	Optimized BRAVO	FLASH
Excitation angle *α*	12°	4°
$FOV_{readout}$ x FOV_{pe1} x FOV_{pe2} (mm)	240 x 192 x 82.6	240 x 192 x 82.6
Imaging matrix	344 x 275 x 118	344 x 275 x 118
Number of *α* pulses per inversion-N_{pe2}	118	118
Resolution	0.7 mm isotropic	0.7 mm isotropic
TR (between successive *α* pulses)	9.9 ms	9.9 ms
TE (Echo time)	4.1 ms	4.1 ms
TI (Inversion time)	1000 ms	-
TD (Time delay at the end of each cycle)	1100 ms	-
Acquisition time	15 min	5.3 min
Number of averages (NEX), separately acquired	2	2

Table 4.2: A summary of the imaging parameters. *N* stands for the number of excitation pulses; *pe1* represents the first phase encoding direction while *pe2* is the second phase encoding direction.

4.1.4 Post processing

To minimize postural differences during image acquisition, the BRAVO and FLASH images from each subject were co-registered using a 6-parameter affine transformation in Amira (Visage Imaging) with Lanczos resampling. The two registered FLASH images were summed then smoothed twice using a 3D median filter of kernel size 3 pixels to reduce noise. The filter was applied twice since the kernel size cannot be increased in Amira. The sum of the two co-registered BRAVO images was divided by the filtered, average FLASH image. The BRAVO images and the FLASH images have similar receive field (B_1^-) profiles; hence their division produces a ratio image with greatly reduced B_1^- inhomogeneity. The transmit field inhomogeneity (B_1^+) is also reduced in the ratio image (Marques *et al.*, 2010; Van de Moortele *et al.*, 2009). Each ratio image was then resampled to a 1 mm isotropic resolution and FreeSurfer

(http://surfer.nmr.mgh.harvard.edu/) (Fischl *et al.*, 2002) was used to extract labels for the cerebrum masked to the pial/cerebral spinal fluid (CSF) boundary. The labels were resampled back to 0.7 mm isotropic resolution to mask the cerebral hemispheres in the original 0.7 mm isotropic resolution ratio image. The subcortical gray matter structures including the basal ganglia and thalamus were manually removed from the masked ratio image, leaving only the cortex and underlying white matter tracts. The ratio image was then segmented into four brain- tissue classes, gray matter (GM), myelinated GM (GMm), white matter (WM) and cerebrospinal fluid (CSF) (Figure 4.3). This tissue segmentation was performed with a fuzzy c-means clustering algorithm (Pham and Prince, 1999) in the software package: MIPAV (version 7.0.1, http://mipav.cit.nih.gov/). After segmentation, the two hemispheres were separated for subsequent processing. The output of the fuzzy c-means segmentation was used to produce tissue labels for GM, GMm, and CSF using a fuzzy membership value of 1 for those tissue classes. The WM labels were produced using a fuzzy membership level of 0.1. This membership level was used to account for the very thin WM blades in the crowns of the gyrii where WM intensity is reduced due to partial voluming. Finally, in each tissue class, unconnected islands containing less than 15 voxels and with mean intensity closer to other tissue classes were removed from the main cluster. The post processing was performed in Amira, unless otherwise stated.

4.1.5 Thickness measurements

The following morphological quantities were determined in each hemisphere (Figure 4.3).

$$Cortical\ thickness = t,$$

$$Thickness\ of\ the\ unmyelinted\ GM\ in\ the\ outer\ layers = d$$

$$Thickness\ of\ the\ well\ myelinated\ deeper\ \ cortex = m \qquad 4.1$$

For these measurements, level set functions were created for the three boundaries, namely the outer cortical boundary (CSF/GM), the outer myelinated cortical boundary (GM/GMm) and the outer white matter boundary (GMm/WM) using the Java Image Science Toolkit (JIST) implementation of the Distance Field (1.3 R) module in MIPAV (Lucas *et al.*, 2010).

$$Levelset\ function\ for\ the\ outer\ cortical\ boudary = \emptyset_p\ ,$$

$$Levelset\ function\ for\ the\ outer\ myelinated\ cortical\ boundary = \emptyset_m$$

$$Levelset\ function\ for\ the\ outer\ white\ matter\ boundary = \emptyset_w \qquad 4.2$$

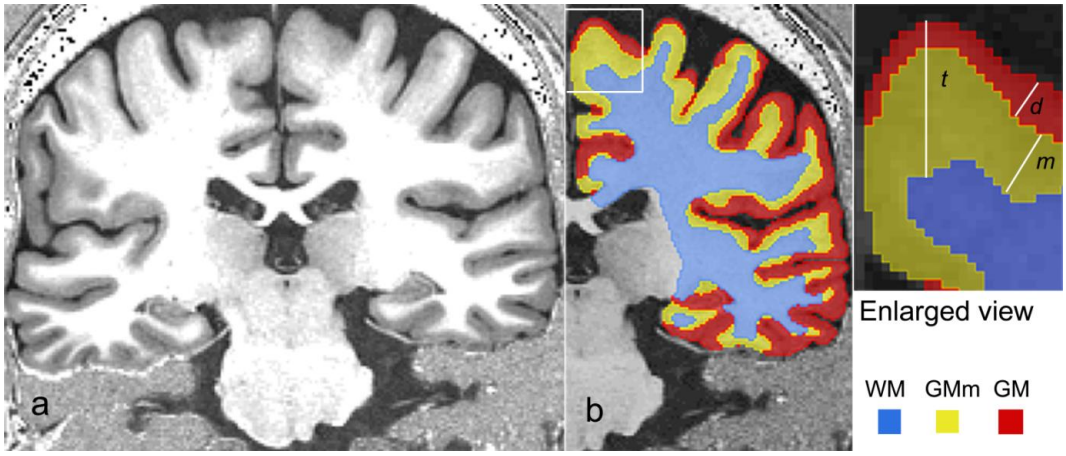

Figure 4.3: A representative MRI slice is shown in Panel a. The tissue classification for the right hemisphere of this MRI is shown in Panel b. On the right, various thickness measurements are shown schematically in an enlarged corner of b. Here, cortical thickness is represented as *t*, thickness of the myelinated cortex as *m* and depth of the myelinated cortex below the outer cortical boundary as *d*.

The cortical thickness, *t*, was obtained by subtracting the WM level set function, $\emptyset_w$,from the pial surface level set function, $\emptyset_p$. Similarly, thickness *d* was calculated by subtracting the GMm level set function $\emptyset_m$ from the pial level set function $\emptyset_p$. These thickness calculations were performed using the JIST implementation of the Thickness (1.5 R) module in MIPAV (Lucas *et al.*, 2010). Next, the difference of these two thickness measurements was calculated to represent the distance between the outer edge of the strongly myelinated band in the cortex and the WM surface. For nested surfaces and in regions where strong myelination persists continuously in all the deeper layers of the cortex, this is equivalent to the thickness *m* of the strongly myelinated deeper cortex.

$$m = t - d \quad (4.3)$$

Finally, the proportional myelinated thickness was calculated according to the equation below.

$$Proportional\ myelinated\ thickness\ (p) = \frac{t-d}{t} \quad (4.4)$$

Performing all the thickness measurements as distances from the outer GM boundary, also known as the pial surface, ensured that the thickness data is defined at the pial surface for display.

4.1.6 A description of the region of interest (ROI)

The primary motor fields are known to be located in the precentral cortex. The precentral cortex consists of the precentral gyrus and superior, middle and inferior frontal gyrii on the dorsal and lateral parts of the hemisphere and the anterior two-third part of the paracentral lobule on the medial aspect of the hemisphere. Functionally, the precentral cortex is dedicated to the primary motor area (M1or BA 4) and the premotor area (BA 6) (Brodmann, 1909; Zilles, 2004), and this anatomical division of BA 4 and BA 6 in the precentral motor cortex is with reference to histological studies (Geyer *et al.*, 2000). The major anatomical features and landmarks in the precentral cortex are shown in Figure 4.4. The primary motor cortex or BA 4 is the most posterior part of the precentral cortex. It occupies the anterior wall of the central sulcus for the most part, medial part of the free surface of the precentral gyrus and a portion of the paracentral lobule.

Anteriorly adjoining BA 4 is premotor area or BA 6 which occupies the rest of the precentral motor cortex.

The well-myelinated area M_m in the precentral gyrus presumably consists of the entire BA 4 and partial BA 6. Thus the ROI in this study is the entire precentral gyrus and anterior part of the paracentral lobule in the precentral cortex. The boundaries of the ROI were mostly defined using anatomical landmarks (Figure 4.4). The posterior boundary of the precentral gyrus is in the depth of the central sulcus (CS) (Geyer *et al.*, 2000). The shape of the most medial part of the precentral gyrus and the central sulcus show some variability between people. In some cases, the central sulcus extends all the way to the medial longitudinal fissure separating the two hemispheres. In other cases, the sulcus terminates before that and the cusp of the precentral gyrus merges with the cusp of the postcentral gyrus without a dip in between. Thus, the posterior boundary of motor region in the paracentral lobule was determined by considering an imaginary line, through the cusp of the gyrus or depth of the sulcus, extending the central sulcus to the paracentral lobule. The anterior bank of the precentral gyrus was marked as the deepest point in the precentral sulcus, except where it merges onto the inferior and middle frontal gyrii. Where it merges with these gyrii, an imaginary geometrical line extending the precentral sulci and running parallel to the precentral gyrus was considered as the boundary. The superior frontal gyrus merges with the paracentral lobule medially and with the precentral gyrus dorsally; it is thus hard to geometrically define the anterior

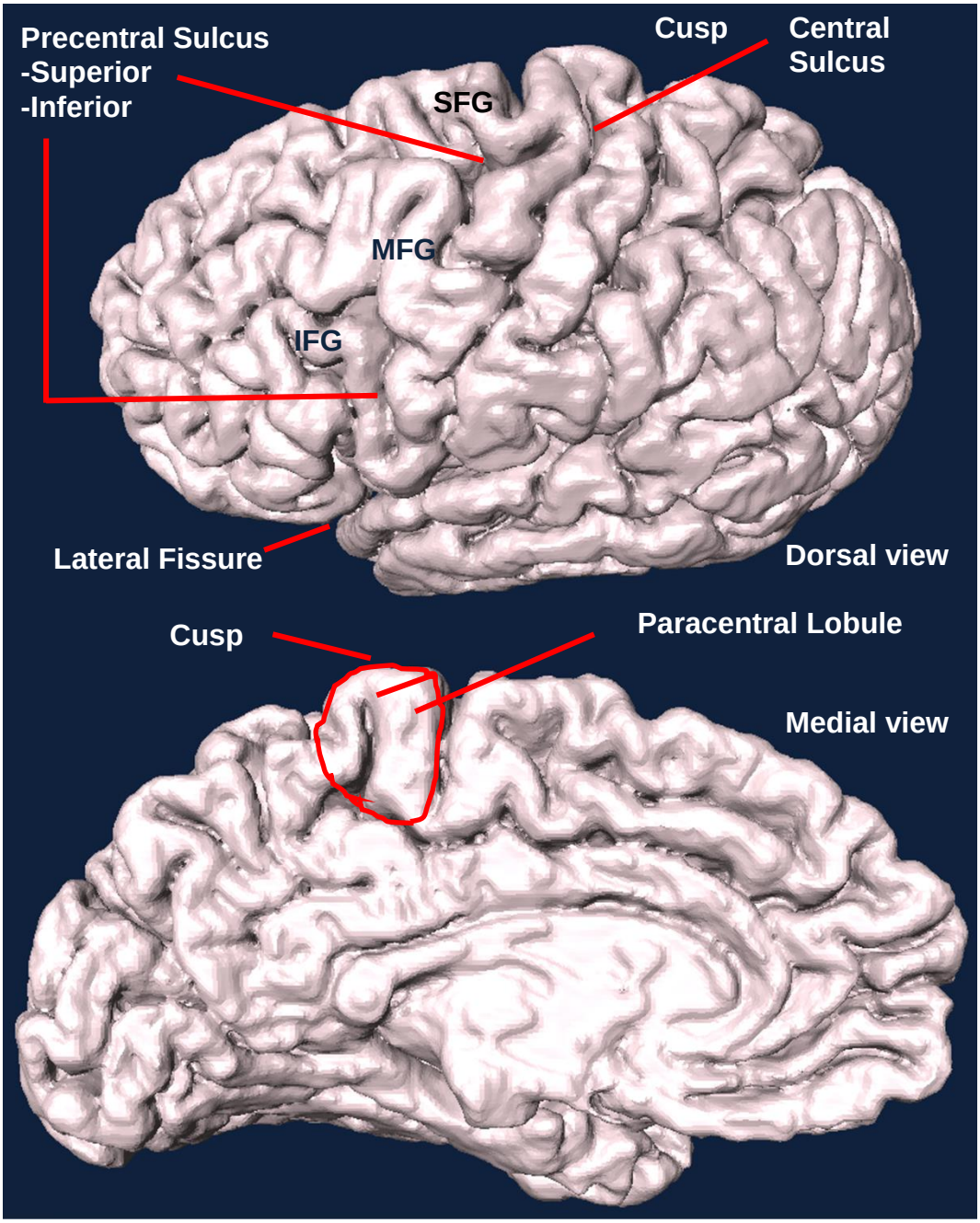

Figure 4.4: Major anatomical landmarks used in defining the boundaries of the ROI. IFG, MFG and SFG represent the inferior, middle and superior frontal gyri, respectively.

boundary of the ROI in the most dorso-medial location. However, as the medial and dorsal parts of the precentral gyrus are described to have relatively high myelinated thickness, this boundary was defined by locating sudden decrease in the proportional myelinated thickness. Along the medial-lateral axis, the precentral gyrus extends from the most medial part of the hemisphere to the Sylvian or lateral fissure.

The ROI is shown in one representative hemisphere in Figure 4.5.

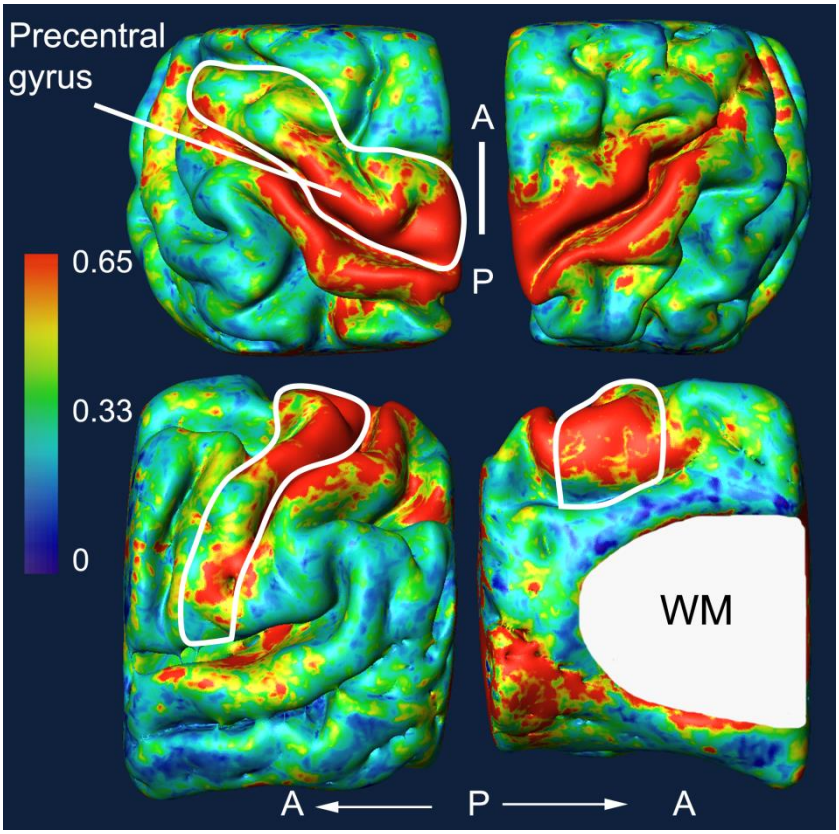

Figure 4.5: Inflated view of the pial surface in one representative subject with proportional myelinated thickness data. The top row shows the dorsal view of both the hemispheres. The bottom row shown the lateral view (left) and the medial view (right). The sub-cortical WM is masked to avoid distraction. The ROI comprising of the pre-central gyrus is roughly drawn with white lines. A = Anterior, P = Posterior.

4.1.7 Display and cropping the ROI

The outer cortical boundary was surface-rendered into a triangular mesh, using the “fast marching cubes” (FCM) (Lorensen and Cline, 1987) algorithm in Amira, to represent the pial surface for visualization and further measurements. The proportional myelinated thickness data was projected on the pial iso-surface for display (Figure 4.5).

The pial iso-surface with proportional myelinated thickness data projected on it was used as a visual help in determining the boundaries of the ROI.

The ratio image was cropped by deleting the voxels outside the ROI consisting of the precentral gyrus. The cropped ROI was also surface-rendered into a triangular mesh using the “fast marching cubes” (FCM) (Lorensen and Cline, 1987) algorithm in Amira, for surface area measurements (Figure 4.6). The proportional myelinated thickness data was projected on the triangle nodes of the cropped pial surface.

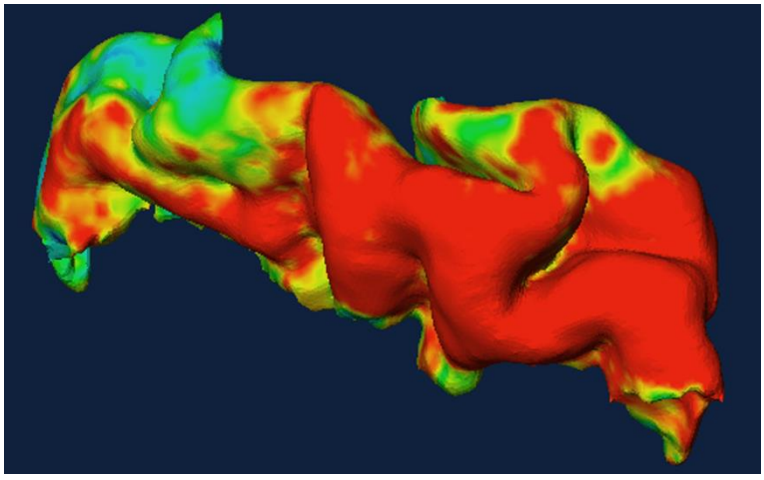

Figure 4.6: A representative ROI obtained after cropping the left hemisphere shown in Figure 4.4. The color map is the same as used in Figure 4.5.

4.1.8 Surface area measurements

The thickness data on the nodes along with the triangulation information was exported to Matlab (The Math Works, Natick, MA). A Matlab code was written to calculate the distribution of the surface area of the precentral gyrus as a function of the proportional myelinated thickness (*p*) binned between *p* = 0 and *p* = 1 in steps of 0.01. As there are two sub-regions in the ROI: one with comparatively higher proportional myelinated thickness and the other with lower values of proportional myelinated thickness, the distribution of surface area versus proportional myelinated thickness is expected to have two distinguishable peaks corresponding to these two sub-regions. To test this, a bimodal Gaussian function was fit to the binned surface area data using a least-squares, non-linear curve fitting algorithm in Matlab (The Math Works, Natick, MA). Equation 4.5 below describes the bimodal Gaussian model used for the fit.

$$Fit = C1 * e^{\frac{-(x-\mu 1)^2}{2\sigma 1^2}} + C2 * e^{\frac{-(x-\mu 2)^2}{2\sigma 2^2}} + C3 \qquad 4.5$$

Here, *C1* and *C2* are constants representing the peak heights and *C3* is a constant included in the fit to accommodate any constant bias; μ_n and σ_n are mean and variance of the n^{th} Gaussian function. The goodness of fit was evaluated by calculating R-squared values adjusted for the degrees of freedom, and also by plotting the residuals. Using the fit parameters, the two Gaussian functions were separated. The first Gaussian with lower mean proportional myelinated thickness was taken to represent the relatively unmyelinated sub-

region M_u. Therefore, the mean of the first Gaussian was taken as the mean proportional myelinated thickness in the sub-region M_u. The second Gaussian with higher mean proportional myelinated thickness was taken to represent the well myelinated sub-region M_m. Therefore, its mean was taken as the mean proportional myelinated thickness in the sub-region M_m and area under its curve was calculated as an estimate of the area of M_m.

Interhemispheric differences in the area of M_m were assessed by calculating the absolute difference between the area of M_m on the left and right side of the brain, and dividing it by the average of left and right M_m areas.

4.1.9 Statistics

Amputees and controls were statistically compared on the basis of two morphological quantities: the mean proportional myelinated thickness in each of the sub-regions in the ROI and surface area of the sub-region with higher proportional myelinated thickness (M_m). These morphological quantities were also compared between the hemispheres in the same group. All the comparisons were made using Student's t-test with the significance level set at 0.05.

4.2 Results

4.2.1 Existence of two sub-regions in the precentral motor cortex

To verify the existence of two sub-regions M_m and M_u in the ROI, a bimodal Gaussian function (Equation 4.5) was fit to the distribution of surface area versus proportional myelinated thickness in all 16 hemispheres included in

the study. Figure 4.7 shows a plot of the area distribution, the bimodal fit and the two separated peaks versus proportional myelinated thickness in a representative subject. These graphs demonstrated a curve with two distinct peaks having overlapping distributions. The bimodal Gaussian function (Equation 4.5) fit the data very well as determined by goodness of fit. R-squared values (adjusted for degrees of freedom) ranged from 0.87 to 0.98 (Table 4.3). Residual errors were found to exhibit normal homoscedastic behaviour.

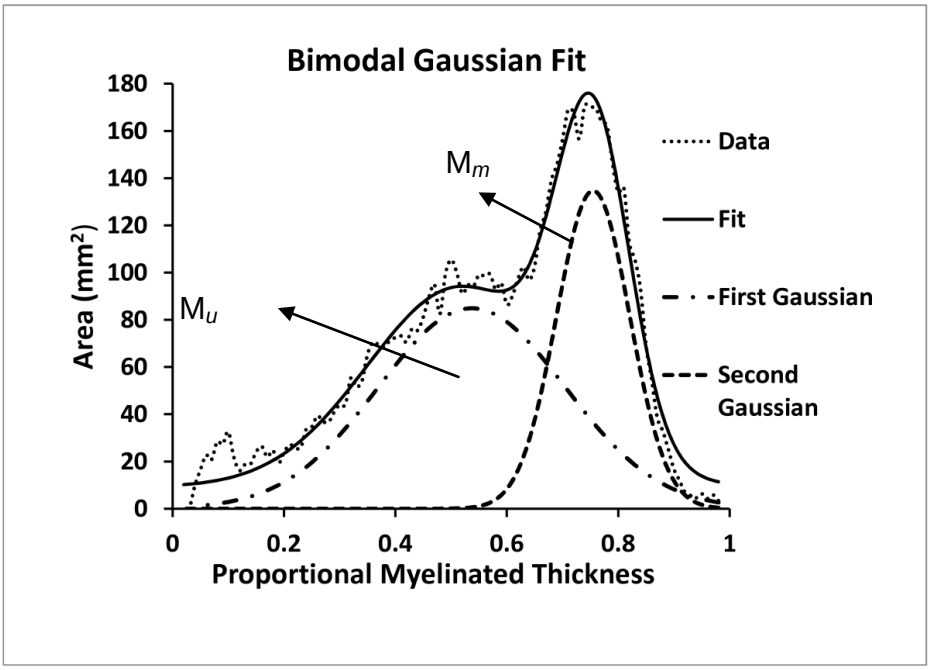

Figure 4.7: A representative graph of distribution of area with proportional myelinated thickness showing the actual data, the fitted function and the fitted function separated into two Gaussian curves. The first Gaussian represents the area M_u and the second Gaussian represents the heavily myelinated dorso-medial area M_m. The fit parameters (Equation 4.5) are the following: $\mu 1 = 0.52$, $\mu 2 = 0.75, \sigma 1 = 0.1, \sigma 2 = 0.07, C1 = 85, C2 = 135, C3 = 9$.

Thus, the distribution of area versus proportional myelinated thickness in the precentral motor cortex can be appropriately modelled as two Gaussian populations of proportional myelinated thickness. The first Gaussian with lower mean proportional thickness is representative of the relatively less myelinated region M_u, while the second Gaussian with higher mean proportional thickness is representative of the heavily myelinated dorso-medial core region M_m in the precentral motor cortex.

The proportional myelinated thickness data was projected on the pial surface in all sixteen hemispheres included in the study (Figure 4.7). The medial and dorsal part of each ROI had a distinctively high proportional myelinated thickness of 0.65 or more in all the subjects. The rest of the ROI has comparatively lower proportional myelinated thickness. This pattern suggests the precentral motor region indeed comprises two sub-regions (M_m and M_u) with distinguishable proportional myelinated thickness distributions.

	Amputees		**Controls**	
	Left	**Right**	**Left**	**Right**
1	0.90	0.87	0.98	0.96
2	0.97	0.93	0.96	0.98
3	0.98	0.97	0.98	0.97
4	0.96	0.98	0.96	0.98

Table 4.3: R-squared values for the bimodal fit, adjusted for degrees of freedom.

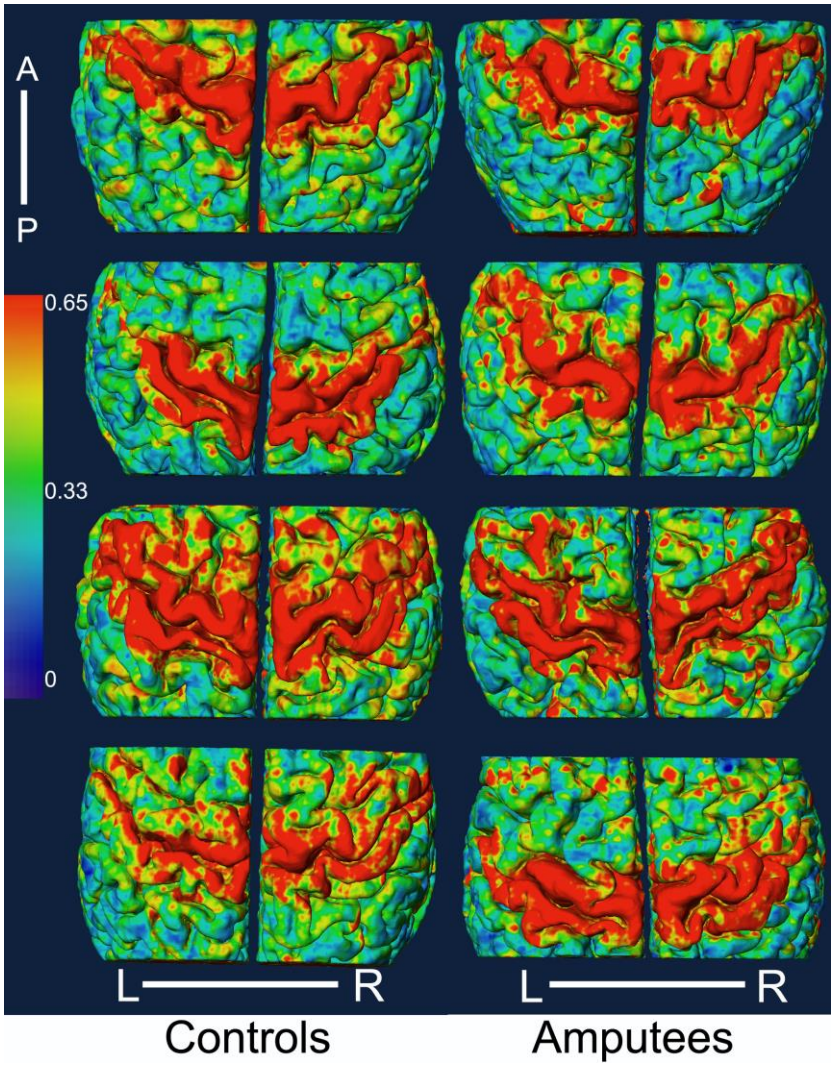

Figure 4.8: The proportional myelinated thickness data projected on the pial surface (dorsal view). The left column shows the controls while the right column shows the amputees. The subjects are represented in the same order in which they appear in Table 1. A = Anterior, P = Posterior, L = Left, R = Right.

4.2.2 Inter- and intra-group comparisons on the basis of proportional myelinated thickness

The mean proportional myelinated thickness in M_u and M_m is listed in Table 4.4 and shown in Figure 4.9 for all subjects. The difference of mean proportional myelinated thickness in the regions M_u and M_m in controls was found to be statistically significant ($p < 0.05$).

	Amputees				**Controls**			
	M_u (First Gaussian)		**M_m (Second Gaussian)**		**M_u (First Gaussian)**		**M_m (Second Gaussian)**	
	Left	**Right**	**Left**	**Right**	**Left**	**Right**	**Left**	**Right**
1	0.39	0.44	0.76	0.77	0.52	0.43	0.75	0.74
2	0.44	0.36	0.73	0.70	0.45	0.53	0.72	0.75
3	0.49	0.44	0.73	0.72	0.48	0.44	0.72	0.72
4	0.36	0.43	0.70	0.73	0.39	0.43	0.70	0.70
Mean ±SD	0.42 ±0.06	0.42 ±0.04	0.73 ±0.02	0.73 ±0.03	0.46 ±0.05	0.46 ±0.05	0.72 ±0.02	0.73 ±0.03

Table 4.4: The mean proportional myelinated thickness in the two sub-regions in the precentral motor cortex.

Mean proportional myelinated thickness in M_m in each hemisphere was compared between the two subject groups to see if amputation affected the proportional thickness of myelinated cortex. No statistically significant differences in the mean proportional myelinated thickness in M_m in the left ($p = 0.33$) as well as in the right ($p = 0.45$) hemisphere were noted when amputees were compared with controls.

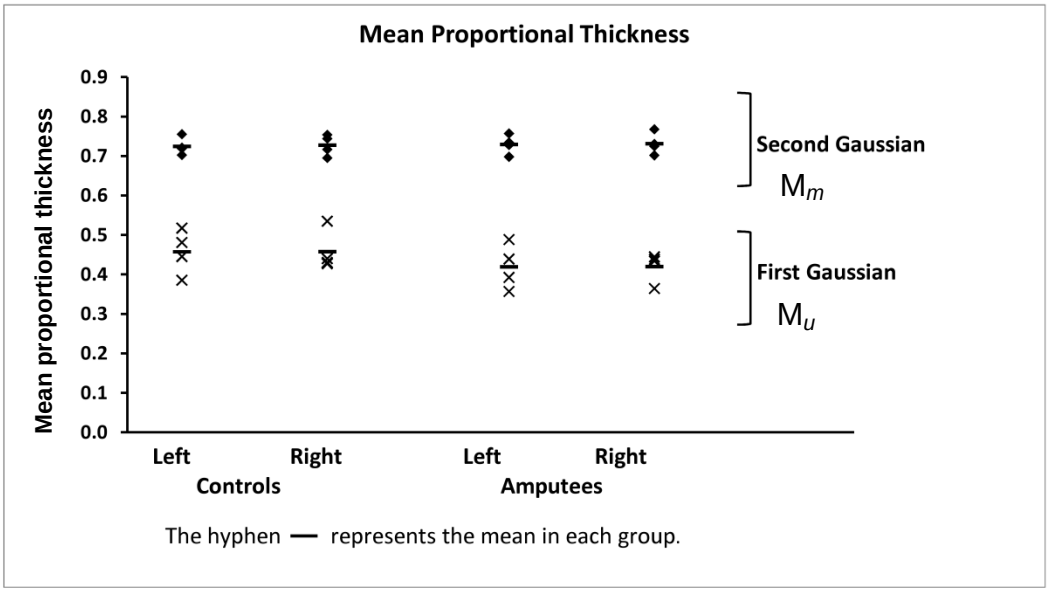

Figure 4.9: Mean proportional thickness in the two sub-regions M_m and M_u in the precentral motor cortex.

To assess for interhemispheric differences in the myelin pattern, the mean proportional myelinated thickness in M_m was compared between the left and right hemispheres in controls and no statistically significant difference was found ($p = 0.38$). The same comparison was performed in amputees and was also not statistically significant ($p = 0.5$).

4.2.3 The area measurements

The results of M_m area measurements are shown in Table 4.5 and Figure 4.10 and Figure 4.11. A larger variation in the area of M_m in controls in comparison with that in amputees was observed. The area of M_m in the left hemisphere of the controls ranged from 14.4 cm^2 to 61.7 cm^2 (a 4.3-fold variation). In the right hemisphere, it ranged from 25.8 cm^2 to 59.7 cm^2 showing a 2.3-fold variation. The total M_m area on both sides of the brain in the controls

varied from 41.7 cm^2 to 121.4 cm^2, thus having a 2.9-fold variation. The area of M_m in the left hemisphere of the amputees ranged from 27.2 cm^2 to 39.9 cm^2 (a 1.5-fold variation). In the right hemisphere, it ranged from 18.9 cm^2 to 32.5 cm^2 showing a 1.7-fold variation only. The total M_m area on both sides of the brain in the amputees varied from 48.3 cm^2 to 70.3 cm^2, thus having a 1.5-fold variation (Figures 4.10 and 4.11). To investigate the effect of amputation on the total area of M_m, the means of total M_m area in both groups were compared. The mean of total M_m area of 69.0 cm^2 in controls was not statistically different than the mean of total M_m area of 59.4 cm^2 in the amputees (p = 0.31).

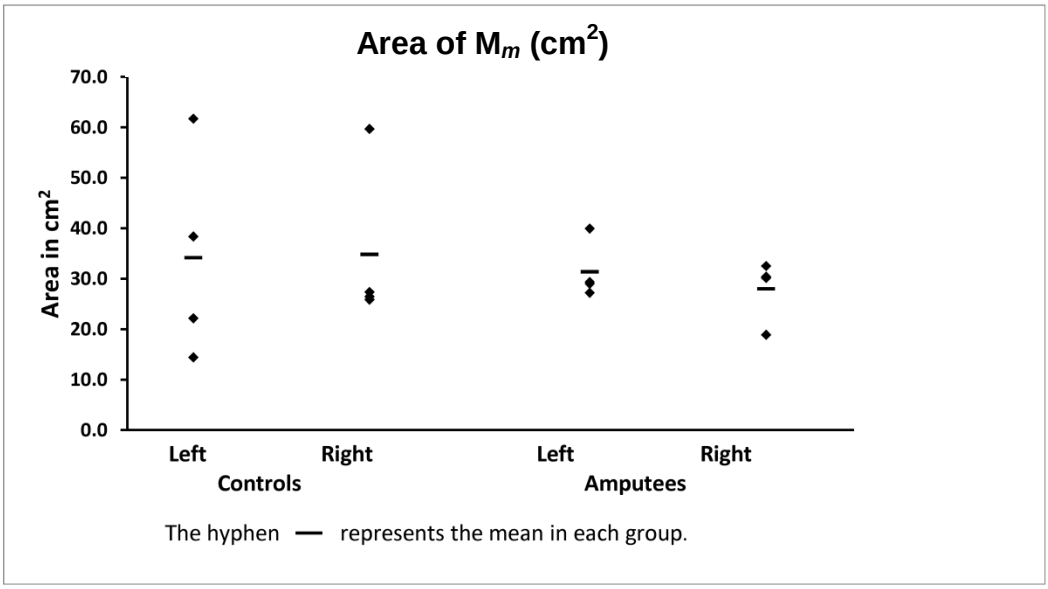

Figure 4.10: Hemispheric area of M_m for all subjects.

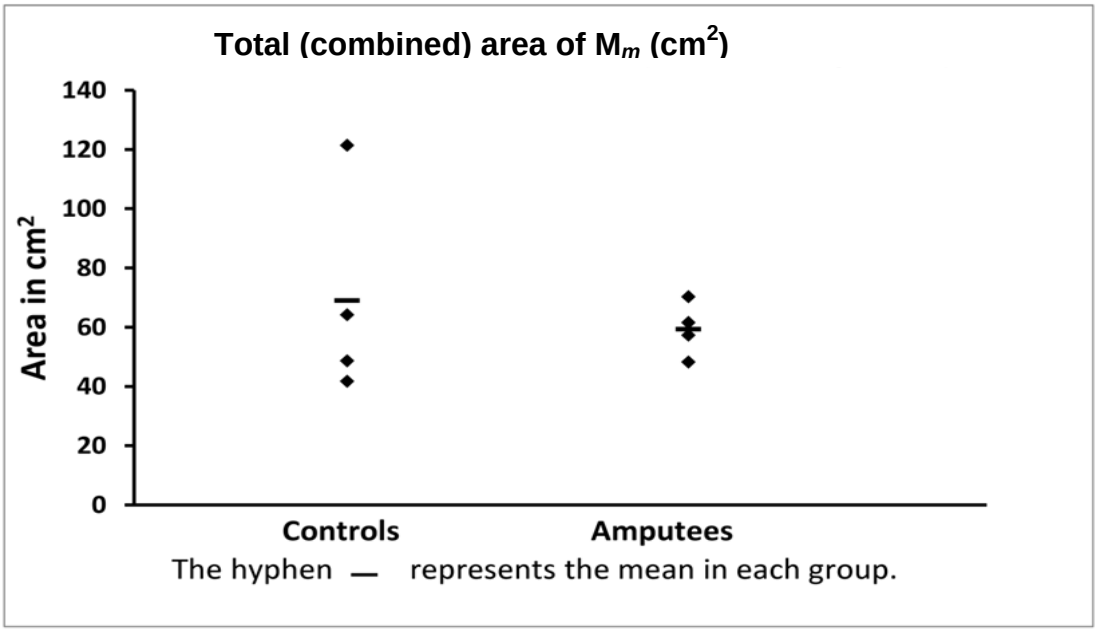

Figure 4.11: Total area of M_m (both hemispheres).

Area of M_m (cm^2)						
	Controls			Amputees		
	Left	Right	Both	Left	Right	Both
1	38.3	25.8	64.2	29.4	**18.9**	48.3
2	22.2	26.4	48.6	**29.0**	32.5	61.5
3	61.7	59.7	121.4	27.2	**30.1**	57.4
4	14.4	27.3	41.7	**39.9**	30.4	70.3
Mean	34.2	34.8	69.0	31.4	28.0	59.4

Table 4.5: M_m area measurements in both groups. The bold numbers indicate the hemisphere representing the lost limb in the amputees.

The interhemispheric differences in the area of M_m in both groups were assessed to see if morphology of this area is affected by differential use or disuse of a lower limb. Controls showed a 30 % mean interhemispheric difference in the M_m area compared to a corresponding difference of 23 % in amputees. Also, a

larger range of 3-60% in the hemispherical area differences was found in controls compared to a corresponding range of 10-40% in amputees. Furthermore, in two amputees, there was greater M_m area on the side contralateral to amputation (the affected hemisphere- indicated by bold numbers in Table 4.5) compared to the other side while for the other two amputees, the reverse was true.

4.3 Discussions and Conclusion

The result that a bimodal Gaussian function can be used to model the distribution of area with proportional myelinated thickness in the precentral motor cortex suggests the existence of two sub-regions in the precentral motor cortex: a dorso-medial region with comparatively higher proportional myelinated thickness (M_m) and an outer belt with lower values of proportional myelinated thickness (M_u). We were specifically interested in comparing features of M_m between controls and amputees because this region contains the primary motor cortex, which we hypothesized could be affected by lower limb amputation.

Two morphological quantities of M_m in the precentral motor cortex, the proportional myelinated thickness and area, were measured in four lower limb amputees and four controls. Although the number of subjects in each group was low, the pattern of variation in proportional myelinated thickness in the precentral motor cortex was found to be reproducible. In all 16 hemispheres studied, the well-myelinated motor region M_m was clearly distinguishable from the rest of the precentral cortex.

The results of proportional myelinated thickness measurements in the well-myelinated dorso-medial sub-region M_m in the precentral motor cortex indicate no statistically significant difference between the amputees and controls. Furthermore, these morphological measurements were not statistically different between the two hemispheres in the amputees. These findings suggest that the loss of lower limb function in amputees does not alter the proportional myelinated thickness in the precentral motor cortex.

The results of M_m area measurements indicate no statistically significant difference between lower limb amputees and controls. Thus, the data suggests that the total area of the well myelinated, core region in the precentral gyrus is preserved in lower limb amputation. However, a 2.9 fold variation in the total M_m area was seen in the controls. Given this high variation, amputation would need to cause a large change in the surface area of M_m for one to detect it, and one would need to look at a much larger group of subjects. Furthermore, the result that the amputees showed lesser interhemispheric difference in the size of the well myelinated area M_m must also be taken in the light of high variation in surface area for M_m in both the controls and amputees. As such, these findings only indicate that there are no grossly observable changes in the surface area of M_m following amputation.

The absence of any statistically observable difference in morphology of M_m as a result of amputation suggests that the myelination pattern in the precentral motor cortex is not disrupted as a consequence of amputation. All amputees had

a long standing loss of limb which occurred at an early age of 10 years or younger when the brain was still developing (Raznahan *et al.*, 2011). It is therefore very likely that any structural changes that could happen as a result of amputation would have completed their course by the time the amputees were imaged. The only motor pathway that is affected by amputation is the cortico-spinal pathway descending from the dorso-medial region of the precentral cortex and the upper motor neurons contributing to this tract are the giant Betz cells in layer V of the cortex. These pyramidal cells are known to contribute to the intracortical myelin by means of their axons and axons collaterals (Braitenberg, 1974). Furthermore, it is known that Betz cells in the leg area are the largest in size and have the thickest myelinated axons (Bishop and Smith, 1964; Lassek, 1940). The Betz cells therefore contribute significantly to the myelination in the primary motor cortex and an intact myelination pattern suggests that these Betz cells contributing to the movement of muscles in the previously intact limb do not degenerate when their prescribed output pathway is disrupted.

The ongoing viability of these upper motor neurons after amputation can be explained in more than one way. There could be new connections at the cortical level, at the level of spinal cord or at the level of peripheral nerves (Kaas and Qi, 2004). These upper motor neurons could make new connections at the cortical level and synapse with a different pool of lower motor neurons innervating the stump or other muscle groups. Or these upper motor neurons could still synapse with the same pool of lower motor neurons that was previously

innervating the intact limb but now those lower motor neurons have grown new connections at the spinal cord level or at the peripheral nerve level and are therefore innervating the stump or other muscle groups. In either case however, the viability of these upper motor neurons, as suggested by the intact myelination pattern, indicates that they control the movement of a new group of muscles after amputation. A purely morphological study like this one cannot differentiate between these scenarios. No human anatomical study investigating these scenarios is reported in the literature as yet. There is, however, one non-human primate study that reported a change in the internal anatomical organization of contralateral M1 in the amputated animals, as seen by labelling the synaptic connections (Wu and Kaas, 1999). Non-human primate studies also indicate that movements in other limbs are evoked by intracortical microstimulation throughout the presumed deprived forelimb region of the contralateral M1 (Kaas and Qi, 2004). Thus, these studies indicate that a rewiring of the contralateral motor cortex happens as a result of limb loss.

The potential re-wiring of the still viable upper motor neurons is also suggested by functional studies. On a functional level, degeneration of these upper motor neurons would mean absence of motor-task related activation in the deprived cortex and also, failure to excite any muscles (in the stump or elsewhere) by stimulating the deprived cortex. Available data from functional plasticity studies suggest that upper motor neurons stay functionally intact even after deprivation. A recent study in lower limb amputees observed an expansion

of activation maps of the stump in M1 of the deafferented hemisphere, spreading laterally to neighboring regions that represent the trunk and upper limbs (Simoes *et al.*, 2012). Another study in upper limb amputees, however, found M1 to be intact with no expansion or lateral shift of the stump muscle representation in M1 (Gagne *et al.*, 2011). Furthermore, an upper limb plasticity study reported sensation of movement in the phantom limb when trans-cranial magnetic stimulation was applied to the deprived motor cortex (Mercier *et al.*, 2006).

This is the first *in vivo* morphological study of the precentral motor cortex in amputees. Morphological studies investigating the deprived cortex in other primary functional regions have contradictory results. A human study that investigated the effect of congenital, as well as late onset, blindness on the visual areas reported a small but statistically significant decrease in the total area associated with primary and secondary visual cortices but the measurement was based on macro-anatomical landmarks rather than on the micro-structure (Park *et al.*, 2009). However, an intact pattern of intracortical myelin is reported by another human study where investigators could detect the stripe of Gennari, a myeloarchitectural hallmark of the primary visual cortex, in congenitally blind people (Trampel *et al.*, 2011). A very recent human study reported an increase in intracortical myelin in the deprived visual cortex in early or congenitally blind (Voss *et al.*, 2014). Thus, because of insufficient and contradicting data on features of intracortical myelin in the deprived sensory and motor cortex and

methodological differences between studies, the results of this study cannot be compared with previously published data.

In summary, it is observed that the two morphological features of the myeloarchitecture, the proportional myelinated thickness and the surface area of M_m, in the precentral motor region are not significantly altered as a result of long-standing lower limb amputation. We conclude that morphological measurements in the well myelinated cortical areas based on the proportional myelinated thickness can be used in future plasticity studies.

5 Conclusions and future directions

5.1 Conclusions

The research in this thesis presents a novel *in vivo* morphological study of the motor cortex in the precentral gyrus in humans based on anatomical MRI of intracortical myelin.

The first goal of the research presented in this thesis was to optimize MRI protocols to achieve enhanced intracortical contrast required to delineate the well-myelinated cortex from the adjacent cortex. A 3D, T_1-weighted MPRAGE sequence was optimized to achieve enhanced intracortical contrast at 0.7 mm isotropic resolution in an imaging time of 15 min. T_1 values in typical or unmyelinated cortical gray matter (GM), well myelinated cortical gray matter (GMm) and white matter were measured as 1280 ± 20, 1110 ± 40 and 740 ± 30 ms (mean ± SD of the sample, n=5), respectively. A contrast optimization was then performed based on the smaller T_1 difference of 170 ms between GMm and GM compared to the larger T_1 difference of 540 ms between WM and GM. By simulating the intracortical contrast using analytical signal equations, it was concluded that increasing the time delay between the end of the inner phase encoding block and the next inversion pulse results in the largest increase in intracortical contrast for a specific imaging time. Furthermore, it was found that dividing the T_1-weighted MPRAGE images with pre-dominantly proton density-weighted images significantly reduces the B_1 inhomogeneities.

The second goal of the research presented in this thesis was to develop image processing protocols to visualize the variation in myelin content across the motor cortex in the precentral motor cortex and delineate its well-myelinated dorso-medial part. The myeloarchitectonic feature that was selected for delineation of the well-myelinated cortex is the proportional myelinated thickness which is defined as the thickness of the myelinated tissue in the cortex relative to cortical thickness. To measure the thickness of myelinated tissue in the cortex, the masked brain (consisting of the cortex, underlying WM and some CSF) was segmented into GM, GMm, WM and cerebrospinal fluid (CSF). The distance between the outer boundary of GMm and WM was determined as the thickness of GMm, and the distance between the outer boundary of GM and WM was determined as the cortical thickness. The proportional myelinated thickness was calculated as the ratio of thickness of GMm and cortical thickness. When the proportional myelinated thickness data was projected on the pial surface, the dorso-medial sub-region of the precentral motor cortex, with relatively higher proportional myelinated thickness, was clearly distinguishable. Thus, it was concluded that proportional myelinated thickness can be used as a metric to distinguish between the well-myelinated cortex with relatively higher mean proportional myelinated thickness and the adjacent regions with relatively lower mean proportional myelinated thickness. Furthermore, the proportional myelinated thickness is a morphological metric and hence it does not depend on

the sequence parameters and the scanner. Thus it can be used for reproducible cortical mapping.

The third goal of the research presented in this thesis was to apply the imaging and image processing techniques to perform a morphological study of the primary motor region in four lower limb amputees and four matched controls. The proportional myelinated thickness was measured in the ROI consisting of the precentral motor cortex, and was used to distinguish between the well-myelinated dorso-medial sub-region M_m of the precentral motor cortex which consists of the primary motor cortex (BA 4) and the premotor cortex (BA 6), and the rest of the ROI which is relatively unmyelinated. Using the proportional myelinated thickness as a metric, the area of the well-myelinated dorso-medial sub-region M_m was also measured. No statistically significant differences ($p < 0.05$) between the amputees and the controls were found based on the mean proportional myelinated thickness and the area of the well-myelinated dorso-medial motor region in the precentral motor cortex. Thus, it was concluded that the myelin pattern is not grossly altered as a result of long withstanding loss of a lower limb.

5.2 Future directions

The techniques developed in this thesis present a novel way to study cortical mapping *in vivo*, using the thickness of the myelinated tissue in the cortex relative to the total cortical thickness as measured with T_1-weighted MRI. In principle, any other suitable contrast mechanism affected by the presence of myelin, such as T_2 (Laule *et al.*, 2007) or T_2^* (Cohen-Adad *et al.*, 2012) can be

utilized by optimizing the appropriate sequence for enhanced intracortical contrast. Future studies can compare the efficacy of various contrast mechanism for measuring the proportional myelinated thickness. Also, the possibility of using 3D T_1 mapping instead of T_1-weighted imaging can also be explored.

A shortcoming of the present image processing protocols is significant manual work, resulting in long processing times. Involvement of manual work may also reduce the reproducibility of the results by introducing a personal bias. One future goal therefore would be to fully automate the image processing pipeline. One manual step that results in an extensive increase in the processing time is the refining of the brain mask by removing the dura mater and subcortical GM structures. At present, some software packages, FreeSurfer for example, are capable of performing these steps as automated tasks but they are limited to 1 mm isotropic resolution data only. Therefore, better automated techniques are needed that can perform these tasks with least manual input on sub-mm resolution data as well. An example of the manual input in the processing protocols which can affect the reproducibility of the results is the selection of 0.1 fuzzy membership level for defining the outer boundary of WM. The need to adjust the WM boundary to account for the partial voluming of GMm into WM can be minimized by using the segmentation algorithms that can better estimate the partial voluming. Another example of manual input in image processing is the cropping of the region of interest (ROI) in the precentral gyrus. One way to avoid this would be to acquire whole brain images in each subject, register the whole

brain images to standard templates, such as the Talairach atlas (Talairach and Tournoux, 1988), and then perform cropping on the registered images. While it would result in lesser manual intervention, there is some danger that differences between individual brains might be lost due to inter-individual registration.

A major shortcoming of the morphological study of plasticity of the motor cortex was the very small group size. However, similar pattern of variation in intracortical myelin in all the subjects, controls and amputees, indicates that the technique is robust. Also, another shortcoming of the plasticity study was the unavailability of the total hemispherical area. In the absence of total hemispherical area data, it cannot be ascertained if the variation in the cortical field sizes across individuals represents variation in the individual field sizes or if it is related to the variation in the overall size of brain and hence total hemispherical surface area. Future studies therefore should also measure the total hemispherical area.

In the future, the technique can be extended to two types of studies of the motor cortex. It can be applied to determine the morphology of the primary motor cortex in larger groups of age- and sex-matched healthy subjects. Thus, it can be helpful in determining the variability in the motor field sizes across different populations and answering a fundamental neuroscience question of how big the motor field sizes are. The second motor cortex future application of the technique could be to use it to study cortical plasticity under various training scenarios -- for example subjects who play a sport versus non-players or musicians versus

controls. Such an investigation can help in determining if the underlying anatomical organization of the presumably normal cortex changes as a result of experience. Overall, both of these future applications can help in determining if the size of the motor cortex is an indicator of its health.

The technique can also be extended to other well-myelinated cortical areas with relatively higher proportional myelinated thickness. These include the primary somatosensory cortex, the primary auditory cortex and the visual cortex (Brodmann, 1909). Studies investigating the morphology and plasticity of these sensory regions in the healthy population can be designed. Thus, the technique can be useful for surveying cortical field sizes in the normal, healthy population. Knowing the variability of the cortical field sizes in the healthy population can be beneficial for further morphological studies in the following way. A very wide range of normal field sizes, if found, would render the morphological studies in the presumably abnormal cortex as inconclusive. A rather narrow range of normal cortical field sizes, if found, would help in determining if cortical morphology is affected by disease.

An important application of this technique could be in rehabilitation planning for example in people who have lost motor control due to stroke. The rehabilitation efforts are designed on the premise that gross changes in the function have not affected the cortical health. However, if the cortical health is compromised due to gross changes in the function or due to the stroke, the rehabilitation efforts would need to address that too. The technique can be used

to assess the morphology of the affected cortex and rehabilitation efforts can be designed accordingly to improve the outcome.

5.3 Overall conclusions

The overall conclusions of the research presented in this thesis can be summarized as below.

- Specific optimization of the anatomical MRI protocols can result in improvement in the visualization of the intracortical myelin for delineation of the well-myelinated regions. This can be of great advantage for cortical mapping studies.
- Proportional myelinated thickness, defined as the ratio of the thickness of the myelinated tissue in the cortex to the cortical thickness, is a reproducible metric for delineation of the well-myelinated cortex.
- The myelin pattern in the dorso-medial part of the precentral motor cortex in lower limb amputees is not grossly affected when compared with healthy controls, on the basis of the mean proportional myelinated thickness and the area of this region.

REFERENCES

Arnold JB, Liow JS, Schaper KA, Stern JJ, Sled JG, Shattuck DW, Worth AJ, Cohen MS, Leahy RM, Mazziotta JC,Rottenberg DA (2001) Qualitative and quantitative evaluation of six algorithms for correcting intensity nonuniformity effects. Neuroimage 13:931-943.

Augustinack JC, van der Kouwe AJ, Blackwell ML, Salat DH, Wiggins CJ, Frosch MP, Wiggins GC, Potthast A, Wald LL,Fischl BR (2005) Detection of entorhinal layer II using 7Tesla [corrected] magnetic resonance imaging. Ann Neurol 57:489-494.

Baillarger J (1840) Mem Acad Med Paris

Barbier EL, Marrett S, Danek A, Vortmeyer A, van Gelderen P, Duyn J, Bandettini P, Grafman J,Koretsky AP (2002) Imaging cortical anatomy by high-resolution MR at 3.0T: detection of the stripe of Gennari in visual area 17. Magn Reson Med 48:735-738.

Belaroussi B, Milles J, Carme S, Zhu YM,Benoit-Cattin H (2006) Intensity non-uniformity correction in MRI: existing methods and their validation. Med Image Anal 10:234-246.

Bernstein M, King K, Xiaohong J, (2004) Handbook of MRI Pulse Sequences. USA: Elsevier.

Bezdek J (1984) FCM: The fuzzy *c*-means clustering algorithm. Computers & Geosciences 10:191-203.

Bishop GH,Smith JM (1964) The sizes of nerve fibers supplying cerebral cortex. Experimental Neurology 9:483-501.

Bock NA, Kocharyan A, Liu JV,Silva AC (2009) Visualizing the entire cortical myelination pattern in marmosets with magnetic resonance imaging. J Neurosci Methods 185:15-22.

Bock NA, Hashim E, Janik R, Konyer NB, Weiss M, Stanisz GJ, Turner R,Geyer S (2013) Optimizing T-1-weighted imaging of cortical myelin content at 3.0 T. Neuroimage 65:1-12.

Braak H, (1980) Architectonics of the human telencephalic cortex. Berlin: Springer.

Braitenberg V (1962) A note on myeloarchitectonics. Journal of Comparative Neurology 118:141-156.

Braitenberg V (1974) Thoughts on the cerebral cortex. J Theor Biol 46:421-447.

Braitenberg V (1974) Thoughts on the cerebral cortex. J Theor Biol 46:421-447.

Bridge H, Clare S, Jenkinson M, Jezzard P, Parker AJ,Matthews PM (2005) Independent anatomical and functional measures of the V1/V2 boundary in human visual cortex. J Vis 5:93-102.

Brodmann K (1909) Vergleichende Lokalisationslehre der Großhirnrinde.Leipzig: Barth.

Clare S,Bridge H (2005) Methodological issues relating to in vivo cortical myelography using MRI. Hum Brain Mapp 26:240-250.

Clare S,Jezzard P (2001) Rapid T-1 mapping using multislice echo planar imaging. Magnetic Resonance in Medicine 45:630-634.

Clark VP, Courchesne E,Grafe M (1992) In vivo myeloarchitectonic analysis of human striate and extrastriate cortex using magnetic resonance imaging. Cereb Cortex 2:417-424.

Cohen-Adad J, Polimeni JR, Helmer KG, Benner T, McNab JA, Wald LL, Rosen BR,Mainero C (2012) T-2* mapping and B-o orientation-dependence at 7 T reveal cyto- and myeloarchitecture organization of the human cortex. Neuroimage 60:1006-1014.

Cook LL, Foster PJ, Mitchell JR,Karlik SJ (2004) In vivo 4.0-T magnetic resonance investigation of spinal cord inflammation, demyelination, and axonal damage in chronic-progressive experimental allergic encephalomyelitis. J Magn Reson Imaging 20:563-571.

Crawley AP,Henkelman RM (1988) A comparison of one-shot and recovery methods in T1 imaging. Magn Reson Med 7:23-34.

Dahnke R, Yotter RA,Gaser C (2013) Cortical thickness and central surface estimation. Neuroimage 65:336-348.

Dale AM, Fischl B,Sereno MI (1999) Cortical surface-based analysis. I. Segmentation and surface reconstruction. Neuroimage 9:179-194.

Deichmann R, Good CD, Josephs O, Ashburner J,Turner R (2000) Optimization of 3-D MP-RAGE sequences for structural brain imaging. Neuroimage 12:112-127.

Deichmann R,Haase A (1992) Quantification of T1 Values by Snapshot-Flash Nmr Imaging. Journal of Magnetic Resonance 96:608-612.

Dick F, Tierney AT, Lutti A, Josephs O, Sereno MI,Weiskopf N (2012) In vivo functional and myeloarchitectonic mapping of human primary auditory areas. J Neurosci 32:16095-16105.

Draganski B, Moser T, Lummel N, Ganssbauer S, Bogdahn U, Haas F,May A (2006) Decrease of thalamic gray matter following limb amputation. Neuroimage 31:951-957.

Dunn J (1973) A Fuzzy Relative of the ISODATA Process and Its Use in Detecting Compact Well-Separated Clusters. Journal of Cybernetics 3:32-57.

Eickhoff S, Walters NB, Schleicher A, Kril J, Egan GF, Zilles K, Watson JD,Amunts K (2005) High-resolution MRI reflects myeloarchitecture and cytoarchitecture of human cerebral cortex. Hum Brain Mapp 24:206-215.

Elliot SG (1907) A new topographical survey of the human cerebral cortex, being an account of the distribution of the anatomically distinct cortical areas and their relationship to the cerebral sulci. J Anat 41:237–254:

Fahim C, Yoon U, Das S, Lyttelton O, Chen J, Arnaoutelis R, Rouleau G, Sandor P, Frey K, Brandner C,Evans AC (2010) Somatosensory-motor bodily representation cortical thinning in Tourette: effects of tic severity, age and gender. Cortex 46:750-760.

Fischl B, Salat DH, Busa E, Albert M, Dieterich M, Haselgrove C, van der Kouwe A, Killiany R, Kennedy D, Klaveness S, Montillo A, Makris N, Rosen B,Dale AM (2002) Whole brain segmentation: automated labeling of neuroanatomical structures in the human brain. Neuron 33:341-355.

Gagne M, Hetu S, Reilly KT,Mercier C (2011) The Map is Not the Territory: Motor System Reorganization in Upper Limb Amputees. Hum Brain Mapp 32:509-519.

Gelman N, Ewing JR, Gorell JM, Spickler EM,Solomon EG (2001) Interregional variation of longitudinal relaxation rates in human brain at 3.0 T: relation to estimated iron and water contents. Magn Reson Med 45:71-79.

Geyer S, Ledberg A, Schleicher A, Kinomura S, Schormann T, Burgel U, Klingberg T, Larsson J, Zilles K,Roland PE (1996) Two different areas within the primary motor cortex of man. Nature 382:805-807.

Geyer S, Matelli M, Luppino G,Zilles K (2000) Functional neuroanatomy of the primate isocortical motor system. Anat Embryol (Berl) 202:443-474.

Geyer S, Weiss M, Reimann K, Lohmann G,Turner R (2011) Microstructural Parcellation of the Human Cerebral Cortex - From Brodmann's Post-Mortem Map to in vivo Mapping with High-Field Magnetic Resonance Imaging. Front Hum Neurosci 5:19.

Glasser MF,Van Essen DC (2011) Mapping human cortical areas in vivo based on myelin content as revealed by T1- and T2-weighted MRI. J Neurosci 31:11597-11616.

Grydeland H, Walhovd KB, Tamnes CK, Westlye LT,Fjell AM (2013) Intracortical myelin links with performance variability across the human lifespan: results from T1- and T2-weighted MRI myelin mapping and diffusion tensor imaging. J Neurosci 33:18618-18630.

Gudbjartsson H,Patz S (1995) The Rician distribution of noisy MRI data. Magn Reson Med 34:910-914.

Haacke E, Brown R, Thompson M, Venkatesan R, (1999) Magnetic Resonance Imaging:Physical Principles and Sequence Design. USA: WILEY-LISS.

Han X, Xu C,Prince J (2003) A topology preserving level set method for geometric deformable models. IEEE Trans Pattern Anal Mach Intell 25:755-768.

Han X, Xu C, Tosun D, Prince J, (2001) Cortical surface reconstruction using a topology preserving geometric deformable model. (Staib L ed), pp 220.

Hazelwood C, Chang D, Nichols B,Woessner D (1974) Nuclear magnetic resonance transverse relaxation times of water protons in skeletal muscles. Biophys. J.

Henderson E, McKinnon G, Lee TY,Rutt BK (1999) A fast 3D look-locker method for volumetric T1 mapping. Magn Reson Imaging 17:1163-1171.

Henderson LA, Gustin SM, Macey PM, Wrigley PJ,Siddall PJ (2011) Functional reorganization of the brain in humans following spinal cord injury: evidence for underlying changes in cortical anatomy. J Neurosci 31:2630-2637.

Holsinger A,Riederer S (1990) The Importance of Phase-Encoding Order in Ultra-Short Tr Snapshot Mr Imaging. Magnetic Resonance in Medicine 16:481-488.

Hopf A (1954) Die Myeloarchitektonik des Isocortex temporalis beim Menschen. J Hirnforsch 1:208-279.

Hutton C, De Vita E, Ashburner J, Deichmann R,Turner R (2008) Voxel-based cortical thickness measurements in MRI. Neuroimage 40:1701-1710.

Jones SE, Buchbinder BR,Aharon I (2000) Three-dimensional mapping of cortical thickness using Laplace's equation. Hum Brain Mapp 11:12-32.

Kaas JH,Qi HX (2004) The reorganization of the motor system in primates after the loss of a limb. Restor Neurol Neurosci 22:145-152.

Kim EY, Kim DH, Chang JH, Yoo E, Lee JW,Park HJ (2009) Triple-layer appearance of Brodmann area 4 at thin-section double inversion-recovery MR imaging. Radiology 250:515-522.

la Fougere C, Grant S, Kostikov A, Schirrmacher R, Gravel P, Schipper HM, Reader A, Evans A,Thiel A (2011) Where in-vivo imaging meets cytoarchitectonics: the relationship between cortical thickness and neuronal density measured with high-resolution [18F]flumazenil-PET. Neuroimage 56:951-960.

Langer N, Hanggi J, Muller NA, Simmen HP,Jancke L (2012) Effects of limb immobilization on brain plasticity. Neurology 78:182-188.

Lassek A (1940) A numerical investigation of the Betz cells of the motor area. Archives of Neurology and Psychiatry 718.

Laule C, Vavasour IM, Kolind SH, Li DK, Traboulsee TL, Moore GR,MacKay AL (2007) Magnetic resonance imaging of myelin. Neurotherapeutics 4:460-484.

Lewis B,Henry C (1877) The cortical lamination of the motor area of the brain.

Li G, Nie J, Wu G, Wang Y, Shen D,Alzheimer's Disease Neuroimaging Initiative (2012) Consistent reconstruction of cortical surfaces from longitudinal brain MR images. Neuroimage 59:3805-3820.

Lin C, Bernstein M, Huston J,Fain S, (2001) Measurements of T1 Relaxation times at 3.0T: Implications for clinical MRA. . ISMRM p-1391.

Liu T, Nie J, Tarokh A, Guo L,Wong ST (2008) Reconstruction of central cortical surface from brain MRI images: method and application. Neuroimage 40:991-1002.

Look D,Locker D (1970) Time Saving in Measurement of NMR and EPR Relaxation Times. Rev Sci Instrum 41:250.

Lorensen W,Cline H (1987) Marching Cubes: A high resolution 3D surface construction algorithm. Computer Graphics 21:163-169.

Lotze M, Flor H, Grodd W, Larbig W,Birbaumer N (2001) Phantom movements and pain. An fMRI study in upper limb amputees. Brain 124:2268-2277.

Lu H, Nagae-Poetscher LM, Golay X, Lin D, Pomper M,van Zijl PC (2005) Routine clinical brain MRI sequences for use at 3.0 Tesla. J Magn Reson Imaging 22:13-22.

Lucas BC, Bogovic JA, Carass A, Bazin PL, Prince JL, Pham DL,Landman BA (2010) The Java Image Science Toolkit (JIST) for rapid prototyping and publishing of neuroimaging software. Neuroinformatics 8:5-17.

Lusebrink F, Wollrab A,Speck O (2013) Cortical thickness determination of the human brain using high resolution 3T and 7T MRI data. Neuroimage 70:122-131.

MacDonald D, Kabani N, Avis D,Evans AC (2000) Automated 3-D extraction of inner and outer surfaces of cerebral cortex from MRI. Neuroimage 12:340-356.

Marques JP, Kober T, Krueger G, van der Zwaag W, Van de Moortele PF,Gruetter R (2010) MP2RAGE, a self bias-field corrected sequence for improved segmentation and T1-mapping at high field. Neuroimage 49:1271-1281.

Matthews PM, Clare S,Adcock J (1999) Functional magnetic resonance imaging: clinical applications and potential. J Inherit Metab Dis 22:337-352.

Mercier C, Reilly KT, Vargas CD, Aballea A,Sirigu A (2006) Mapping phantom movement representations in the motor cortex of amputees. Brain 129:2202-2210.

Niedermeyer E, Lopes da Silva F, (2005) Electroencephalography: Basic Principles, Clinical Applications, and Related Fields. Philadelphia, USA: Lippincott Williams & Wilkins.

Nieuwenhuys R (2013) The myeloarchitectonic studies on the human cerebral cortex of the Vogt-Vogt school, and their significance for the interpretation of functional neuroimaging data. Brain Struct Funct 218:303-352.

Nieuwenhuys R, Voogd J, van Huijzen C, (2008) The Human Central Nervous System. Germany: Springer.

Nishimura D, (1996) Principles of Magnetic Resonance Imaging.

Osechinskiy S,Kruggel F (2012) Cortical Surface Reconstruction from High-Resolution MR Brain Images. Int J Biomed Imaging 2012:870196.

Osher S, Paragios N, (2003) Geometric level set methods in imaging, vision and graphics. New York: Springer-Verlag.

Park HJ, Lee JD, Kim EY, Park B, Oh MK, Lee S,Kim JJ (2009) Morphological alterations in the congenital blind based on the analysis of cortical thickness and surface area. Neuroimage 47:98-106.

Penfield W, Rasmussen T, (1950) The cerebral cortex of man: a clinical study of localization of function. New York: Macmillan.

Pham DL,Prince JL (1999) Adaptive fuzzy segmentation of magnetic resonance images. IEEE Trans Med Imaging 18:737-752.

Pham DL, Xu C,Prince JL (2000) Current methods in medical image segmentation. Annu Rev Biomed Eng 2:315-337.

Preissl H, (2005) Magnetoencephalography. USA: Elsevier Academic Press.

Preissler S, Feiler J, Dietrich C, Hofmann GO, Miltner WH,Weiss T (2013) Gray matter changes following limb amputation with high and low intensities of phantom limb pain. Cereb Cortex 23:1038-1048.

Qi HX, Jain N, Collins CE, Lyon DC,Kaas JH (2010) Functional organization of motor cortex of adult macaque monkeys is altered by sensory loss in infancy. Proc Natl Acad Sci U S A 107:3192-3197.

Querbes O, Aubry F, Pariente J, Lotterie JA, Demonet JF, Duret V, Puel M, Berry I, Fort JC, Celsis P,Alzheimer's Disease Neuroimaging Initiative (2009) Early diagnosis of Alzheimer's disease using cortical thickness: impact of cognitive reserve. Brain 132:2036-2047.

Raznahan A, Shaw P, Lalonde F, Stockman M, Wallace GL, Greenstein D, Clasen L, Gogtay N,Giedd JN (2011) How does your cortex grow? J Neurosci 31:7174-7177.

Rockstroh B, Vanni S, Elbert T, Hari R, (2000) Extensive somatosensory stimulation alters somatosensory evoked fields. (Aine, CJ Okada, Y Stroink, G Swithenby, SJ Wood,CC ed), pp 851.

Roiha K, Kirveskari E, Kaste M, Mustanoja S, Makela JP, Salonen O, Tatlisumak T,Forss N (2011) Reorganization of the primary somatosensory cortex during stroke recovery. Clin Neurophysiol 122:339-345.

Rooney WD, Johnson G, Li X, Cohen ER, Kim SG, Ugurbil K,Springer CS,Jr (2007) Magnetic field and tissue dependencies of human brain longitudinal 1H2O relaxation in vivo. Magn Reson Med 57:308-318.

Rosas HD, Salat DH, Lee SY, Zaleta AK, Pappu V, Fischl B, Greve D, Hevelone N,Hersch SM (2008) Cerebral cortex and the clinical expression of Huntington's disease: complexity and heterogeneity. Brain 131:1057-1068.

Sailer M, Fischl B, Salat D, Tempelmann C, Schonfeld MA, Busa E, Bodammer N, Heinze HJ,Dale A (2003) Focal thinning of the cerebral cortex in multiple sclerosis. Brain 126:1734-1744.

Sanchez-Panchuelo RM, Francis ST, Schluppeck D,Bowtell RW (2012) Correspondence of human visual areas identified using functional and anatomical MRI in vivo at 7 T. J Magn Reson Imaging 35:287-299.

Sarty G, (2005) MRI Physics for Life Science Researchers.

Schmierer K, Wheeler-Kingshott CA, Boulby PA, Scaravilli F, Altmann DR, Barker GJ, Tofts PS,Miller DH (2007) Diffusion tensor imaging of post mortem multiple sclerosis brain. Neuroimage 35:467-477.

Sereno MI, Lutti A, Weiskopf N,Dick F (2013) Mapping the human cortical surface by combining quantitative T(1) with retinotopy. Cereb Cortex 23:2261-2268.

Sethian JA (1996) A fast marching level set method for monotonically advancing fronts. Proc Natl Acad Sci U S A 93:1591-1595.

Sigalovsky IS, Fischl B,Melcher JR (2006) Mapping an intrinsic MR property of gray matter in auditory cortex of living humans: a possible marker for primary cortex and hemispheric differences. Neuroimage 32:1524-1537.

Simoes EL, Bramati I, Rodrigues E, Franzoi A, Moll J, Lent R,Tovar-Moll F (2012) Functional expansion of sensorimotor representation and structural reorganization of callosal connections in lower limb amputees. J Neurosci 32:3211-3220.

Sled JG, Zijdenbos AP,Evans AC (1998) A nonparametric method for automatic correction of intensity nonuniformity in MRI data. IEEE Trans Med Imaging 17:87-97.

Talairach J, Tournoux P, (1988) Co-Planar Stereotaxic Atlas of the Human Brain. New York: Thieme Medical Publishers.

Tofts P, (2003) Quantitative MRI of the brain:Measuring changes caused by disease. England: John Wiley & Sons.

Tokunaga C, Arimura H, Yoshiura T, Ohara T, Yamashita Y, Kobayashi K, Magome T, Nakamura Y, Honda H, Hirata H, Ohki M,Toyofuku F (2013) Automated measurement of three-dimensional cerebral cortical thickness in Alzheimer's patients using localized gradient vector trajectory in fuzzy membership maps. J. Biomedical Science and Engineering 6:327-336.

Trampel R, Ott DV,Turner R (2011) Do the congenitally blind have a stria of Gennari? First intracortical insights in vivo. Cereb Cortex 21:2075-2081.

Van de Moortele PF, Auerbach EJ, Olman C, Yacoub E, Ugurbil K,Moeller S (2009) T1 weighted brain images at 7 Tesla unbiased for Proton Density, T2* contrast and RF coil receive B1 sensitivity with simultaneous vessel visualization. Neuroimage 46:432-446.

Vogt C, Vogt O, (1928) Die Grundlagen und die Teildisziplinen der mikroskopischen Anatomie des Zentralnervensystems. . In: Handbuch des mikroskopischen Anatomie des Menschen. pp 448-477. Berlin: Springer.

Vogt C,Vogt O (1909) Allgemeinere Ergebnisse unserer Hirnforschung. J Psychol Neurol 25:279-468.

Vogt O (1951) Die anatomische Vertiefung der menschlichen Hirnlokalisation. Klin Wochenschr 29:111-125.

Vogt C,Vogt O (1919) Allgemeinere Ergebnisse unserer Hirnforschung. J fu¨ r Psychologie und Neurologie 25:279–461:

von Economo K, Koskinas G, (1925) Die Cytoarchitektonik der Hirnrinde des erwachsenen Menschen. Wien: Springer.

Voss P, Pike BG,Zatorre RJ (2014) Evidence for both compensatory plastic and disuse atrophy-related neuroanatomical changes in the blind. Brain 137:1224-1240.

Waehnert MD, Dinse J, Weiss M, Streicher MN, Waehnert P, Geyer S, Turner R,Bazin PL (2013) Anatomically motivated modeling of cortical laminae. Neuroimage

Wansapura JP, Holland SK, Dunn RS,Ball WS,Jr (1999) NMR relaxation times in the human brain at 3.0 tesla. J Magn Reson Imaging 9:531-538.

Wright PJ, Mougin OE, Totman JJ, Peters AM, Brookes MJ, Coxon R, Morris PE, Clemence M, Francis ST, Bowtell RW,Gowland PA (2008) Water proton T1 measurements in brain tissue at 7, 3, and 1.5 T using IR-EPI, IR-TSE, and MPRAGE: results and optimization. MAGMA 21:121-130.

Wu CW,Kaas JH (1999) Reorganization in primary motor cortex of primates with long-standing therapeutic amputations. J Neurosci 19:7679-7697.

Xu C, Pham DL, Rettmann ME, Yu DN,Prince JL (1999) Reconstruction of the human cerebral cortex from magnetic resonance images. IEEE Trans Med Imaging 18:467-480.

Yoshiura T, Higano S, Rubio A, Shrier DA, Kwok WE, Iwanaga S,Numaguchi Y (2000) Heschl and superior temporal gyri: low signal intensity of the cortex on T2-weighted MR images of the normal brain. Radiology 214:217-221.

Zhao H (2005) A fast sweeping method for Eikonal equations. Mathematics of Computation 74:603-627.

Zhu DC,Penn RD (2005) Full-brain T1 mapping through inversion recovery fast spin echo imaging with time-efficient slice ordering. Magn Reson Med 54:725-731.

Zilles K, Amunts K, (2012) Architecture of the cerebral cortex. In: The human nervous system. Academic Press.

Zilles K, (2004) Architecture of the Human Cerebral Cortex. In: The Human Nervous System. Second edition (Paxinos G, Mai Jürgen K eds), pp 997-1055. Amsterdam: Elsevier Academic Press.

Appendix

Reprint permissions

1. Figure 1.1

SPRINGER LICENSE
TERMS AND CONDITIONS

Jul 02, 2014

This is a License Agreement between Eyesha Hashim ("You") and Springer ("Springer") provided by Copyright Clearance Center ("CCC"). The license consists of your order details, the terms and conditions provided by Springer, and the payment terms and conditions.

All payments must be made in full to CCC. For payment instructions, please see information listed at the bottom of this form.

License Number	3420820128389
License date	Jul 02, 2014
Licensed content publisher	Springer
Licensed content publication	Springer eBook
Licensed content title	Telencephalon: Neocortex
Licensed content author	None
Licensed content date	Jan 1, 2008
Type of Use	Thesis/Dissertation
Portion	Figures
Author of this Springer article	No
Order reference number	None
Original figure numbers	Figure 15.4
Title of your thesis / dissertation	A MORPHOLOGICAL STUDY OF THE PRIMARY MOTOR CORTEX USING MRI
Expected completion date	Aug 2014
Estimated size(pages)	200
Total	0.00 CAD

2. Figure 1.2 and Figure 4.2

SPRINGER LICENSE
TERMS AND CONDITIONS

Jul 02, 2014

This is a License Agreement between Eyesha Hashim ("You") and Springer ("Springer") provided by Copyright Clearance Center ("CCC"). The license consists of your order details, the terms and conditions provided by Springer, and the payment terms and conditions.

All payments must be made in full to CCC. For payment instructions, please see information listed at the bottom of this form.

License Number	3420820433152
License date	Jul 02, 2014
Licensed content publisher	Springer
Licensed content publication	Brain Structure and Function
Licensed content title	The myeloarchitectonic studies on the human cerebral cortex of the Vogt–Vogt school, and their significance for the interpretation of functional neuroimaging data
Licensed content author	Rudolf Nieuwenhuys
Licensed content date	Jan 1, 2012
Volume number	218
Issue number	2
Type of Use	Thesis/Dissertation
Portion	Figures
Author of this Springer article	No
Order reference number	None
Original figure numbers	Figure 1, 3, 7
Title of your thesis / dissertation	A MORPHOLOGICAL STUDY OF THE PRIMARY MOTOR CORTEX USING MRI
Expected completion date	Aug 2014
Estimated size(pages)	200
Total	0.00 USD

3. Figure 2.4

SPRINGER LICENSE
TERMS AND CONDITIONS

Jul 02, 2014

This is a License Agreement between Eyesha Hashim ("You") and Springer ("Springer") provided by Copyright Clearance Center ("CCC"). The license consists of your order details, the terms and conditions provided by Springer, and the payment terms and conditions.

All payments must be made in full to CCC. For payment instructions, please see information listed at the bottom of this form.

License Number	3420830025369
License date	Jul 02, 2014
Licensed content publisher	Springer
Licensed content publication	Springer eBook
Licensed content title	Motor Systems
Licensed content author	None
Licensed content date	Jan 1, 2008
Type of Use	Thesis/Dissertation
Portion	Figures
Author of this Springer article	No
Order reference number	None
Original figure numbers	figure 21.7
Title of your thesis / dissertation	A MORPHOLOGICAL STUDY OF THE PRIMARY MOTOR CORTEX USING MRI
Expected completion date	Aug 2014
Estimated size(pages)	200
Total	0,00 USD

4. Figure 4.1

SPRINGER LICENSE
TERMS AND CONDITIONS

Jul 02, 2014

This is a License Agreement between Eyesha Hashim ("You") and Springer ("Springer") provided by Copyright Clearance Center ("CCC"). The license consists of your order details, the terms and conditions provided by Springer, and the payment terms and conditions.

All payments must be made in full to CCC. For payment instructions, please see information listed at the bottom of this form.

License Number	3420821332920
License date	Jul 02, 2014
Licensed content publisher	Springer
Licensed content publication	Springer eBook
Licensed content title	Telencephalon: Neocortex
Licensed content author	None
Licensed content date	Jan 1, 2008
Type of Use	Thesis/Dissertation
Portion	Figures
Author of this Springer article	No
Order reference number	None
Original figure numbers	Figure 15.19
Title of your thesis / dissertation	A MORPHOLOGICAL STUDY OF THE PRIMARY MOTOR CORTEX USING MRI
Expected completion date	Aug 2014
Estimated size(pages)	200
Total	0.00 USD